KOBELCO TECHNOLOGY REVIEW

No. 34 Mar. 2016

Feature- Ⅰ: Infrastructure systems -In pursuit of safety and security-
Feature- Ⅱ: Electronic and Electric technologies (Advanced Materials and Apparatuses)

Contents

Feature- Ⅰ Infrastructure systems -In pursuit of safety and security-

Feature- Ⅱ Electronic and Electric technologies (Advanced Materials and Apparatuses)

Published by

Secretariat & Publicity Dept.
Kobe Steel, Ltd.

2-4, Wakinohama-Kaigandori 2-chome,
Chuo-ku, Kobe, HYOGO 651-8585,
JAPAN
http://www.kobelco.co.jp

Editorial Office: **Shinko Research Co., Ltd.**
5-5, Takatsukadai 1-chome,
Nishi-ku, Kobe, HYOGO 651-2271, JAPAN
Fax: +81-78-992-9790
E-mail: rd-office@kobelco.com

Advanced Techniques for Analyzing Corrosion Resistance of Steels for Infrastructure

Dr. Takenori NAKAYAMA*1

*1 Materials Research Laboratory, Technical Development Group

This paper reviews methods for quantitatively measuring the composition of steel rust by X-ray diffraction using internal standards. Also introduced is a method for evaluating the size of rust particles on the basis of molecular adsorption. Experiments with artificially synthesized rust described here suggest new approaches to improve the corrosion resistance of steels. The atmospheric corrosion phenomena of steels used for infrastructures have been analyzed using the ultra-bright synchrotron radiation generated by SPring-8 and the neutron beam generated by a compact neutron source by RIKEN.

Introduction

Modern steel infrastructures are required to have decreased life-cycle costs and increased lives. Thus, steels with high corrosion resistance, as typified by weathering steels, are gaining more importance.[1)] The corrosion resistance of steel is heavily dependent on the structure and characteristics of the rust formed on the steel surface. Hence, Kobe Steel has long established its own technologies for controlling steel rust as a means for improving the corrosion resistance. As a result, the company has newly developed and implemented two types of unique steels for infrastructure. One is for unpainted applications and has higher atmospheric corrosion resistance in chloride environments than conventional weathering steel. The other is for painted bridges, which can prolong the cycle of repainting.[2)] Kobe Steel has conducted various activities in parallel, such as joint studies with government and academia, as well as participation in academic societies, to establish new and unique analysis technologies to support studies on corrosion and the prevention of corrosion in steel for infrastructure. These technologies include rust evaluation using, for example, X-ray diffraction, molecular adsorption and highly brilliant synchrotron radiation. They also include a new approach based on experiments using artificially synthesized rust and neutron radiation to visualize the under-film corrosion of painted steel. They have been serving to substantiate the onset mechanism of corrosion resistance and as guidelines for material development. The following introduces the outline and application examples of these technologies.

1. Rust evaluation technologies for weathering steel

1.1 Quantitative analysis of rust composition based on X-ray diffraction using internal standards

Weathering steel is often regarded as "steel using rust to prevent rusting." It is considered that certain alloying elements serve to form a dense, protective rust layer in the air, exerting excellent atmospheric-corrosion resistance. This implies that the first step in understanding its corrosion resistance mechanism is to know which substances constitute the rust layers. The rust formed on steel is generally recognized to consist of crystalline components, such as α-FeOOH, β-FeOOH, γ-FeOOH and Fe_3O_4, as well as other components regarded as X-ray amorphous. X-ray diffraction (hereinafter "XRD") is an analytical method commonly used for discriminating these substances. In XRD, the subject rust sample may be mixed with a certain amount of known substance, called "internal standard substance", to determine the intensity ratios of the diffraction lines for said substance and the individual rust component, such that each intensity ratio can be collated to its respective calibration curve (prepared in advance) to enable quantification. This technique, however, has not been reported in detail so far. It was against this background that Kobe Steel, collaborating with Kobelco Research Institute, Inc., conducted basic studies including the methods of preparing internal standard substances and rust samples, the conditions of XRD measurement and the method for analyzing data; this, in particular, led to the development of a quantitative XRD for rust using ZnO as the internal standard substance.[3)] It has turned out that ZnO is preferable because its grains are finer and more homogeneous than those of other conventionally used substances, such as CaF_2, and readily mixes with rust samples. **Fig. 1** outlines the experimental procedure. This quantitative method was further submitted to the *SABI*-chemistry study group, Japan Society of Corrosion Engineering, where its accuracy was verified in a round robin test, and its application technology was improved. This method is being used as a de-facto standard.[4)]

An application example of this quantitative method is demonstrated in **Fig. 2** showing the relationship between the thickness loss (corrosion

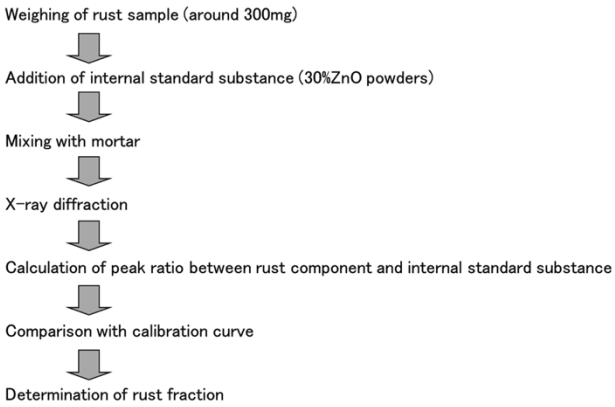

Fig. 1 Experimental procedure of quantitative analysis by XRD of rust composition

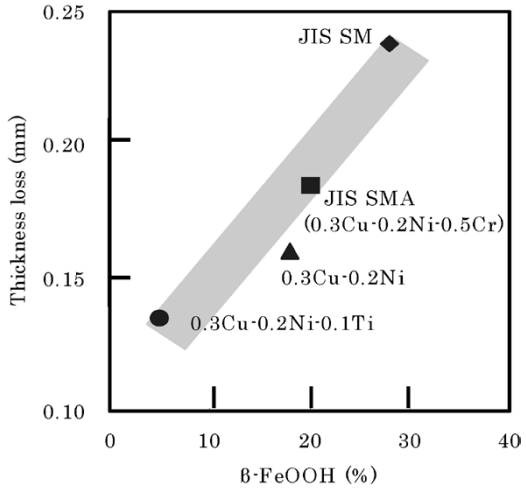

Fig. 2 Relationship between thickness loss and β-FeOOH rust fraction of various steels exposed at Kakogawa Works quay for 1 year

resistance) and rust components of various steels exposed to a chloride environment.[5] The thickness loss correlates with the amount of β-FeOOH rust. The results indicate that proper amounts of alloying elements such as Cu, Ni and Ti suppress the formation of β-FeOOH, classified as a detrimental rust, and improve the resistance against corrosion in a chloride environment.

1.2 Evaluation of specific surface area of rust based on molecular adsorption

A rust layer on steel can be regarded as a porous aggregate consisting of fine particles of individual rust components. Finer rust particles are considered to form a denser, protective rust layer, exerting corrosion resistance. In reality, however, rust particles have various shapes and strongly aggregate; this makes it difficult to determine their sizes quantitatively by, for example, electron microscopy observation or particle size analyzer measurement. The molecular adsorption, on the other hand, makes it possible to obtain molecular size information even from aggregated rust because it uses gaseous molecular probes. With this in mind, Kobe Steel has collaborated with Osaka Kyoiku University and Shimane University to conduct adsorption experiments, using the molecules of nitrogen (N_2) and water (H_2O), on various rusts formed by atmospheric corrosion. Specific surface areas (hereinafter "SAs") were measured which were considered to reflect the particle sizes of the rusts. It was found that the SA can be an evaluation index for the corrosion resistance of weathering steels.

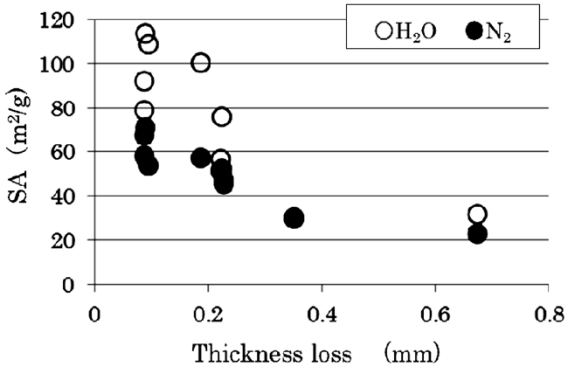

Fig. 3 Plots of specific surface area (SA) of the steel rusts formed by cyclic corrosion test against the decrease in thickness

Fig. 3 depicts, as an example, the SAs obtained by cyclic corrosion testing (CCT) of various weathering steels, plotted against their corrosion resistances (thickness losses).[6] The results show that the SA increases with decreasing thickness loss, indicating that finer rust particles densify the rust layer, improving the corrosion resistance. The results also indicate that the adsorption of water molecules can reflect the denseness of rust more sensitively than nitrogen.

2. Approach based on experiments using artificially synthesized rust

Alloying elements such as Cr, Cu, Ni and Ti are known to densify the rust layers of steel and thus improve the corrosion resistance. A rust layer is an aggregate of particles of individual rust components, as described above, and its performance is affected by environmental factors such as chloride ion, dissolved oxygen and pH. Thus, the formation of rust on steel in real conditions is complex, with various factors interacting complexly with each other, making it difficult to clarify which alloying element works on which rust component to densify the rust. The fundamental improvement of corrosion resistance, however, requires clarification of how individual alloying elements affect the formation

and structure of each rust component. As a new approach to achieving this, Kobe Steel, collaborating with Osaka Kyoiku University and Shimane University, has been conducting experiments on artificially synthesized rust and has established a technology for artificially synthesizing an intended rust composition with intended alloying elements under intended environmental conditions. As a result, the effects of alloying elements and environmental factors on the composition of rust layers are being systematized.

Table 1 shows, as an example, the results of a study on the effects of typical metallic ions on the crystallinity and particle size of each rust component formed under typical rusting conditions.[7] The results show that Cu(II) can densify rust components other than β-FeOOH. It is also shown that Cr(III) has small effects on α-FeOOH and β-FeOOH, but refines γ-FeOOH significantly. Divalent nickel, Ni (II), has little effect on the refinement of β-FeOOH, but refines other rusts, in particular, γ-FeOOH. Unlike other metallic ions, Ti (IV) is found to refine β-FeOOH significantly. In order to densify rust layers and improve corrosion resistance, it appears to be more effective to add combined alloying elements, taking into account the effects of alloying elements and the corrosion environment, rather than adding each element singly. Atmospheric rust formed in a chloride-free environment, for example, mainly contains α-FeOOH and γ-FeOOH. Therefore, it stands to reason that the addition of Cr, Cu, and Ni is indispensable to the conventional weathering steels stipulated in the Japan Industrial Standard (JIS). Chloride environments, on the other hand, give rise to the formation of β-FeOOH and Fe_3O_4, which are regarded as detrimental rusts. Thus, Ti is strongly recommended as an element that inhibits the formation of β-FeOOH and improves the resistance against corrosion in chloride-containing atmospheres. Further addition of Ni and Cu, the elements densifying Fe_3O_4, α-FeOOH and γ-FeOOH, is expected to improve the corrosion resistance even more.

Table 1 Comparison of effects of metal ions on crystallinity and particle size of iron rusts

Rusts		Cu(II)	Cr(III)	Ni(II)	Ti(IV)
α-FeOOH	crystallinity	◎	●	○	*
	particle size	○	○	○	○
β-FeOOH	crystallinity	△	○	○	◎
	particle size	●	○	△	◎
γ-FeOOH	crystallinity	○	○	○	●
	particle size	○	◎	◎	○
Fe_3O_4	crystallinity	○	○	○	○
	Particle size	○	○	○	○
X-ray amorphous	crystallinity	○	○	○	○
	particle size	△	●	△	△

● : rise, △ : unchanged, ○ : fall, ◎ : marked fall
* : double domain particles consisting of an α-FeOOH core and a poorly crystalline shell

3. Application of ultra-bright synchrotron radiation

Synchrotron radiations, having high brightness and wide wavelength windows, excellent in directionality and stability, are recently gaining attention as new X-ray sources that provide analytical information featuring, for example, high resolution and a high S/N ratio. In particular, the large synchrotron radiation facility, SPring-8 (Super Photon-ring, 8 GeV), in Nishiharima, Hyogo in Japan, achieves the world's highest performance and offers brightness more than one hundred million times higher than do conventional X-ray tubes. Kobe Steel participates in promoting the industrial application of SPring-8, exploiting the facility in elucidating the corrosion processes of steel and the structures of rust formed.

Fig. 4 exemplifies the results obtained by the XRD apparatus of the SPring-8 Hyogo Beamline (BL24XU), in which the corrosion process in iron was traced during the beginning stages of wet/dry cycles.[8] This experiment involved dry-polishing a surface of high-purity iron and dispensing a saturated NaCl solution onto the surface every 60 minutes, while measuring in-situ the XRD intensity at a low incidence angle. Here, Fe_3O_4 and FeOOH (presumed to be α-FeOOH) were detected with a higher ratio of Fe_3O_4 immediately after the salt solution was supplied, and with a decreased ratio of Fe_3O_4 as the solution slowly dried naturally. The NaCl solution was replenished 60 minutes later, which increased the ratio of Fe_3O_4 again, and this behavior was repeated thereafter. These behaviors seem to agree with the electrochemical redox model proposed by U. R. Evans, which states that, in wet processes, FeOOH is reduced into Fe_3O_4 by cathodic reduction, which acts as an oxidant to promote the corrosion of iron, while, in dry processes, Fe_3O_4 is oxidized by air into FeOOH: these processes are repeated, promoting atmospheric corrosion.

Fig. 5 shows an example in which the state of Ti (the radial distribution function around Ti) in Ti-added, β-FeOOH rust was analyzed using the X-ray absorption fine-structure (hereinafter "XAFS") apparatus of the SPring-8 Industrial Consortium Beamline (BL16B2).[9] Kobe Steel has recently developed an advanced weathering steel containing nickel, in which a minor quantity of Ti is added to suppress the formation of β-FeOOH rust and

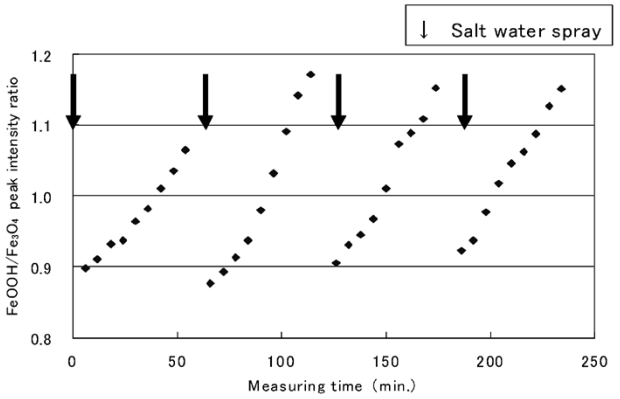

Fig. 4 Time change of $FeOOH/Fe_3O_4$ peak intensity ratio during the iron rust formation process by wet/dry cycle using in-situ SR-XRD observation

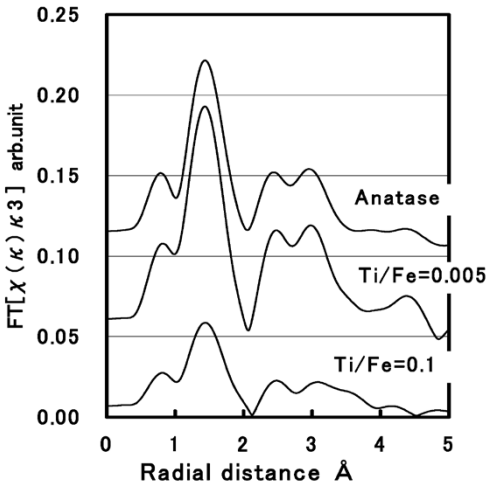

Fig. 5 Radial distribution functions of Ti in Ti-containing β-FeOOH rusts and anatase type TiO_2 obtained from SR-XAFS measurement

thus improve the resistance against corrosion in chloride environments. This development involved the above experiment as well as high-resolution TEM observation. These analyses imply that, in the advanced weathering steel with a minor addition of Ti, nanometer scale particles of anatase-type TiO_2 are formed to promote the refinement of β-FeOOH rust, providing excellent resistance against corrosion in chloride-containing atmospheres. Synchrotron radiation XAFS enables highly sensitive detection of information on local structure and the electronic state around specific elements, regardless of whether the subject is solid or liquid, allowing, for example, studies currently on-going on the action mechanisms of alloying elements in corrosion processes.

4. Application of neutron radiation

Painting is widely used for preventing the corrosion of steel infrastructure; however, with the passage of time, water may penetrate under the coating film through, for example, film defects, which promotes under-film corrosion and eventually causes the coating to blister. Painted steel structures therefore must be repainted periodically, which raises the maintenance cost. Attempts are being made, including the development of heavy duty coating, to prolong the life of coatings. Kobe Steel focused on the densification of rust and pH control at corrosion tips and has developed a unique alloy steel for painted application to deter the progress of under-film corrosion. To further advance this development, the mechanism of under-film corrosion must be elucidated; however, the conventional X-ray analysis tools have insufficient sensitivity to water and low power for penetrating through steel material, limiting the analysis of under-film corrosion. Neutron beams, on the other hand, have penetrating power that is remarkably higher than that of X-rays in principle and has an excellent capability for detecting the water involved in corrosion. Kobe Steel is collaborating with RIKEN, as a part of study-group activities of the Iron and Steel Institute of Japan, to visualize the movement of water inside the blisters of painted steel by a neutron imaging technique using a compact neutron source system, the RIKEN Accelerator-driven Neutron Source (RANS), maintained and upgraded by RIKEN.

Fig. 6 shows examples of the results.[10] Specimens of normal steel (SM400) and alloy steel (0.8Cu-0.4Ni-0.05Ti) were compared. They were coated with modified epoxy paint, and artificial defects were induced into the coating. These specimens were subjected to CCT tests to create blisters of under-film corrosion. These specimens were ① stored in a room for one month after the CCT tests, ② immersed in distilled water for 110 min, and ③ dried by blown air for 30 min using a fan after step ②. These 3 states are compared in the figure. In the naturally dried state (①), contrasts (attenuations of neutron transmittance) due to the defects of rust layer or to the residual water in the coating and steel/coating interface were observed in addition to the rust component (FeOOH) formed under the film. For both steels, these contrasts were found to be enhanced when the specimens were immersed in water (②) and, conversely, found to be weakened when they were dried (③). These changes in contrast are considered to reflect the movement of water (changes in moisture) under the films. Compared with the normal steel, the alloy steel has a localized water-containing region, which makes it easier for water to disappear, so it is less likely to be retained. Water being a direct cause of corrosion, this implies

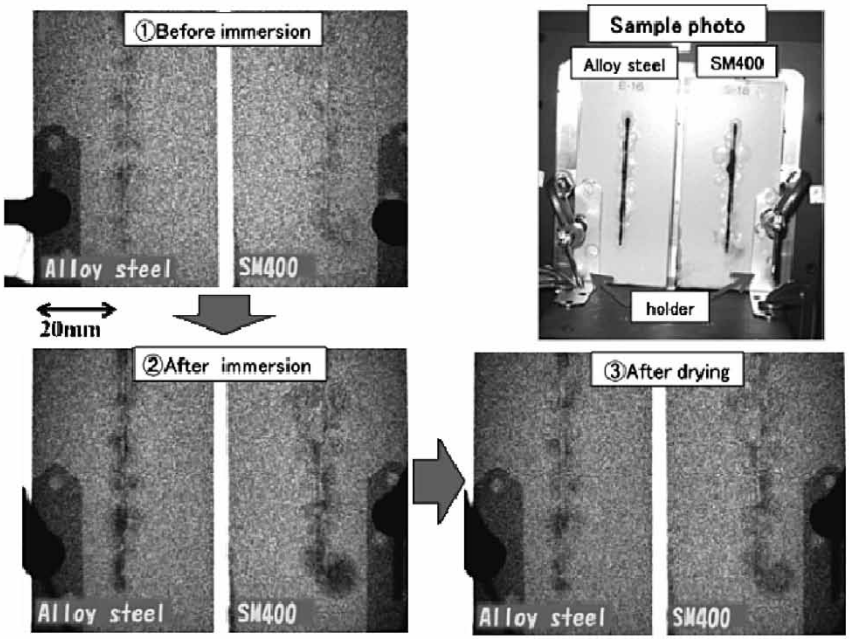

Fig. 6 Neutron images of under-film corroded normal steel (SM400) and alloy steel (0.8Cu-0.4Ni-0.05Ti) during water immersion and drying process

that the alloy steel has excellent resistance against under-film corrosion.

Conclusions

This paper has introduced a few examples of evaluation/analysis technologies that Kobe Steel has worked on to evaluate the corrosion resistance of steel for infrastructure. Neutron beams, in particular, have high penetrating power and excellent capabilities of detecting the water and hydrogen involved in corrosion phenomena and are expected to be used, with synchrotron radiation, for example, in a complementary manner. Infrastructures will be required to have a further decreased life-cycle cost and increased lives, and corrosion-resistant steel is expected to gain more importance. To support this, the technologies for evaluating and analyzing corrosion resistance must be advanced further. We will continue to strive to respond to a variety of sophisticated demands from customers.

References

1) T. Nakayama et al. *Bulletin of the Iron and Steel Institute of Japan*. 2005, Vol. 10, p. 932.
2) T. Nakayama et al. *R&D Kobe Steel Engineering Reports*. 2001, Vol. 51, No. 1, p. 29.
3) T. Iwata et al. *Proc. of JSCE Materials and Environments 1995*, C-306 (1995), 341.
4) T. Nakayama et al. *Proc. of 132nd. Corrosion and Protection Symposium*. 2001, p. 65.
5) T. Nakayama et al. *ESCCD2001*. 2001, p. 201.
6) T. Ishikawa et al. *Materials and Corrosion*, to be published.
7) T. Nakayama et al. *R&D Kobe Steel Engineering Reports*. 2009, Vol. 59, No. 1, p. 13.
8) T. Yasunaga et al. *Proc. of 49th JSCE Materials and Environments*, A-104. 2002, p. 11.
9) T. Segi et al. *X-SEN BUNSEKI NO SHINPO 37*. 2006, p. 325.
10) M. Yamada et al. *TETSU-TO-HAGANE*. 2014, Vol. 100, p. 99.

Steel Plate for Bridges with Long-life Coating (Eco-View)

Dr. Fumio YUSE*1, Masahiro MATSUSHITA*2, Manabu IZUMI*3

*1 Materials Research Laboratory, Technical Development Group
*2 Plate Products Marketing & Technical Service Dept., Iron & Steel Business
*3 Plate Products Development Dept., Research & Development Laboratory, Iron & Steel Business

Kobe Steel has developed new steels which were designed to reduce the life cycle cost of bridges. The newly developed steel plates (Eco-View) showed excellent corrosion resistance in 10-year-exposure test results. The anti-corrosion properties of this newly developed steel (Eco-View), after painting, are better than those of conventional JIS-SM steel plates. Eco-View steel is expected to contribute to the reduction of life cycle costs, because it can prolong the period before repainting, especially in urban areas or, specifically, in harsh corrosive environments.

Introduction

As of April 2013, there were approximately 699 thousand road bridges being maintained in Japan. Many of them were built during the period of high economic growth, with 16% of them having been constructed more than 50 years ago. This ratio will increase to 65% in 20 years, indicating their rapid aging and huge costs incurred for their maintenance and renewal.[1), 2)] Since steel road bridges are typically damaged by corrosion, maintenance, paint coating and corrosion protection are receiving more and more attention, while there has been a rise in the awareness of the extension of life and reduced life-cycle costs in the construction of bridges. Life-cycle cost (LCC) is a concept encompassing all stages, including construction, maintenance and re-building, for which Kobe Steel makes suggestions as to material steel plates. The company has developed, for example, a 1% Ni-Ti weathering steel with high resistance against chloride corrosion, as well as excellent weldability, allowing its use in high-salinity environments without paint coating.[3)]

Paint coating, on the other hand, is indispensable for urban areas that emphasize landscapes and for areas with severely corrosive environments. With this in mind, Kobe Steel has developed a series of steel plates for long-life coating (hereinafter "Eco-View™ note)", which satisfies all the conventional requirements for steels for welded structures (corresponding to Japan Industrial Standard (JIS) G 3106; structural materials (SM)) and, in addition, is itself provided with a function of inhibiting under-film corrosion.[4), 5)] The Eco-View is registered in the New Technology Information System (NETIS.) This paper introduces the results of a ten-year exposure test of the Eco-View[6)] and results of a study on corrosion resistance, as well as its development concept and the mechanism of corrosion-resistance improvement.

1. Features of steel plates for paint coating (Eco-View)

1.1 Development concept

More than 70% of the bridges in urban areas that emphasize landscaping and in areas with high-salinity environments are specified as requiring painting, and usually are made of steel for welded structures (corresponding to JIS G 3106; SM). The steel, however, does not by itself have any effective function of inhibiting corrosion due to rust, and easily permits the rust to progress from defects in paint films. This progression of rusting causes the blistering and peeling of the paint films, which is a factor in determining the life of coating. Painting accounts for 5 to 15% of the total construction cost of a superstructure, and re-painting is estimated to cost as much as the initial painting. Thus the reduction of these costs presents some big challenges.

In attempts to lengthen the cycles of re-painting, new paints have been developed and the coating methods have been improved; however, the progression of corrosion, as well as rusting and the deterioration of paint films, inevitably occurs in portions such as sharp edges that are difficult to manage, and from defects in the paint films (e.g., damage to the coating during service). Corrosion progresses from such defects in the paint film, forming rust and deteriorating the corrosion resistance of the paint film. The Eco-View is a steel material with a function that inhibits such deterioration.

In commercializing the 1% Ni-Ti weathering steel that can be used in high-salinity environments without coating, Kobe Steel adapted its original alloy system, a non-Cr, Cu-Ni-Ti system. A similar technology has been used in the Eco-View as well to improve its corrosion resistance.

In general, Cu, Ni and Cr are regarded as elements that improve corrosion resistance, and

note) Eco-View is the translation of a registered Japanese trademark "エコビュー(pronounced "í:koʊ bjú")" (No. 4631892) of Kobe Steel.

the JIS requires these as indispensable alloying elements for weathering steels. Many years of research, however, have revealed that, in salinity environments, Cr lowers the pH at the corrosion tips and promotes corrosion. Meanwhile, it has been found that a minor addition of Ti is effective in inhibiting the formation of β-FeOOH, which is regarded as less stable and adversely affecting corrosion resistance. In addition, Cu and Ni have been found to promote the formation of amorphous rust, which has a favorable effect on corrosion resistance. On the basis of such knowledge, the content of Cu and Ni has been optimized, without the addition of Cr, and with a minor addition of Ti, to improve corrosion resistance by the densification of the rust that formed.[3), 4)]

Fig. 1 shows the mechanism assumed to occur in improving the corrosion resistance of paint films on the Eco-View. This mechanism is expected to work to inhibit under-film corrosion even when corrosion originates in defects in paint films. The chemical composition of the Eco-View is shown in **Table 1**. The menu covers all the steel plates with tensile strengths of 400-570 MPa class used for ordinary steel bridges. The Eco-View steels have compositions within the range stipulated by JIS SM so as to secure satisfactory performance as steel for welded bridge structures. Thanks to the low carbon content, and despite the addition of elements such as Cu and Ni, the Pcm (the critical metal parameter for weld cracking) is as low as 0.19% or less, which is lower than 0.21%, the criterion for allowing decreased preheating. Furthermore, all the steel plates have sufficient strength and toughness. Therefore, no special processing is necessary for adopting the Eco-View to actual bridges.

1.2 Application records

The former Japan Highway Public Corporation applied the Eco-View to the bridges on the Minami-Hanna road, including the Hyoge daiichi-kyo bridge and Takeuchi-bashi bridge (**Fig. 2**), as well as bridges on the Joshinetsu Expressway, including the Kannonsawagawa bridge. The Eco-View has also been used for more than ten bridges built, for

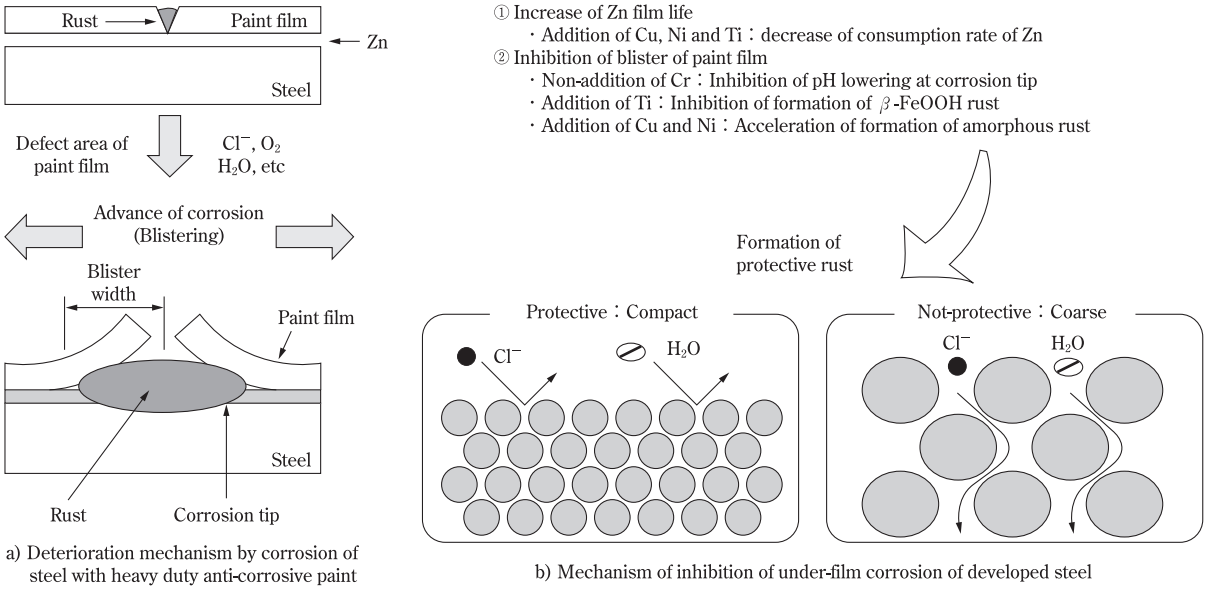

Fig. 1 Mechanism of inhibition of under-film corrosion on Eco-View

Table 1 Chemical compositions of Eco-View

Steel Class	Thickness (mm)	Chemical compositions (%)							Ceq (%)	P_{CM} (%)
		C	Si	Mn	Cu	Ni	Cr	Ti		
400MPa	25	0.05	0.30	0.65	0.78	0.41	0.01	0.045	0.24	0.14
490MPa	25	0.06	0.30	1.24	0.74	0.38	0.01	0.042	0.35	0.18
	50	0.05	0.32	1.56	0.79	0.41	0.02	0.046	0.40	0.19
570MPa	50	0.05	0.30	1.54	0.77	0.39	0.02	0.041	0.39	0.19

Note) 1) Ceq=C+Mn/6+Si/24+Ni/40+Cr/5+Mo/4+V/14+(Cu/13)
(Cu: applied when Cu≧0.50%)
2) P_{CM}= C+Si/30+Mn/20+Cu/20+Ni/60+Cr/20+Mo/15+V/10+5B

Fig. 2 Takeuchi-bashi Bridge of Minami Hanna Road

example, by local governments.[7] Since the Minami-Hanna road is a highway running through ancient cities, particular attention was paid to the scenery, which included involving specialists in determining the colors. There are six bridges, each with two girders, on this highway in the Taima district. A total of approximately seven-hundred tonnes of the Eco-View was used for these bridges to lengthen the cycles of re-painting. The Takeuchi-bashi bridge is the largest of the six bridges, and its particulars are as follows:

Ordering party: The Japan Highway Public Corporation (NEXCO West Japan)
Place of erection: Nara prefecture
Year of erection: 2002
Type: 4-span continuous composite 2-main-girder steel bridge
Length: 160 m (span lengths; 41.25 + 41.4 + 41.4 + 34.44 m)
Amount of steel used: Approximately 310 tonnes
Features: Eco-View + thin-film heavy-anticorrosion coat (I-coating system).

2. Corrosion resistance of coating

The effect of the Eco-View has been verified by exposure tests conducted at the Hyoge daiichi-kyo bridge near the Takeuchi-bashi bridge. This section reports the results of a 10-year exposure test.

2.1 Study outline

Since 2003, an exposure test has been in progress at the Hyoge daiichi-kyo bridge on the Minami-Hanna road. Small samples of ordinary steel (SM490) and the Eco-View were placed on the inspection catwalk of this bridge. Each small sample (150×70×6 mm) was sealed with tape on its sides and back, and the I-coating system (organic zinc, 75 μm; polyurethane resin, 30 μm; polyurethane resin, 25 μm: Total 130 μm), used in the construction of this bridge, was applied to the test surface. In order to simulate the paint scratches and sharp edges where rusting tends to begin, defects were artificially introduced into the paint film after curing, using a cutter knife. For comparison, a non-painted sample was provided on the same exposure stand. The appearance of one of the test samples and of the exposure test situation are shown in **Figs. 3** and **4**, respectively.

After ten years of exposure, each sample was inspected (for cracks and peeling in the painted

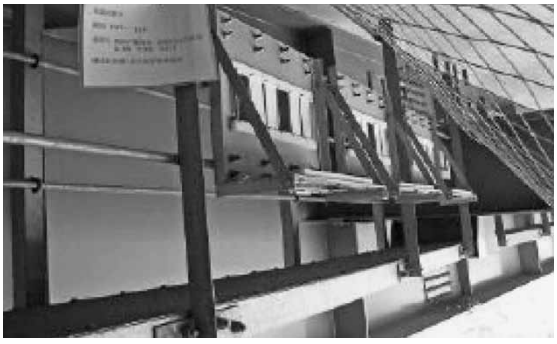

Fig. 4 Exposure test

	I-paint system		Appearance
Number of painting processes	3		150×70×6mm With artificial film defect (scratch)
Film thickness	130 μm		
Applicable regions	Urban regions		
Details of paint films	Polyuretane resin	Top-coat (55μm)	
	Organic Zn	Under-coat (75μm)	
	Primer		
	Steel		

Fig. 3 Coating system and appearance of test samples

portion) and the blister width on the artificial film defect was measured. To measure the blister width, the cut portion was divided into 5 equal sections, and the maximum value was measured for each of the sections. For some coated samples, paint films were removed using a peeling agent. These samples were cut for cross-sectional scanning electron microscope (SEM) observation and electron probe micro analyzer (EPMA) analysis. The rust on the non-painted sample was removed and subjected to X-ray diffraction (XRD) for its identification and quantification.

2.2 Results for painted samples

Fig. 5-left shows the samples (placed horizontally; dust removed) of ordinary steel and the Eco-View after the exposure test. Neither rust, nor blister of paint film, was observed on either steel. Fig. 5-right shows the blister width determined for each artificial defect in the paint film. The blister width tends to be greater for the horizontally-placed samples than for the ones placed vertically. This is attributable to the fact that the horizontally-placed samples can collect moisture and dust more easily, which promotes corrosion.

It has turned out that Eco-View has a blister width that is, on the average, smaller by 10% or more than that of the ordinary steel.

Fig. 6 shows the surfaces of the steels after removing the paint films. The degree of corrosion for each of the steels indicates that the Eco-View offers superior corrosion resistance.

2.3 Results of cross-sectional observations

Fig. 7 shows the cross-sectional SEM images with EPMA (Cl) mapping. They indicate that in the ordinary steel, chlorine ions (Cl^-), a corrosion factor, exist at the tip of the rust (i.e., the interface on the side of the iron), while in the Eco-View, they stay in the outer surface of the rust layer, showing that the penetration of Cl^- has been effectively inhibited. The result indicates that the Eco-View effectively prevents under-film corrosion, resulting in the smaller width of the blister from the film defect.

2.4 Results of XRD analyses of rust

Since the amount of rust on the corroded portion of the painted sample was too small to be analyzed, the XRD analysis was performed on rust collected from the non-painted sample exposed in the same manner as the painted samples. The analysis focused on β-FeOOH, which is characteristically

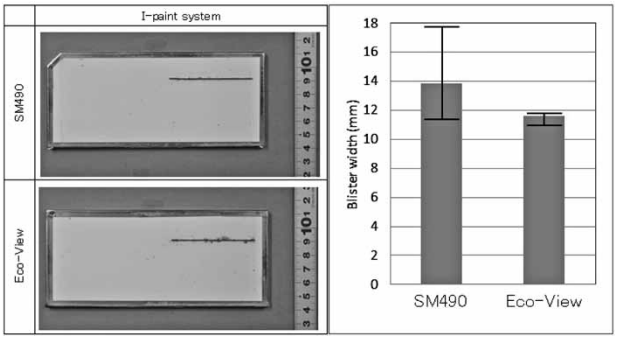

Fig. 5 Appearance and blister width of painted steels

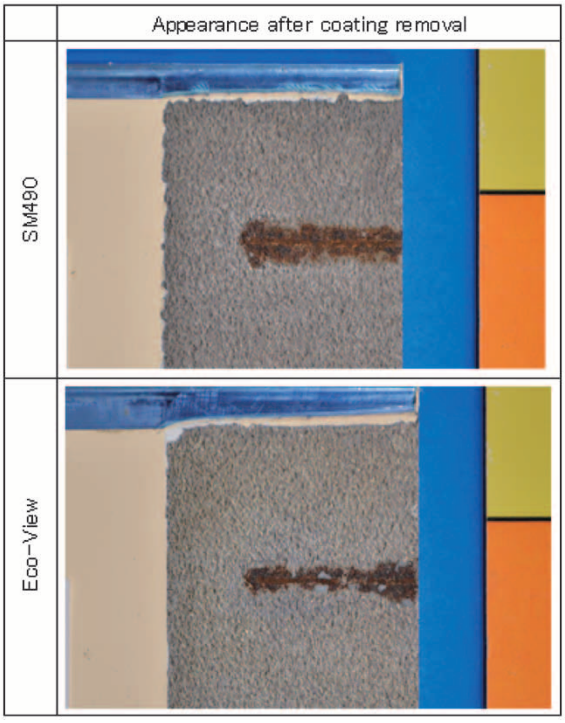

Fig. 6 Appearances of the test pieces after coating removal

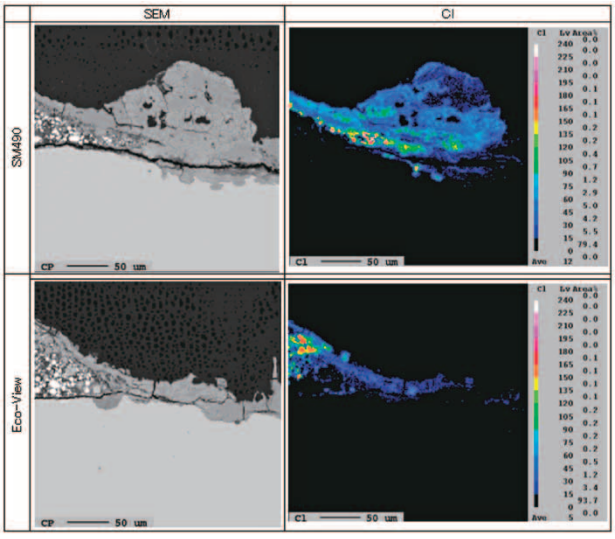

Fig. 7 Cross-sectional images of SEM and EPMA of Cl

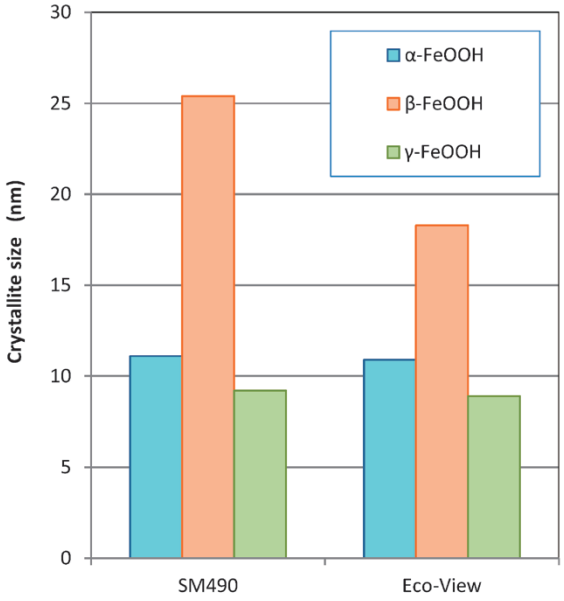

Fig. 8 Crystallite size of SM490 and Eco-View

formed in chloride environments and adversely affects the corrosion resistance. The Eco-View has approximately half the amount of β-FeOOH, compared with the ordinary steel.

To quantitatively evaluate the crystallinity, the crystallite sizes were determined on the basis of Scherrer's equation using the half-peak width of the XRD peaks. The results are shown in **Fig. 8**. The Eco-View has β-FeOOH with a crystallite size that is approximately 30% finer, indicating that the addition of Ti can effectively refine β-FeOOH.

3. Discussions

A chloride environment leads to the formation of a significant amount of β-FeOOH, known as detrimental rust. Titanium (Ti) is an element considered to be effective in interrupting the formation of β-FeOOH and improving the corrosion resistance through its refinement.[8] The current testing of small samples exposed to an actual environment has confirmed the advantage, in terms of blister width, of the Eco-View. The results show that the optimized composition, including no addition of Cr and the addition of Ti, Cu and Ni, inhibits the corrosion at the tip of the under-film corrosion and densifies the rust formed, so as to inhibit the penetration of corrosion factors. This is considered to verify the validity of the mechanism originally assumed.

In a past experiment, the post-coating corrosion resistance of the Eco-View was evaluated for different coating systems. The results showed that, for the A-coating system, which is used for the general environment, the Eco-View exhibited a greatly inhibited progression of rust from defects in the paint film, as well as a significantly reduced blister width in the paint film, compared with conventional steel. For the C-coating system (a heavy corrosion-protection coating system), used for harsh coastal environments, the results showed a reduced blister width and confirmed the effectiveness of sacrificial protection by zinc.[4]

The corrosion protection of road bridges made of steel used to be provided by the A-coating system, consisting of rust-inhibiting red lead primer and phthalic resin coating. The coating system is being changed to a heavy corrosion-protection system including a zinc-rich primer and a final coating of polyfulorocarbon for atmospheric isolation. Yet, however excellent the coating system may be in its anti-corrosion function, corrosion may occur and spread from the corners of parts, where the films are not thick enough, or from scratches and defects. Once the sacrificial protection effect of zinc disappears after a long period of time, the corrosion of the base iron may occur and spread from such portions. Here, the mechanism shown in Fig. 1 is considered to apply in the same manner. The 10-year exposure test conducted this time was performed on the I-coating system (a thin-film type, heavy corrosion-protection coating system) in a mild environment. Therefore, there was not much difference between the different steels. In the future, however, when corrosion has progressed further, the effect of alloying elements, as described above, will become clearer, accentuating the difference between different steels.[4]

Considering the experimental results this time, the Eco-View is expected to lengthen the cycles of re-painting and reduce the life-cycle cost of bridges for which the re-painting cycles are regulated due to damage in the paint films.

Conclusions

A 10-year exposure test was conducted on an actual bridge. The results show that the "Eco-View", a steel plate for bridges with long-life coating, exhibits excellent resistance against coating corrosion compared with ordinary steel. The results, including the results of rust analysis, indicate that the mechanism of inhibiting under-film corrosion is working as expected. The Eco-View is expected to enable re-painting cycles to be lengthened and reduce the life-cycle cost of steel bridges. Kobe Steel will continue to accumulate more data on corrosion resistance for an extended period of time and data on corrosion occurring in different environments.

Finally, our special thanks are due to West

Nippon Expressway Company, Kansai Office and Hanna Highway Office for their cooperation in the long-term exposure test.

References

1) S. Takagi. *KYOURYOU-TO-KISO (Bridges and Foundations)*. 2014, No.9, p.33.
2) T. Tamakoshi et al. *Report of General Studies on Land and Infrastructure Management*. Ministry of Land, Infrastructure, Transport and Tourism. 2006, No.294, p.1.
3) H. Kawano et al. *R&D Kobe Steel Engineering Reports*. 2002, Vol.52, No.1, p.25.
4) S. OKANO et al. *R&D Kobe Steel Engineering Reports*. 2002, Vol.52, No.1, p.39.
5) F. Yuse et al. *The 55th annual conference of the Japan Society of Civil Engineers*. 2001, I-A234.
6) A. Takahashi et al. *The 69th annual conference of the Japan Society of Civil Engineers*. 2014, V-459.
7) N. Furukawa et al. *R&D Kobe Steel Engineering Reports*. 2003, Vol.53, No.1, p.47.
8) T. Ishikawa et al. *Zairyo-to-Kankyo*. 2003, Vol.52, No.3, p.140.

Welding Process and Consumables Aimed at Improving Fatigue Strength of Joints

Minoru MIYATA*1, Reiichi SUZUKI*1

*1 Welding process Dept., Technical Center, Welding Business

The fatigue of steel structures, an important problem, is mainly attributable to stress concentration and tensile residual stress at their weld toes. In order to improve the fatigue resistance of welds, welding consumables, called low-temperature transformation (LTT) consumables, have been developed and their effectiveness demonstrated. Conventional LTT consumables, however, contain large amounts of Ni, posing problems of high cost, poor mechanical properties and low cracking resistance, which has hindered their widespread use. With this in mind, a study was conducted to replace Ni with Mn, which confirmed that Mn can more effectively improve fatigue resistance than Ni. Two newly developed consumables, "TRUSTARC™ MX-4AD" and "TRUSTARC™ LB-3AD", exploit Mn to improve the crack resistance and reduce cost. When used for additional beads, these welding consumables were confirmed to improve the fatigue resistance as well as or better than other methods such as grinding treatment, a standard method for increasing fatigue strength, or peening treatment, which is becoming widespread.

Introduction

Lately, many steel bridges, such as those on the Tokyo Metropolitan Expressway, are suffering from fatigue cracks due to aging, posing a serious problem. A weld is a portion that can deteriorate structural fatigue resistance due to the stress concentration at the weld toes as well as residual stress. Thus, the technology for improving the fatigue resistance of welds is being looked to with great expectation.

The current techniques for improving the fatigue resistance of welds include grind finishing the shapes of the weld toes to relax stress concentration and peening the welds to introduce compressive residual stress.[1] These methods, however, are causing a huge burden due to their low work efficiency and the special apparatuses required.

As a technique for improving fatigue resistance by means of welding consumables, a method has been developed which involves special welding consumables, called low transformation temperature (hereinafter "LTT") welding consumables.[2)-4)] The LTT welding consumables developed so far, however, are significantly inferior to general welding consumables in terms of consumable cost, mechanical performance and resistance against cracking (delayed cracking and hot cracking), and have not been fully implemented yet.

In order to solve these problems and to develop LTT welding consumables that can effectively improve fatigue resistance, Kobe Steel proposed new composition systems that are different from the ones for the conventional LTT welding consumables. On the basis of newly gained knowledge, the company has started manufacturing two products, the TRUSTARC™ note) MX-4AD (hereinafter "MX-4AD"), a flux-cored wire (FCW) for fillet welding that is widely used in the bridge industry, and the TRUSTARC LB-3AD (hereinafter "LB-3AD"), a shielded metal arc-welding rod superior in all-position welding. This paper introduces these products.

1. Mechanism of improving fatigue resistance by using LTT welding consumables

The technology of LTT welding consumables exploits the phase-transformation expansion of weld beads during the cooling process in relaxing the tensile residual stress caused by welding. As shown in **Fig. 1**, a conventional welding consumable undergoes phase transformation at a temperature of 700℃ or higher, and the thermal contraction of the weld bead after the transformation is restrained by the base material, inevitably causing tensile residual stress. An LTT welding consumable, in contrast, has a transformation-start temperature of 500℃ or lower, allowing the transformation expansion of the weld bead to continue at temperatures closer

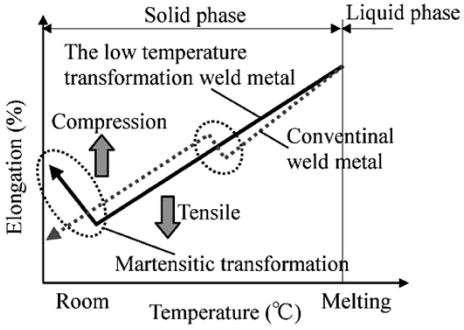

Fig. 1 Mechanism of introducing compressive residual stress around weld bead by low-temperature transformation

note) TRUSTARC (TRUSTARC™) is a trademark of Kobe Steel.

to the ambient temperature, which enables weak tensile/compressive residual stress to remain after the welding. Many studies have been conducted on the transformation-start temperatures (hereinafter "Ms points") of iron and steel, which, for example, are expressed by Equation (1):[5]

$$\text{Transformation-start temperature (℃)} = 529 - 382\times(\%C) - 31\times(\%Mn) - 18\times(\%Ni) - 9\times(\%Mo) - 5\times(\%V) - 33\times(\%C)\times(\%Cr) \quad \cdots\cdots (1)$$

This equation indicates that the transformation-start temperature can effectively be lowered by the addition of elements such as C, Mn, Ni and Cr. Each LTT welding consumable developed so far contains approximately 10% of Ni as the main alloying element, which lowers the transformation-start temperature to 200℃ or below.[6] However, although Ni is effective in lowering the transformation-start temperature, the element deteriorates the resistance against hot cracking, excessively raises the strength of weld beads and increases the cost of welding consumables. This has been hindering the more widespread use of LTT welding consumables. Now, Kobe Steel has developed LTT welding consumables while actively exploiting Mn, which substitutes for Ni and is just as effective in the lowering transformation-start temperature.

2. Additional-welding process

Regardless of its composition system, an LTT welding consumable has the feature of producing a weld bead with high strength and low toughness. This feature contributes to the improvement of the fatigue characteristics of joints; however, it may cause the brittle fracture of welds and deteriorate the resistance against delayed cracking. The drawbacks, therefore, cannot be resolved by simply replacing conventional welding consumables with LTT welding consumables. Hence, the practical use of an LTT welding consumable requires development that takes into account the method of its application.

According to the specifications for highway bridges, the weld toes of fillet joints, including cruciform joints and gusset-plate joints, are easily subject to stress concentration and particularly tend to become the origins of fracture.[7] The application of LTT welding consumables to such parts can be effective in improving the fatigue characteristics. As shown in **Fig. 2** (a), however, when a horizontal plate is abutted against a vertical plate (rib) and the intersection is welded with partial joint penetration to form main beads, by fillet welding, for example, a significant stress concentration occurs at the roots as well as at the toes. As a result, applying an LTT welding consumable to a main bead may lead to cracking at the root, increasing the risk of the structure collapsing in a brittle manner (Fig. 2 (b).) In an attempt to resolve these problems, main beads were formed by a conventional welding consumable for 490 MPa class steel to create a sound weld joint, and an LTT welding consumable was overlaid onto the weld toes of the main beads to relax the tensile residual stress there. This method, so called additional welding, is depicted in Fig. 2 (c) and **Fig. 3**.

Additional welding is also expected to relax the macroscopic stress concentration, thanks to the increased throat depth and leg length of the weld.

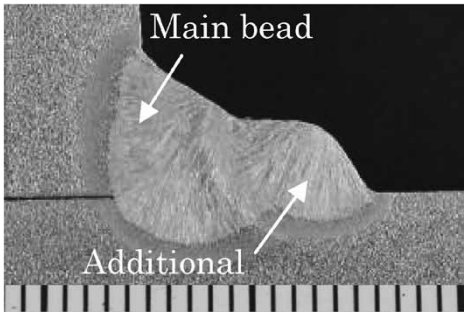

Fig. 3 Cross-sectional shape of additional weld

		(a) Conventional welding joint	(b) Welding joint using LTT welding consumables as main bead	(c) Welding joint using LTT welding consumables as additional bead
		Geometric stress concentration Root Toe Conventional welding consumable	Root Toe LTT welding consumable	Conventional Welding consumable LTT welding consumable
Root	Crack resistance and Toughness	Good	Poor	Good
Toe	Residual stress	Tensile	Compression	Compression
	Fatigue strength	Low	Improve	Improve

Fig. 2 Fillet welding process to balance ①fatigue strength with ② crack resistance and toughness

3. Study on improving fatigue resistance by addition of Mn to welding consumables

3.1 Composition of welding consumables tested

Table 1 lists the flux-cored wires used for the test. The main beads were formed by the FAMILIARC ™ note) MX-200 (hereinafter "MX-200"), a product of Kobe Steel, and comparisons were made with reference to it. This welding consumable is the most widely used of the consumables used for the fillet welding of 490 MPa class steels. In order to verify the improvement effect of Mn and Ni on fatigue resistance, tests were conducted on trial FCWs (B - E) that are based on MX-200 and contain various amounts of Mn and Ni.

These test materials were subjected to Formaster testing to measure their transformation temperatures, which confirmed that both Mn and Ni have the effect of lowering the transformation temperature, as known previously. **Fig. 4** compares consumables containing 5% of Mn and Ni respectively. This figure indicates that, compared with Ni, the addition of Mn results in a greater expansion of the deposited metal at the ambient temperature. Thus, a positive addition of Mn is expected to cause compressive residual stress and to improve the fatigue resistance.

Table 1 Mn and Ni content (%) in all-deposited metal and Ms point

Wire	Mn	Ni	Ms point (℃)	Purpose
MX-200	1.7	0	670	Base
FCW B	2.1	3.1	490	Increasing Ni from MX-200
FCW C	2.0	5.2	390	Increasing Ni from MX-200 and FCW B
FCW D	3.6	0	490	Increasing Mn from MX-200
FCW E	5.5	0	310	Increasing Mn from MX-200 and FCW D

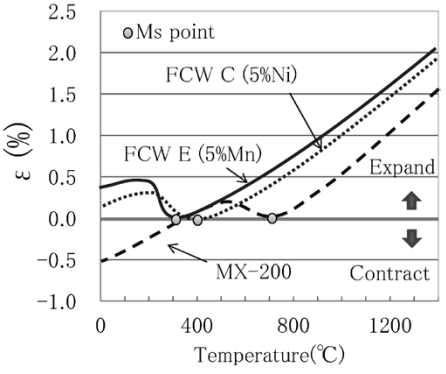

Fig. 4 Relationship between temperature and expansion of conventional welding consumable, FCW C and FCW E

note) FAMILIARC (FAMILIARC™) is a trademark of Kobe Steel.

3.2 Methods of residual stress measurement and fatigue test

Base plates of SM490YA (thickness, 12 mm) were joined by double-sided fillet welding to prepare joints as shown in **Fig. 5**. Each joint was subjected to the measurement of residual stress at its weld toe and to a three-point bending fatigue test. It should be noted that, as shown in **Table 2**, all the test joints employed MX-200 to their main beads, while adopting MX-200, FCW B, FCW C, FCW D and FCW E, respectively on their additional welds. The welding conditions were as follows: welding current, 280 A; welding speed, 450 mm/min; and shielding gas, 100% CO_2.

Each test joint, as prepared, was subjected to X-ray residual stress measurement to determine its surface residual stress at its weld toe. This measurement was conducted at the center in the direction of the weld line. The measuring point was 0.5 mm from the weld toe (**Fig. 6**.)

The specimens for the fatigue test were prepared as shown in **Fig. 7**, and a three-point bending fatigue test was conducted with a stress ratio of 0.1. The nominal stress was calculated in accordance with Equation (2):

Nominal stress σ (MPa) = $3PL / 2wb^2$ ····· (2)

P : test load (N), L : support span (mm),

w : plate width (mm), b : plate thickness (mm)

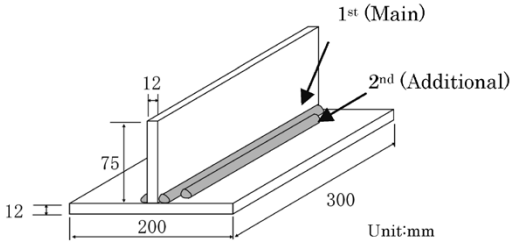

Fig. 5 Test joint and its dimensions

Table 2 Combination of welding wires

Main (1st)	Additional (2nd)
MX-200	MX-200
	FCW B
	FCW C
	FCW D
	FCW E

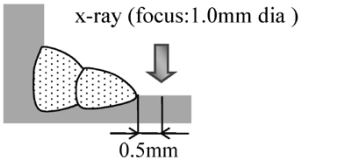

Fig. 6 Schematic of residual-stress measuring point

3.3 Effect of Mn addition on relaxation of tensile residual stress and improvement of fatigue resistance

Fig. 8 shows the results of the residual stress measurements at the weld toe of the T-shaped fillet joints. For each 2% increase in the amount of Ni added in the all-deposited metal, the compressive residual stress at the weld toe increases by 20 MPa. In contrast, for each 2% increase in the amount of Mn added, the stress increases by approximately 50 MPa, indicating that this element makes a greater contribution than Ni to the provision of compressive residual stress.

Moreover, the fatigue resistance of joints improves with the addition of Mn and/or Ni, as shown in **Fig. 9**. For convenience, a regression analysis was performed on the 10^5 cycle strength, which yielded Equation (3). This equation implies that, compared with Ni, Mn has approximately twice the effect on the improvement of fatigue resistance.

10^5 cycle strength (MPa) = 390 + 32 × (%Mn) + 18 × (%Ni) ····· (3)

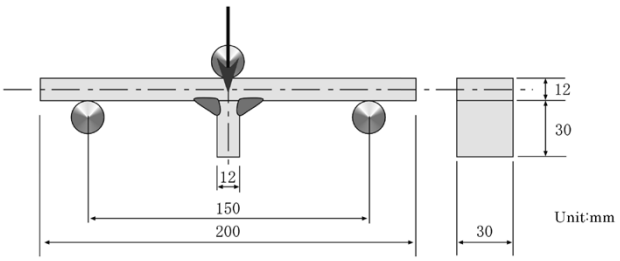

Fig. 7 Schematic of specimen for bending fatigue test

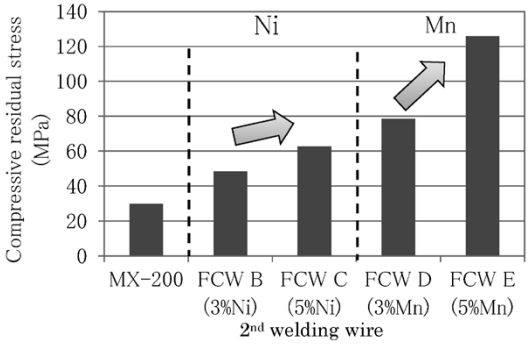

Fig. 8 Effect of Ni and Mn content on residual stress on surface of base metal nearby weld toe

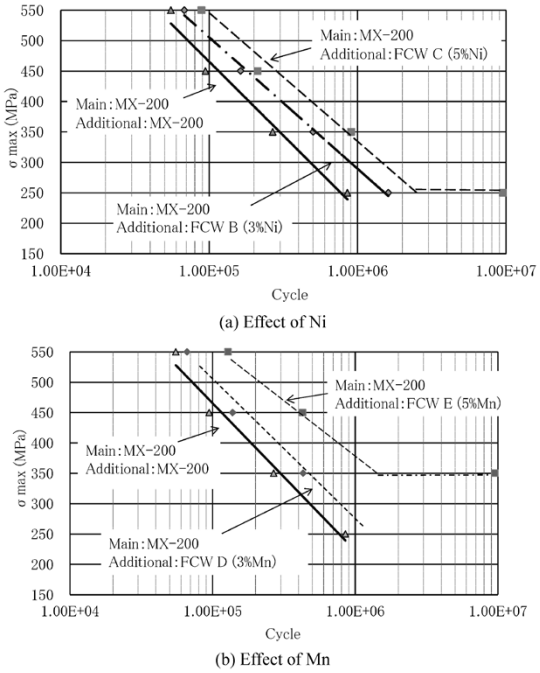

Fig. 9 Improvement of bending fatigue strength by increased addition of Ni and Mn

(Mn: 1.7 − 5.5 wt%, Ni: 0 − 5 wt%, N = 5 , R = 0.99, R2 = 0.98, Standard error = 6.7)

4. Welding consumables, MX-4AD and LB-3AD, for improving fatigue resistance

4.1 Performance of MX-4AD and LB-3AD

When putting an LTT welding consumable into practice, a necessary and sufficient degree of toughness (47 J at 0℃) must be secured with favorable hot cracking resistance under practical conditions. The welding consumables developed this time, MX-4AD and LB-3AD, contain adjusted amounts of Mn and Ni and are designed to satisfy these requirements (**Table 3**.)

In general, the FCWs of carbon steel systems contain slag sources (oxides), which tend to be left in weld beads as inclusions, making the weld beads low in toughness. Against this backdrop and taking into account the balance between toughness and fatigue strength, the MX-4AD has a Mn content

Table 3 Chemical compositions, Ms points, and mechanical properties of all-deposited metals and results of hot crack test* for developed welding consumables

	Chemical compositions (wt%)						Ms point	YS	TS	El.	absorbed energy	Result of
	C	Si	Mn	Ni	Cr	O	(℃)	(MPa)	(MPa)	(%)	at 0℃ (J)	hot crack test*
MX-4AD	0.029	0.38	4.3	-	-	0.069	472	727	820	23	53	No crack
LB-3AD	0.034	0.41	3.3	3.3	-	0.019	408	895	973	20	72	No crack

*According to JIS Z 3155 FISCO test

※MX-4AD: Welding current 280A-Welding speed 300 and 600 mm/min
LB-3AD : Welding current 140A-Welding speed 150 and 300 mm/min

of approximately 4% in deposited metal. Low-hydrogen covered arc-electrodes, on the other hand, result in low oxygen and less inclusion, thanks to the strong deoxidant contained in the applied flux, which results in weld beads with higher toughness than that obtained by FCW. This, as a result, raises the upper limit for the additive amount of Mn + Ni. In the case of LB-3AD, sufficient toughness and favorable hot-cracking resistance have been secured even with its composition of 3% Mn - 3% Ni in the deposited metal. It should be noted that the hot cracking resistance was evaluated in accordance with JIS Z 3155, based on the restrained weld cracking test with C-type jig (FISCO cracking test). The existence/non-existence of cracks was evaluated at constant regions excluding starts and craters.

As shown in **Fig.10**, the transformation-start temperatures (Ms points) are significantly lower for the MX-4AD and LB-3AD than for the MX-200, a welding consumable of 490 MPa class. In particular, the LB-3AD, containing larger amounts of alloying elements, exhibits a greater transformation expansion at the ambient temperature and is expected to improve fatigue resistance significantly.

4.2 Effect of MX-4AD and LB-3AD on improving fatigue resistance of joints

To study the effect of MX-4AD and LB-3AD on the improvement of the fatigue resistance, T-shaped fillet joints as shown in Fig. 5 were prepared in a manner similar to that described in the previous section. The MX-200 was used for the main beads, while the newly developed LTT welding consumables were used for the additional weld. The joints thus prepared were subjected to the measurements of residual stress at their weld toes and to the three-point bending fatigue test. For comparison, a T-shaped fillet joint prepared using MX-200 was used as a test joint with its weld toe processed by peening, and another joint prepared in the same manner was used as a test joint with its weld toes ground to smooth surfaces. Here, the pin-tip radius for the peening was 2.5 mm, and the weld toe radius after the grinding finish was 4.5 mm. The appearances of these weld toes are shown in **Fig.11**.

Fig.12 shows the results of the residual stress measurement. Comparing the residual stresses at the weld toes of beads, the T-shaped fillet joint with the main beads consisting only of MX-200 exhibits a tensile residual stress, while the ones with additional welds made of the newly developed LTT welding consumables exhibit large compressive residual stresses. Furthermore, the LB-3AD exhibits compressive residual stress significantly increased by the peening in the immediate vicinity of the weld toe.

Fig.13 summarizes the effect of each process on the improvement of fatigue resistance. The MX-4AD brings about an improvement that almost equals that achieved by a grinding finish. Thus it is expected that replacing the grinding work, which is extremely low in efficiency, with additional welding using the MX-4AD will shorten the work time. The LB-3AD, on the other hand, almost doubles the fatigue life compared with peening and is expected not only to shorten the work time, but also to improve fatigue

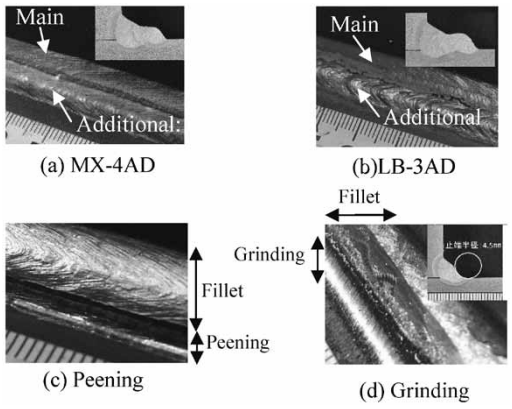

Fig.11 Bead appearance after each treatment

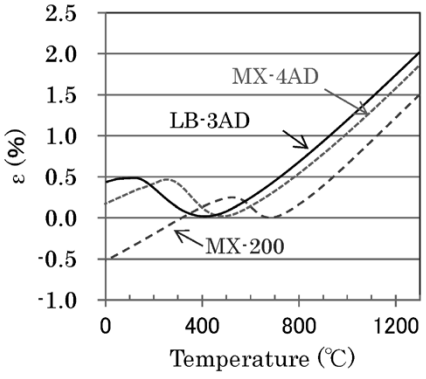

Fig.10 Relationships between temperature and expansion of developed welding consumables

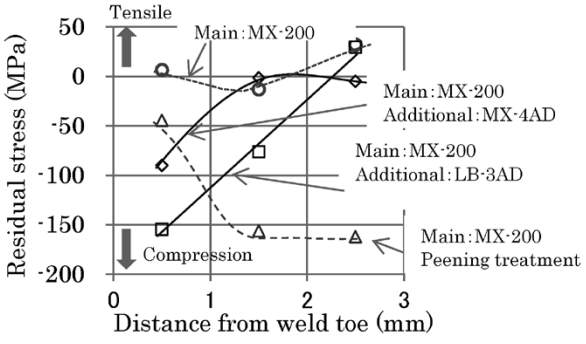

Fig.12 Comparison of residual stresses near weld toes of main beads made of various welding consumables

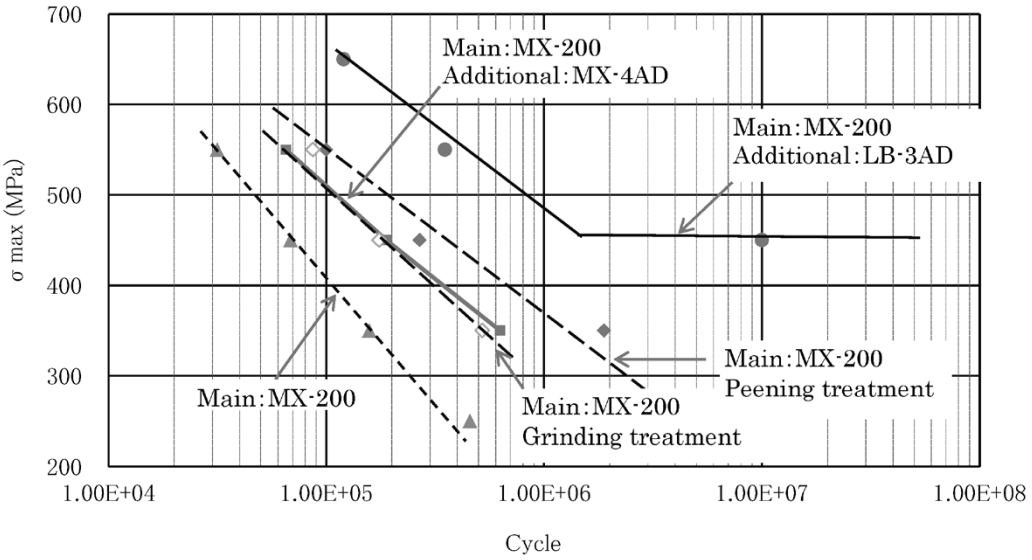

Fig.13 Comparison of bending fatigue strength of each treatment

resistance much more significantly than the current methods.

Conclusions

A study was conducted on the positive addition of Mn to develop new LTT welding consumables, and its effect was confirmed in this paper. The study has led to the manufacturing of two welding consumables, MX-4AD and LB-3AD, for additional welding to improve fatigue resistance. These consumables are advantageous in that the MX-4AD can replace the grinding finish and shorten the work time, while, the LB-3AD can improve fatigue resistance significantly and extend the life of structures better than conventional processes.

Kobe Steel will strive to promote the implementation of these welding consumables and to exploit its own welding consumables and welding system to contribute to the provision of a safe and secure social infrastructure.

References

1) T. Nose. *Journal of the Japan Welding Society (Journal of JWS)*. 2008, Vol.77, No.3, pp.6-9.
2) M. Nishio et al. *the Japan Society of Civil Engineers, The 68th Annual Conference Abstracts 2013-9-4/6*. 2013, pp.1109-1110.
3) C. Miki et al. *Journal of Japan Society of Civil Engineering*. 2002, No.710/I-60, pp.311-319.
4) T. Tominaga et al. *Journal of Japan Society of Civil Engineering*. 2010, Vol.66, No.4, pp.653-662.
5) Y. Ippongi et al. *Bulletin of the Kyushu Institute of Technology*. Science and technology 53, 93-98, 1986-09.
6) T. Kasuya. *Welding Technology*. 2014, Oct, pp.45-49.
7) Japan Road Association. *Specifications for Highway Bridges Commentary*. 2012, pp.200-206.

Development and On-site Construction of GRID NET™ -Grid-type Sabo Dam for Debris Flows of Small Boulders-

Akihiko TAKANO*1, Hiroshi MORIYAMA*1, Takanori KAWAMURA*1, Takuya SAEKI*1, Keita KAGOHASHI*1
*1 Steel Structures & Sabo Division, Engineering Business

The deployment percentage of sabo dams is insufficient for ensuring the safety and protection of human lives against sediment disasters. Therefore, there is a great need for open-type steel sabo dams that have more than twice the sediment-trapping capacity of closed-type sabo dams. However, due to problems with their debris flow trapping capability and with their construction, open-type steel dams have not been used to counter debris flows comprising mostly of small boulders. To address this problem, we have developed GRID NET™, a Kobe Steel-manufactured grid-type sabo dam with a mesh of rings attached to the upstream side that is capable of trapping such debris flows, and so far we have constructed four sabo GRID NET dams. This paper describes the development and construction of GRID NET.

Introduction

The grid-type sabo dam manufactured by Kobe Steel is one kind of open-type steel sabo dam that is constructed from factory-prefabricated steel pipe members with diameters of 508 mm and 609.6 mm and assembled in a three-dimensional grid. By allowing sediment to pass through during low and medium flows to preserve trapping capacity for debris flows, the open-type steel dam is designed to trap large boulders that characteristically accumulate at the front of a debris flow, thereby ensuring a debris flow trapping capacity two to three times greater than a traditional concrete gravity dam.

This capability translates into fewer open-type steel dams being needed to handle debris flows than concrete gravity dams.

At present, the number of sabo dams is still insufficient since approximately only 20% of the needed anti-debris flow dams have been deployed, underlining the need for prompt installation of sabo dams to protect human lives from sediment disasters. However, due to the high construction costs and long construction times needed for sabo dams, at present dam installation progress has fallen behind.

Since the adoption of high-capacity open-type steel dams for trapping debris flows can rapidly achieve an improved deployment percentage and ensure safe and secure living in light of the aforementioned situation, the demand for open-type steel dams has grown substantially. However, despite the substantial demand for such dams at sites of debris flows comprising mostly of small boulders (grain diameter sizes of 500 mm or less), they have not been used because of problems with debris flow trapping and construction.

To resolve the above problems, we have developed GRID NET™ note), a grid-type dam for debris flows of small boulders, which is a traditional grid-type dam with a fine and high-strength mesh of rings attached on the upstream side for trapping such debris[1]. We have successfully received orders for and completed the construction of four GRID NETs since its development. This paper describes the basic structure of GRID NET, experiments on the efficacy of the mesh of rings for trapping debris flows, drop experiments for boulder impact testing[3], and on-site construction.

1. Basic structure of GRID NET

Fig. 1 depicts the basic structure of GRID NET. In the basic structure, the net spacing between the vertical steel pipe members of the portion furthest upstream is fixed at approximately 600 mm, to which a mesh of 300 mm diameter rings[4] is attached. The mesh of rings is a weave of multiple 300 mm diameter rings ("small-diameter rings"), with each ring having multiple circular windings fabricated from a 3 mm diameter steel wire and held together by clips. The mesh of rings is then secured by

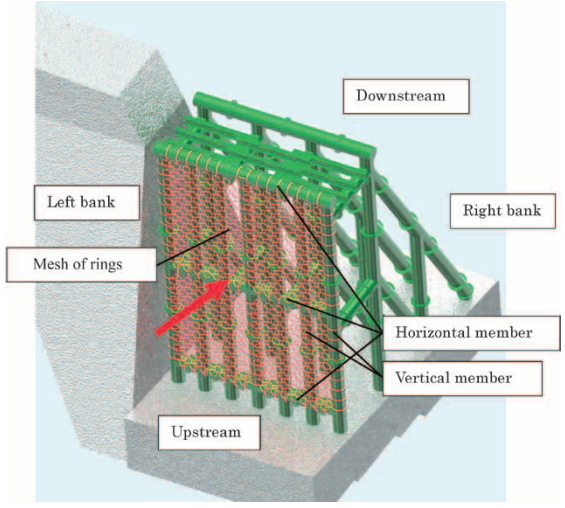

Fig. 1 Basic structure of GRID NET

note) GRID NET is a registered trademark (Nos. 5679434 and 5428784) of Kobe Steel.

shackling the small-diameter rings of the mesh to 550 mm diameter rings ("large-diameter rings") that are mounted to the vertical and horizontal members of the grid-type dam. The advantages of the basic structure are described below.

(1) The standard[2] calls for arranging the vertical and horizontal members at the most upstream part of an open-type steel dam as a planar mesh and further calls for net spacing between each of the vertical members and each of the horizontal members to be no more than the maximum grain diameter, d_{95}[1] (d_{95} is the 95th percentile grain diameter size on the cumulative particle size distribution compiled from over 200 grain samples from the site). If the grid members are arranged as above, the projected area A_0 of the opening framed by the vertical and horizontal members will become smaller than the projected area A_b of the grid members themselves when d_{95} is less than 500 mm. If, as in this case, the void ratio [$n_0 = A_0 / (A_0 + A_b)$] is 0.5 or less, the stream will become dammed[5] on the upstream side of the dam before the debris flow front reaches the barrier, causing the clump of boulders at the debris flow front to disintegrate and the boulders to arrive separately to the barrier. The debris flow is not effectively trapped.

However, since the thin wires of the mesh of rings can achieve a void ratio of 0.5 or greater, the stream does not become dammed and the debris flow can be reliably trapped.

(2) Next, the planar grid-type arrangement for the members furthest upstream was abandoned and replaced with an arrangement of only the vertical members with a net spacing of approximately 600 mm. The decision to do so was based on the rationale that a void ratio of 0.5 or greater can be achieved while also ensuring that a disaster can be suppressed with a narrow 600 mm spacing of members even if, in a rare case, the net fails due to some unanticipated event and the trapped sediment gets released.

2. Experiment to verify the trapping function of the mesh of rings

2.1 Overview of experiment

Table 1 summarizes the series of experiments that were performed. In cases 1-1 to 3-2 in Table 1 (Net model), the maximum grain diameter d_{95} was multiplied by factors of 3.0, 2.0, and 1.5 to provide a varying ring diameter Dr to investigate the effect of the ratio Dr/d_{95} on the debris flow trapping ratio, and in cases 4-1 to 6-2 (bottom beam model), the maximum grain diameter d_{95} was multiplied by factors of 2.0, 1.5, and 1.0 to provide a varying vertical height for the net spacing of the bottom horizontal beam members bh to investigate the effect of the ratio bh/d_{95} on the trapping ratio. Further, in cases 7-1 and 7-2 (Slit model), the net spacing between vertical members b1 was configured to be 1.5 times that of d_{95} in the test unit, without an installation of the mesh, to compare the trapping effectiveness with that of the mesh of rings.

The experiment was scaled to 1:50 and used a rectangular channel that was 300 mm wide and 10 m long with a gradient of 17 degrees. Sediment was packed into a thickness of 10 mm and a length of 1.3 m at a position 5 m upstream of the test unit and was released with a unit flow rate of 0.75 cm^2/s for the experiment. **Fig. 2** shows the particle size distribution of the fluidized sediment. Fig. 2 plots both the experimental sand (d_{95} = 10.1 mm) and the large boulders ($d_{95\,5}$ = 15.7 mm). The experimental sand is defined to be of grain size of the 95th cumulative percentile of all the sand used in the experiment, and the large boulders are defined to be the grain size of the 95th cumulative percentile of 100 large boulders selected from the experimental

Table 1 Summary of experiments

Case	Model name	Dr/d_{95}	bh/d_{95}	bl/d_{95}
1−1	Net model	3.0	—	—
1−2				
2−1		2.0	—	—
2−2				
3−1		1.5	—	—
3−2				
4−1	bottom beam model	1.5	2.0	—
4−2				
5−1			1.5	—
5−2				
6−1			1.0	—
6−2				
7−1	Slit model			1.5
7−2				

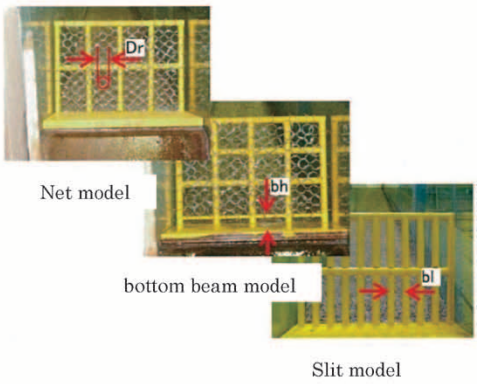

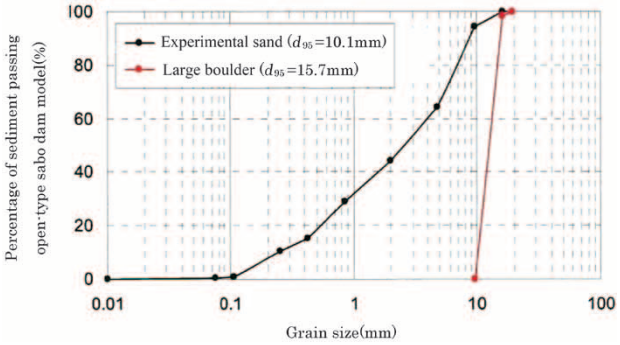

Fig. 2 Grain size distribution of fluidized sediment

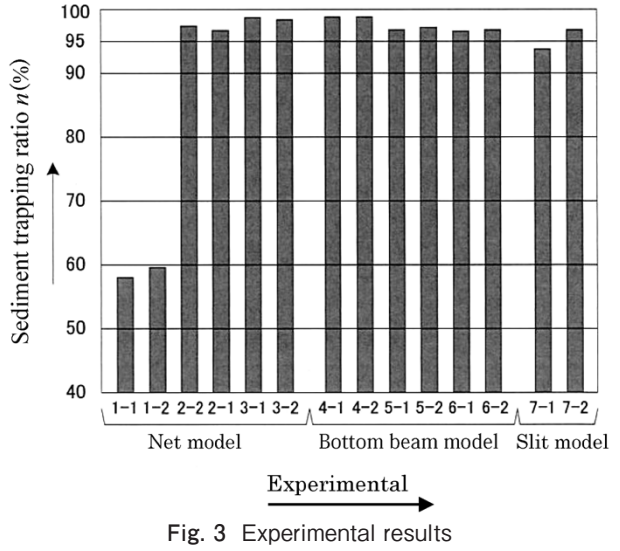

Fig. 3 Experimental results

sand. In this experiment, the latter grain size of 15.7 mm was used as the maximum grain size, or d_{95}.

2.2 Experimental results

The experimental results are shown in **Fig. 3**. The horizontal axis labels in Fig. 3 are the cases of the experiment and the vertical axis is the debris flow trapping ratio *n*. Here, the trapping ratio n, is calculated as: $n = V1 / (V2 - V3) \times 100$, where $V1$ is the volume of sediment, $V2$ is the volume of all fluidized sediment, and $V3$ is the volume of sediment that overflowed the test unit. Fig. 3 offers the following observations.

(1) Net model

1) The trapping ratio *n* for cases 1-1 and 1-2 is 60% or less and is lower in comparison with the other cases. This was due to the large value for *Dr*, which in this case was 3 times the size of d_{95} (Dr/d_{95} = 3.0), which caused the sediment that had initially been trapped to leak through as it was pushed by the flow behind it.
2) For cases 2-2 to 3-2, the ratio *n* is 95% or greater and the design adequately served its purpose for trapping debris. This means that if *Dr* is configured to be no more than 2 times the value of d_{95}, the debris flow can be adequately trapped. However, in conformance to the standard[1] for the actual implementation, we have defined *Dr* to be no more than 1 times the value of d_{95} in order to trap more reliably. **Fig. 4** shows pictures of the trapped debris flow.

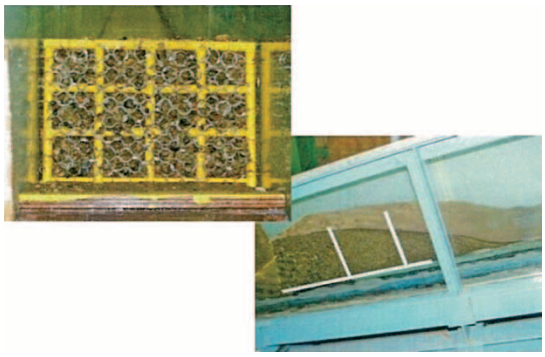

Fig. 4 Trapped debris flow (Case 4-1)

(2) Bottom beam model

1) The trapping ratio *n* for all the bottom beam model cases was high at 95% or greater. This shows that if *bh* is no more than two times the value of d_{95}, the debris flow can be adequately trapped.
2) Since the debris flow depth *h* in the experiment was 40 mm and was larger than *bh* (10 mm, 15 mm, 20 mm) of the bottom beam model, this means that even if *bh* is larger than d_{95}, the debris flow can be adequately trapped as long as *bh* is smaller than *h*. However, in consideration of safety and the standard[1] in the case of *bh* as well, we have defined *bh* to be no more than the debris flow depth *h* or to be no more than 1.5 times the value of d_{95}.

(3) Slit model

At the 95% level, the slit model has a high trapping ratio *n*. A comparison of the slit model *n* values with the *n* values for the net model cases 2-2 to 3-2 shows that the net model *n* has higher values. This means that the trapping efficacy of the mesh of rings is considerably high.

(4) Stream damming

In this series of experiments, the stream never became dammed and we were able to verify that the clump of boulders at the debris flow front reached the model without disintegrating.

3. Experiment to validate the energy-absorbing power of the mesh of rings

Although the mesh of rings is an implementation of a proven wire mesh technique[6] for trapping debris flows, the method to test the energy absorption, *ER*, was not known for a mesh of rings covering a narrow rectangular cross-section framed

by vertical and horizontal steel pipe members as implemented in this study. Therefore we assumed that *ER* can be expressed as a product of the energy absorbency *En* retained by one ring (as used in rockfall protection works) and the number of rings that covers the rectangular cross section noted above, as shown in Eq. (1). To verify this assumption, we performed full-sized impact tests.

$$ER = En \times nR \quad \cdots\cdots (1)$$

where:

En is the energy absorbency of one ring.
nR is the number of rings.

3.1 Overview of experiment

Table 2 summarizes the series of experiments that were performed and their results. **Fig. 5** illustrates the test unit and test equipment. As shown in Table 2, two stands were used in the experiment. For stand I, the center-to-center spacing of the horizontal members is 1,800 mm and is hypothetically based on the lowest dam height; and stand II is hypothetically based on the highest possible height for a dam and has spacing of 4,150 mm between the horizontal members.

Nr in Table 2 is the number of windings per ring. Cases 1-1 to 4-2 in Table 2 used rings with an *Nr* of 5, with which we investigated the maximum energy absorbency of the mesh of rings. Similarly, cases 5-1 to 6-2 used rings with an *Nr* of 7 and cases 7-1 and 7-2 used rings with an *Nr* of 1. Cases 8-1 and 8-2 used stand II, which has the narrowest rectangular cross section, and rings with an *Nr* of 5.

The test unit was full-sized while GRID NET, as shown in Fig. 5, was partially simulated with a mesh of rings attached to a stand constructed from 508 mm diameter steel pipes. The mesh was installed according to the actual installation method in which the mesh is secured to every other vertical member. Note that *nR* from Eq. (1) is the number of rings

Table 2 Summary of experiments and experimental results

Case	Stand	*Nr* (windings)	*En*(KJ)	*nR* (number of rings)	ER(KJ)	EW(KJ)	EW/ER	Results
1−1	I	5	0.34	12.5	4.25	4.25	1.00	Pass
1−2								Pass
2−1						5.31	1.25	Pass
2−2								Pass
3−1						6.38	1.50	Fail
3−2								Pass
4−1						8.50	2.00	Fail
4−2								Fail
5−1		7	0.50		6.25	6.25	1.00	Pass
5−2								Pass
6−1						7.81	1.25	Pass
6−2								Pass
7−1		12	1.10		13.75	13.75	1.00	Pass
7−2								Pass
8−1	II	5	0.34	33.5	11.39	11.39	1.00	Pass
8−2								Pass

Nr(windings) : Number of windings per ring *En*(KJ) : Energy absorbency per ring
nR : Number of rings in rectangular section framed by vertical and horizontal members
ER(KJ) : Calculated energy absorbency of mesh of rings
EW(KJ) : Test weight energy
Pass : No mesh failure Fail : Mesh failure

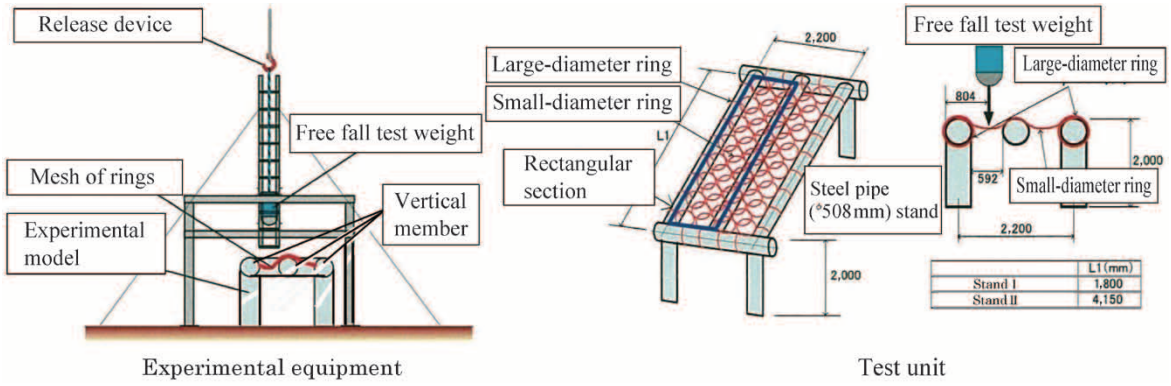

Fig. 5 Experimental equipment and test unit

inside the rectangular cross section indicated in Fig. 5.

As shown in Fig. 5, the experiment was conducted using a test weight to simulate a stone in a free fall drop from a designated height to impact on one side of the mesh.

3.2 Experimental results

The experimental results are as shown in Table 2. **Fig. 6** also shows the condition of the mesh before and after impact by the test weight for case 1-1.

(1) As can be seen from Table 2, the mesh failed in the group of cases from 3-1 to 4-2, but failure was not observed in cases 1-1 to 2-2. *EW* in Table 2 is the potential energy of the test weight that was varied for the testing. The results thus indicate that the mesh of rings with an *Nr* of 5 windings has an energy absorbency that is 1.25 times that of *ER* or more. Further, Fig. 6 shows that the mesh of rings had stretched quite a bit, clearly indicating that energy had been absorbed by its deformation.

(2) We can see from cases 5-1 to 7-2 that a value of 1.0 or greater was achieved for the ratio *EW*/*ER* for the mesh.
These results mean that the mesh possesses the predetermined energy absorbency for *Nr*s of 7 and 12 windings as well.

(3) We can see from cases 8-1 and 8-2 that the mesh achieved a value of 1.0 or greater for the ratio *EW*/*ER*. These results mean that the mesh possesses the predetermined energy absorbency for stand II as well.

(4) Since the energy absorbency *ER* of the mesh of rings was less than *EW* as observed in the discussions (1) through (3) above, we have been able to confirm the appropriateness of using *ER* from Eq. (1) for our designs.

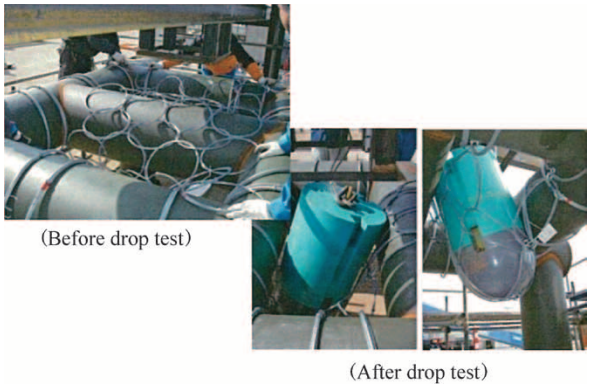

Fig. 6 Condition of mesh of rings

4. Construction of GRID NET

4.1 Preliminary considerations for construction

The actual installation of the mesh of rings to a grid-type dam is performed after the grid-type dam has been constructed and painted, and requires the use of the construction scaffolding and care to avoid damaging the paint during mesh installation. As a study prior to an actual installation, a mock install (or rehearsal) was performed with the conditions stated above. An overview of the study is given below.

(1) The large-diameter rings are multiple windings fabricated from 5 mm diameter wire. We verified that each ring could be easily mounted by unwinding the ends of the wire so as to loosen the strands of the winding and slipping it onto the steel pipe, then turning the rings repeatedly to complete the mounting.

(2) To prevent damage to the paint while the large-diameter rings are mounted, we decided to cover the steel pipes with vinyl tarpaulin. Note that the vinyl tarpaulins are to be removed after installation has been completed.

(3) After the large-diameter rings have been mounted, the ring windings are secured with clips so that the windings do not fray. However, because the clips might have damaged the paint on the steel pipes after the vinyl tarpaulins were removed, the step was taken to cover all the clips with vinyl sleeves.

(4) Scaffolding has traditionally been installed in very close proximity to the vertical members during the construction of a grid-type dam, so there was no space for attaching the mesh of rings. For this reason, the provision was made for a gap of several centimeters, small enough so as not to be a safety issue, between the vertical members and the scaffolding.

(5) **Fig. 7** is a picture of the installation experiment for the mesh of rings. Note that because the mesh of rings is a woven assembly of flexible, 300 mm diameter, small-ringed structures, it has high vertical and horizontal elasticity. For this reason, there was a possibility that an error might occur between the final dimensions of the actual item and the final design dimensions. The concern was that if the error were significant, the attached mesh of rings would sag more than expected or would be too taut, so we also verified the mesh tension during the mock install. As a result, we were able to verify that the mesh of rings did not have unexpected sag or tautness and that it can be installed without problems.

4.2 Construction of GRID NET

GRID NET was selected for installation at: the Shokanbogawa sabo dam site for the Tannan Civil Engineering Office of Fukui Prefecture in fiscal year 2011; the Higashinikkawa sabo dam site for the Hokushin Construction Office of Nagano Prefecture in fiscal year 2012; the Obama sabo dam site for the Junreidani sabo dam site for the Obama Civil Engineering Office of Fukui Prefecture in fiscal year 2013; and the Hinoki-no-Hazakawa sabo dam site for the Central Prefectural Land Development Office of Shimane Prefecture in fiscal year 2014.

Fig. 8 is a diagram of the attachment procedures for the mesh of rings at the Shokanbo sabo dam. Below is a description of the installation based on Fig. 8.

1) After the dam has been constructed, the scaffolding already in place is used to wrap the vertical and horizontal members with vinyl tarpaulin to protect the painted surfaces of the steel pipes.
2) The large-diameter rings are mounted on the vertical and horizontal members.
3) Vinyl sleeves are installed over the clips that secure the large-diameter rings.
4 A crane hooks onto the second row of small-diameter rings on the mesh of rings to raise and suspend the mesh. The top row of small rings is kept free since these need to be shackled to the top row of large-diameter rings.
5) First, the top row of small-diameter rings are manually pulled into their designated positions and shackled to the large-diameter rings. Then the small-diameter rings are shackled to the large-diameter rings on the vertical members and in turn to the large-diameter rings on the bottom row. This work was performed manually and relatively easily.
6) After the mesh of rings has been attached, the quality of the installation is checked, and overall work adjustments are made.
7) Lastly, the vinyl tarpaulins are removed.

We were able to complete the series of tasks in approximately one and a half days without major problems. This was possible because we had thoroughly conducted a preliminary study of the installation. **Fig. 9** is a picture of the mesh of rings

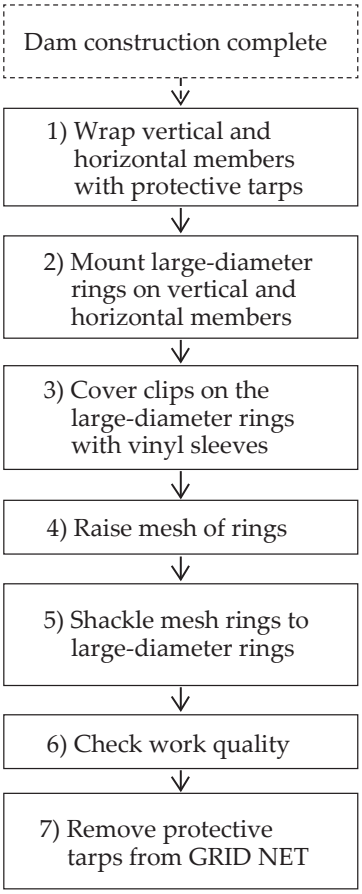

Fig. 8 Installation procedure for the mesh of rings

Fig. 7 Attachment of the mesh of rings

Fig. 9 A completed GRID NET

after installation. In Fig. 9, we can see that the mesh has been installed without excessive sag.

Conclusions

We have developed and achieved commercial viability with GRID NET (Grid-type Sabo Dam for Debris Flows of Small Boulders), a dam capable of handling debris flows containing small boulders, which have been beyond the application scope of open-type steel dams. We believe the achievement of such an expansion in the application scope of open-type steel dams with extremely large debris flow trapping capacities will have a significant impact on improving the deployment percentage of sabo dams. Furthermore, as a dam for mitigating disasters, GRID NET is also capable of handling fine particle grains when such grains must be prevented from flowing downstream. GRID NET is expected to protect lives and assets from sediment disasters and to enhance the safety and security of residents.

Going forward, we will maintain a sustained effort to perform follow-up investigations of the existing GRID NET installations and to keep verifying their functional efficacies for letting sediment pass through during low and medium flows but to trap debris during large flows, and to keep verifying the durability of the mesh of rings after a debris flow has been trapped.

References

1) H. Moriyama et. al. *Journal of the Japan Society of Erosion Control Engineering*. 2010, Vol.62, No.6, p.30-33.
2) Ministry of Land, Infrastructure, Transport and Tourism. *Manual of Technical Standard for establishing Sabo master plan for debris flow and driftwood*. 2007.
3) T. Kawamura et. al. *Fiscal Year 2010 Proceedings of the Annual Conference of the Japan Society of Erosion Control Engineering*. 2010, p.210-211.
4) TOA Grout Kogyo (Sabo Engineering) *Report*. 2002,

(Received 31 July 2009; Accepted 26 January 2010).

5) Y. Hasegawa et. al. *Journal of the Japan Society of Erosion Control Engineering*. 2003, Vol.55, No.6, p.66-73.
6) K. Shimojo et. al. *Journal of the Japan Society of Erosion Control Engineering*. 2010, Vol.62, No.6, p.38-42.

Development and Practical Application of a Sound Absorbing Panel Using Microperforated Aluminum for Shinkansen Tunnel Entrance Hoods

Ph.D. Takashi HORIUCHI *1, Kei OGINO *1, Toshio YOSHIMURA*1, Ichiro YAMAGIWA*2, Yuichi TORIGOE *3

*1 Steel Structures & Sabo Division, Engineering Business
*2 Mechanical Engineering Research Laboratory, Technical Group
*3 CAE & Evaluation Dept., Engineering Mechanics Div., Kobelco Research Institute, Inc.

A sound absorbing panel for Shinkansen tunnel entrance hoods has been developed using a sound absorbing material featuring microperforated aluminum. The conventional microperforated aluminum material was enhanced in terms of structural strength for use in Shinkansen tunnel entrance hoods. The developed microperforated panel was designed using finite element analysis, and was subjected to strength tests, which demonstrated the high safety standards of the product. It can be applied to the ceiling of entrance hoods installed at tunnel portals of Shinkansen tracks, where it has been shown to dampen noise dramatically.

Introduction

Reducing environmental noise is a great concern in society, in connection with the development of traffic infrastructure and the need for creating comfortable living environments. For more than two decades, we have developed various noise insulation technologies and products for many applications including Shinkansen bullet train systems and expressways. Our microperforated aluminum sound absorbing panel is one of our unique products in this field. This panel had found use in noise barriers for roads and conventional railroad lines, but never before in sound absorbing panels for Shinkansen lines.

On the other hand, installing sound absorbing materials on tunnel entrance hoods is one of the major measures against environmental noise around Shinkansen tracks. It is possible to achieve a tangible noise reduction around the tunnel portal by applying sound absorbing material to the entire inner arch of the entrance hood. Compared with similar materials used in open sections, sound absorbing material installed in tunnel entrance hoods are subjected to punishing conditions. A particularly safe structure is also required to eliminate the risk of such material being fragmented and falling off from the ceiling of the tunnel entrance hood.

The microperforated aluminum panel would be a suitable solution to meet the above requirements. However, the conventional product for noise barriers is structurally insufficient in both terms of strength and acoustic performance. This is why we have used the microperforated aluminum panel to develop a new sound absorbing panel with a high-strength structure for Shinkansen tunnel entrance hoods. The new product is the first microperforated aluminum panel to be selected as a noise control material for Shinkansen trains. It can be used on the inner walls, including the ceiling, of Shinkansen tunnel entrance hoods for a substantial noise reduction. This paper describes the development and practical application of the new panel and presents a real-life installation of the technology.

1. Sound absorbing technology using microperforated aluminum

1.1 Structure and sound absorbing principles of the microperforated aluminum panel [1)]

Unlike fiber-based porous sound absorbing materials such as glass wool, microperforated aluminum panels consist of microperforated aluminum plates and air space only. In other words, they are comprised of metallic materials alone.

The panel technology exploits the basic principles of Helmholz resonance, in this case the acoustic resonance generated in perforations in the aluminum materials and air space behind them. It absorbs sounds by exploiting two phenomena:

1) Sound energy from noise and other sources is converted into frictional energy in perforations; and
2) Eddies generated by the reciprocal movement of air in perforations cause pressure losses.

Compared with conventional sound absorbing systems using acoustic resonance in perforated plates, this technology features very small perforations (1.5 mm or less in diameter), which increase friction damping in the holes, enabling the panel to absorb sounds over a broad range of frequencies.

Fig. 1 shows an example of microperforated aluminum panel structure. The multilayer structure is comprised of, in the order from the outermost facing the sound source, a surface microperforated aluminum plate, air space, inner microperforated aluminum foil, air space, and a noise insulation back

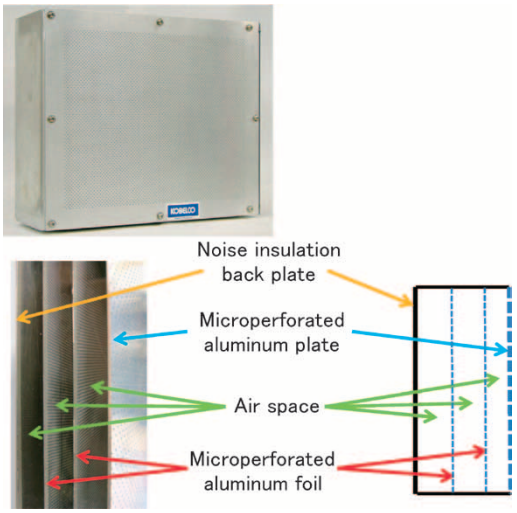

Fig. 1 Example of microperforated aluminum panel structure

plate. The multilayer structure of microperforated components gives the acoustic resonator multiple degrees of freedom, increasing the number of resonant frequencies and thereby ensuring a broader range of sound absorption.

1.2 Technical features

General features of a microperforated aluminum panel include:

1) Acoustic performance: sound absorption efficiency can be designed using parameters including the thickness, perforation diameter, and aperture ratio of the microperforated aluminum plate and foil as well as the thickness of the air space behind.
2) Strength properties: the panel features stable strength with no risk of components being fragmented and falling off.
3) Corrosion and weather resistance: it is suitable for prolonged outdoor use.
4) Burning quality: the panel is flame resistant.
5) Environmental compatibility: panel materials are recyclable without generating industrial waste.

In particular, the advantages, shown in items 2 to 5 above, over conventional fiber-based porous materials, which come from the fact that the entire panel comprises metallic materials alone, make the panel suitable for use in many different environments. It had therefore been developed and used in noise barriers for roads and existing railroad lines [2], but never before for Shinkansen tracks.

2. Development of a sound absorbing panel for use in Shinkansen systems

The above-mentioned features of the microperforated aluminum sound absorbing panel make it ideal for noise control near tunnel portals of Shinkansen systems. The panel's acoustic performance and strength properties, in particular, meet the relevant noise control requirements. These requirements and the details of the development project are presented in this chapter.

2.1 Noise near tunnel portals

While running on the track, Shinkansen trains generate various noise. To reduce the noise transmitted to surrounding areas, noise control measures for open rail sections (e.g., sections of elevated tracks), where direct transmissions from the train prevail, focus on noise barriers and others that address noise transmission paths. By contrast, measures implemented at tunnel portals must include more than direct noise control. The reason is that noise generated by the train passing through the tunnel reverberates in the tunnel and is emitted from the portal, which is combined with direct noise from the adjacent open section (**Fig. 2**). This is why it can be impossible to reduce overall noise near the tunnel portal by simply increasing the height of the noise barriers [3].

A similar phenomenon can be observed with a tunnel entrance hood (**Fig. 3**) installed to reduce tunnel booms generated as Shinkansen trains enter the tunnel. When tunnel portal emissions represent a large portion of near-portal noise, it is necessary to implement measures to reduce such emissions. A previous study [4] conducted using a model considers the possibility of reducing portal noise emissions by applying sound absorbing material to the entire inner arch of the entrance hood. The study shows that the soundproofing of these surfaces is particularly effective where the inner walls, e.g. ceiling, of the entrance hood can be seen through from the surrounding area.

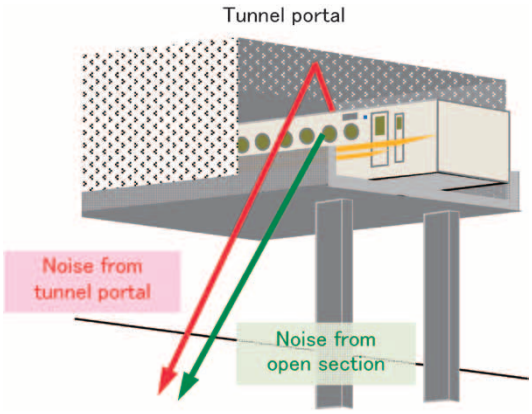

Fig. 2 Noise at points near tunnel portal

Fig. 3 Tunnel entrance hood for Shinkansen

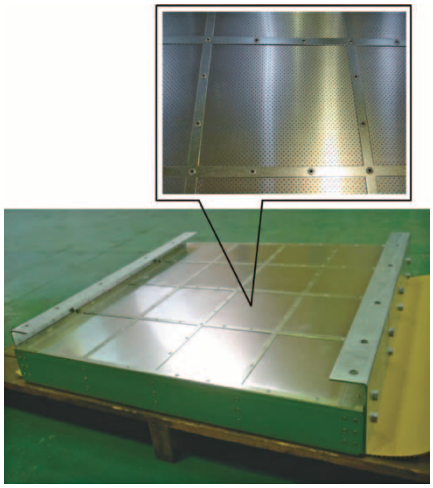

Fig. 4 Microperforated panel for tunnel entrance hoods

To fulfill these noise control requirements, We used our microperforated aluminum sound absorbing technology to start developing a new sound absorbing panel for tunnel entrance hoods. The development processes and results of implementation are described in the following.

2.2 High-strength sound absorbing panel

2.2.1 Overview of new development

Fig. 4 shows the sound absorbing panel product for tunnel entrance hoods that has been developed in the project under review. The panel measures 990 mm in height and 969 mm in width (including fixtures), with a thickness of 100 mm (150 mm including fixtures). Component sheets other than microperforated aluminum plates are made of highly weatherable plated steel sheet, while fixtures are made of hot-dip galvanized steel. The weight of a single panel including the fixtures is as low as approximately 50 kg for easy handling during installation. To reflect the results of the strength design and endurance tests described below, the surfaces and inside areas of the sound absorbing panel are reinforced using steel members.

Fig. 5 shows general drawings of the new sound absorbing panel. During installation on a tunnel entrance hood, panels can be fed into installation beams (made of H-section steel) preinstalled in the main structure of the entrance hood and bolted onto the inner walls using locking nuts to ensure safety.

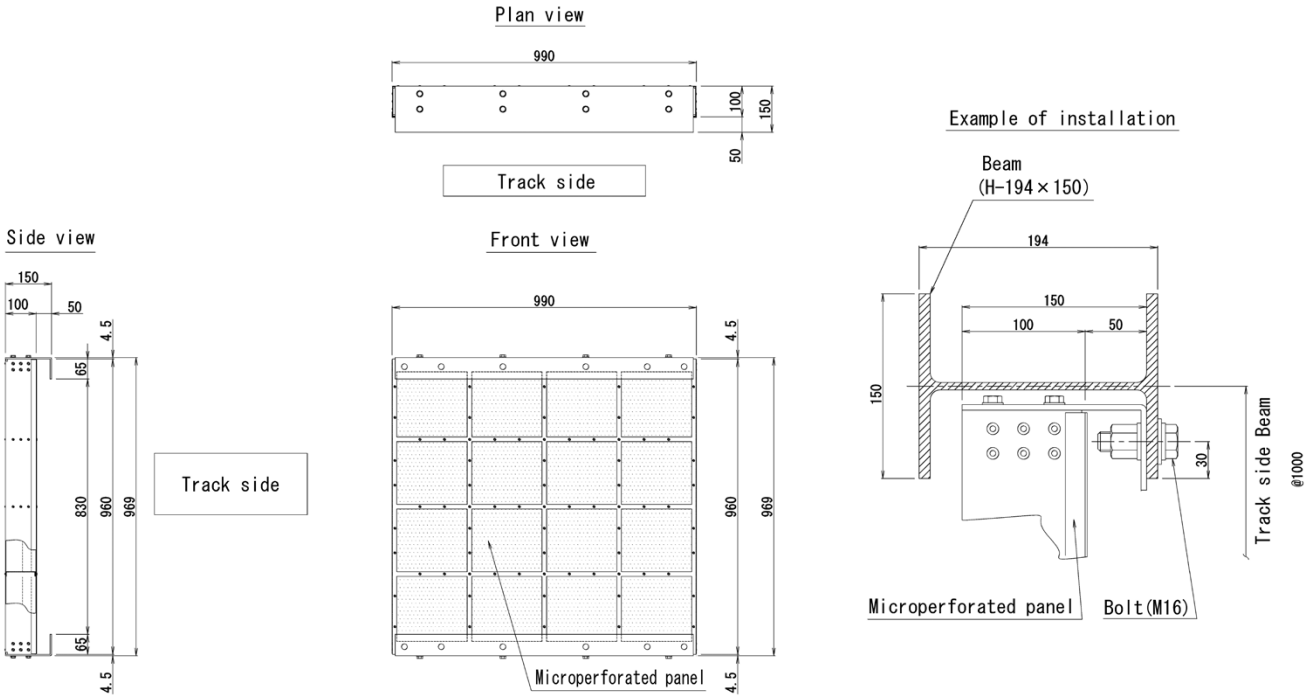

Fig. 5 General drawings of microperforated panel for tunnel entrance hoods

2.2.2 Development objectives

The development of the microperforated panel for inner walls of tunnel entrance hoods had three objectives to be achieved.

1) Design load: The panel must withstand a wind pressure of ±4.2 kPa in emergencies and ±2.1 kPa constantly.
2) Fatigue resistance: The panel must withstand three million repeated applications of a constant load of ±2.1 kPa.
3) Safety: The entire panel, including its fixtures and sound absorbing material, must consist solely of metallic materials to reduce the risk of the panel or broken pieces falling off.

By way of comparison, a design load of 3 kPa is specified for noise barriers installed on the side walls in open sections of Shinkansen tracks. One possible reason is that, unlike the partially closed space in tunnel entrance hoods, open sections are subjected to lower wind pressures. Another reason is that, located on the side walls of the track, such noise barriers are relatively easy to inspect and replace during maintenance work.

Compared with such noise barriers, the newly developed sound absorbing panel is more difficult to maintain, due to it being installed on the inner walls (including the ceiling) of Shinkansen tunnel entrance hoods, which cover part of the track entirely. It should also be noted that Shinkansen operators attach particular importance to safety. This is why we chose to employ microperforated aluminum sound absorbing panel technology; its stable strength and resistance to ageing were expected to help ensure safety. But again, the structure of the basic product, designed for roads and existing railroad systems, is insufficient in terms of strength and fatigue resistance. It was therefore necessary to design a more durable product and verify its suitability for the application in question.

2.2.3 Strength design

During the strength design of the new sound absorbing panel, the finite element method (FEM) was employed to analyze individual components in detail. In stress evaluation, we compared the stress values found in the analysis to be acting on members with allowable levels. Stress levels for microperforated plates and blind rivet joints were increased threefold for evaluation, by taking stress concentrations around the holes into account. **Fig. 6** shows the result of the FEM analysis.

The panel was analyzed on the assumption that the design loads for anomalies and normal situations

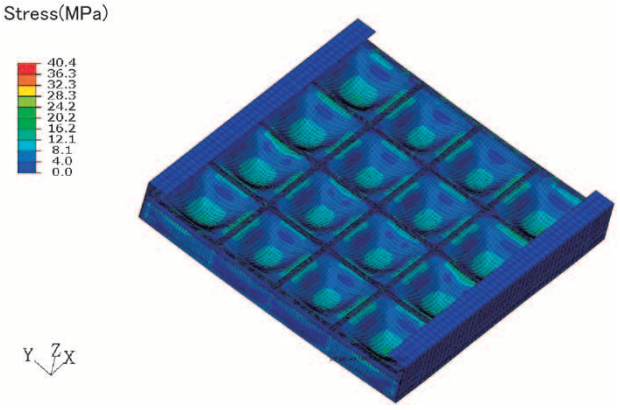

Fig. 6 Stress contours created by FEM analysis

shown in the previous section were applied to the panel's front and back surfaces. It was thus established that the stress acting on each member was not greater than the corresponding allowable level. It was also thus confirmed that, during the repeated applications of the load, the stress acting on each member did not surpass the corresponding fatigue limit. The above strength design phase of establishing the safety of the sound absorbing panel and its components was followed by endurance tests on real panels. These double testing procedures are designed for further verification of safety.

2.2.4 Endurance tests

1) Static load test

The microperforated panel was tested using sandbag weights to verify its safety against static loads. To accurately reproduce the panel structure as installed, test panel fixture samples included an installation beam and securing bolts. The front and back surfaces were each loaded with weights generating a pressure of 6 kPa, surpassing the design load for anomalies (4.2 kPa) and approximately 1.4 times the design load. **Fig. 7** shows the test of panel being subjected to the static load.

The test revealed that the panel was safe against the design load, causing no problems such as damage to or excessive deformation of any component.

2) Load fatigue test

A fatigue resistance test was required to verify the panel's safety against repeated load applications. It is practically impossible, however, to apply a pressure load repeatedly to the panel. As an alternative method, a panel loaded with weights was tested on a vibration test bench. Using a 150 kg sandbag, the weight was designed to generate a load equivalent to 3 kPa under an acceleration of 1 G. This load was applied to each of the panel's front and

Fig. 7 Static load test of microperforated panel

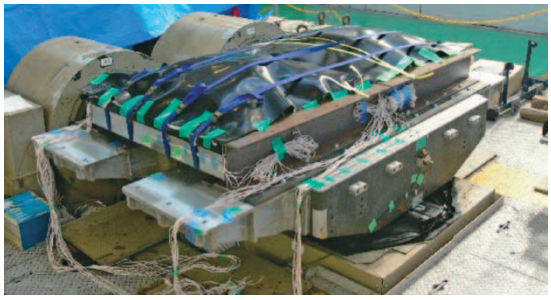

Fig. 8 Load fatigue test of microperforated panel

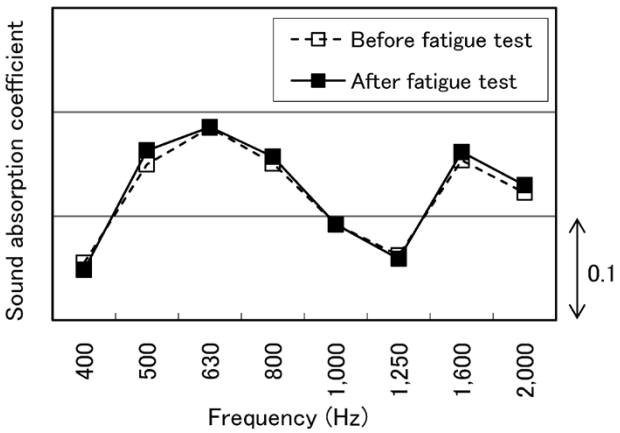

Fig. 9 Sound absorption coefficient after load fatigue test

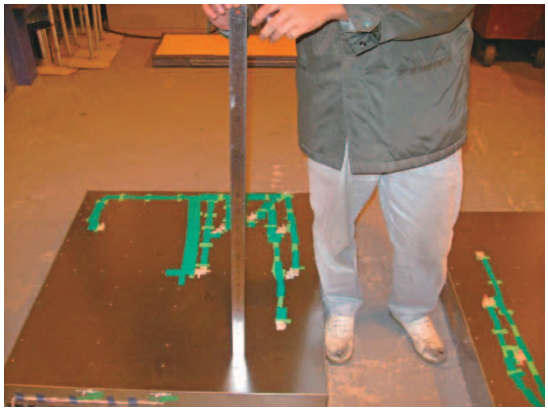

Fig.10 Impact test of microperforated panel

back surfaces three million times with a vibration frequency of 5 Hz. **Fig. 8** shows the panel during the load fatigue test.

The load fatigue test established that the panel was safe against the repeated load, causing no problems such as damage to or loosening of any component. In addition, the sound absorption performance of the microperforated panel was measured before and after the load fatigue test. **Fig. 9** shows the panel's sound absorption coefficient at normal incidence measured before and after the load fatigue test. It reveals that three million cycles of vibration causes no change in sound absorption coefficient.

Generally, the most vulnerable in structure are joints in surface microperforated aluminum plates fastened using blind rivets. The most punishing load conditions are generated by negative pressures from the inside of the microperforated panel to the track side. A similar trend was also observed during the FEM analysis described in the previous section. With a focus on the above-mentioned joints, a further load fatigue test was conducted under negative pressure load conditions. With a weight placed inside, the microperforated panel was vibrated three million times with a frequency of 5 Hz to apply a load generating a pressure of 2.1 kPa to the surface microperforated aluminum plate. Like the previous one, the second test shows no problems caused in the microperforated panel.

3) Impact test

Impact of foreign objects on the microperforated panel could cause components to be fragmented and fall off from the panel. An impact test was performed to verify safety in this regard. Specifically, an iron ball weighing 1 kg was dropped from a height of 1 m to hit several points on the front and back surfaces of the microperforated panel. **Fig.10** shows the panel during the impact test.

The impact test showed that the collisions only caused indentations in the impact surfaces, with no components broken and no fragments dropped off. Consisting entirely of metallic materials, down to the sound absorbing elements, the product can effectively prevent the components from being fragmented and falling off.

2.3 Acoustic performance

The "sound absorption coefficient in a reverberation room" (JIS A 1409, hereinafter simply "sound absorption coefficient") of the microperforated panel was measured using a real

product. **Fig.11** shows the results. The panel's sound absorption coefficient reaches its peak around 800 Hz and remains 0.7 and above between 250 Hz and 4 kHz. This superb feature has been made possible by the panel's excellent acoustic design, which adapts sound absorbing performance to the frequency characteristics of Shinkansen noise sources. Using the real product, the test established that the microperforated panel has high sound absorption coefficients over a wide frequency range.

3. Application to a tunnel entrance hood

3.1 Installation in a real tunnel

The results of development described in the preceding chapter have made the microperforated panel technology the first of its kind to be used for noise control in a Shinkansen system. This section presents the real-life installation of the microperforated panel technology in a tunnel entrance hood [5), 6)].

3.1.1 Installation method

The tunnel entrance hood is 10 m in length and made of steel. Microperforated panels were installed over almost the entire length of the inner walls, including the ceiling, of the hood. **Fig.12** shows a view of microperforated panels being installed on the entrance hood, while **Fig.13** shows a view of the hood following panel installation.

The following is a brief description of the method employed to install the microperforated panels. First, set up a scaffold directly under the ceiling area where microperforated panels are to be installed. The reason is that the ceiling is as high as 8.5 m above the ground. A chain block is made available on top of the scaffold to hoist the materials. Use a crane to move the materials from outside the track close to the tunnel portal. Carry them further to the scaffold manually. Hoist the materials onto the top of the scaffold and install them as described above. Check the securing bolts for tightening torque and remove the scaffold. These steps are to be completed in a predefined nighttime period of a few hours during which no trains operate around the tunnel. The scaffold is installed and removed for each round of work. Working under these unusual operating conditions required great attention to safety. It took a few months to complete the installation work.

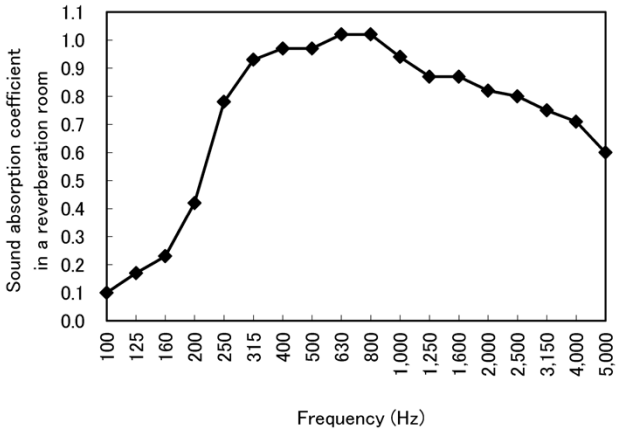

Fig.11 Sound absorption coefficient in a reverberation room

Fig.12 Installation of microperforated panels

Fig.13 Microperforated panels covering inner walls of tunnel entrance hood

3.1.2 Effects of microperforated panels

In parallel with the installation of microperforated panels, environmental noise levels were measured to see the effects of their installation. The work was executed to extend the sound absorbing installation step-by-step, starting from the tunnel side to the front edge of the entrance hood. The aim was to determine the relationship between an increase in sound absorbing installation length and the corresponding noise decrement.

During each test cycle, noise emissions from a total of 20 trains running in both directions were

measured both before and after the increase in installation length. In ether phase, the ten highest values from among the maximum noise levels (Slow) measured from the 20 trains were power-averaged. The noise decrement was defined as the difference between both power average values. The above procedures were performed for several measuring points to see the distribution of amounts of noise reduction over a surface.

The above test showed that noise decrement tended to increase as the installation work progressed. Noise decrements varied depending on the measuring point locations. Points from which the inside of the entrance hood can be seen through registered greater noise decrements than the other points to which the above condition does not apply. A likely reason is that, at the see-through measuring points, tunnel portal noise emissions previously represented a large portion of near-portal noise. The increase in sound absorbing installation length therefore had a greater impact on noise levels. The completion of the entire design installation length led to a total noise decrement of up to approximately 4 dB, depending on the measuring point. By installing sound absorbing panels on the inner walls, including the ceiling, of the tunnel entrance hood, we have successfully achieved substantial reductions in near-portal noise levels.

3.2 Future developments

By installing sound absorbing panels on the inner walls, including the ceiling, of the tunnel entrance hoods described in the previous section, we have successfully achieved substantial reductions in near-portal noise levels. We believe it is necessary to improve this noise control method further for future applications. One possible way of improvement now under consideration is to implement soundproofing from outside the entrance hood [7]. The aim is to reduce installation work cost and improve safety and ease of maintenance. We are also studying possible improvements on the microperforated panel presented here. In addition, we will continue to increase the performance of technology for reducing noise emissions from tunnel portals.

Conclusions

This paper has presented the new sound absorbing technology developed using microperforated panels, which was adopted for use in a Shinkansen system for the first time. By taking advantage of the features of this noise control technology, such as acoustic performance and strength properties, we will develop more applications in traffic infrastructure including Shinkansen systems. We will build on the findings of the above development project and consider developing products that can accommodate environments which require even greater strength. We hope that this work serves environmental preservation purposes.

In developing the product, we received many useful pieces of advice from individuals from West Japan Railway Company and other organizations who were concerned with the project. We express our sincere thanks to these individuals.

References

1) I. Yamagiwa. *So-on Seigyo (Noise Control)*. 2012, Vol.36, No.6, pp.410-414.
2) T Yamada et al. *Nippon So-on Seigyo Kogakukai Kenkyuhappyokai Koenronbunshu 2007-9-12/13 (Proceedings of Meeting, the Institute of Noise Control Engineering of Japan, September 12/13, 2007)*. Nihon So-on Seigyo Kogakukai (Institute of Noise Control Engineering of Japan). 2007, pp.165-168.
3) K. Nagakura. *Tetsudo Soken Hokoku (Railway Technical Research Institute Report)*. 2013, Vol.17, No.11, pp.13-18.
4) S. Matsui et al. *Nippon So-on Seigyo Kogakukai Kenkyuhappyokai Koenronbunshu 2010-9-28/29 (Proceedings of Meeting, the Institute of Noise Control Engineering of Japan, September 28/29, 2010)*. Nippon So-on Seigyo Kogakukai (Institute of Noise Control Engineering of Japan). 2010, pp. 135-138.
5) S. Matsui et al. *Nippon So-on Seigyo Kogakukai Kenkyuhappyokai Koenronbunshu 2012-9-5/6 (Proceedings of Meeting, the Institute of Noise Control Engineering of Japan, September 5/6, 2012)*. Nippon So-on Seigyo Kogakukai (Institute of Noise Control Engineering of Japan). 2012, pp.281-284.
6) T. Nitta et al. *Doboku Gakkai Dai 67-kai Nenji Gakujutsu Koenkai Ronbunshu 2012-9-5/6/7 (Proceedings of the 67th Annual Conference of the Japan Society of Civil Engineers, September 5/6/7, 2012)*. Doboku Gakkai (Japan Society of Civil Engineers). 2012, pp.201-202.
7) K. Ikegashira et al. *Nippon Tetsudo Shisetsu Kyokaishi (Journal of the Japan Railway Civil Engineering Association)*. 2013, Vol.51, No.12, pp.929-931.

"Eco Kyuon" – Microperforated Sound Absorbing Panel

Ichiro YAMAGIWA*1, Masaji HORIO*2, Shigeharu NAKAOKA*2, Takahiro YAMADA*2

*1 Mechanical Engineering Research Laboratory, Technical Development Group
*2 Engineering Department, SHINKO KENZAI LTD.

This paper presents the development of sound absorbing panels utilizing the sound absorption mechanism of microperforated plates and foils. Microperforated plates and foils reduce acoustic energy by generating friction damping and pressure loss from the vibration of acoustically resonating aperture air. Applying this principle, we have developed a method to predictively calculate the sound absorption coefficient and applied it to develop microperforated sound absorbing panel products. A distinct advantage of this method is that these products can be designed with the optimum frequency characteristics for the desired sound absorption coefficient. These products were used to develop rail and road noise barriers that contribute to traffic noise reduction.

An additional purpose of the study was to develop a transparent sound absorbing panel solution. We selected polycarbonate, a clear polymer material, as the film material to which this technology was applied. The challenge was to overcome the drop in sound absorption due to the propensity of the transparent polymer film to intense vibrations. Improved sound absorption performance was successfully achieved by creating several combinations of manufacturable materials, calculations for predicting the sound absorption coefficient and performance verification experiments. Optimization of design elements such as sheet thickness, aperture diameter, and aperture ratio was also critical to achieving the desired performance. Since successful commercial transparent sound absorbing panels are rare, these products hold much promise for broad application in a variety of markets.

Introduction

Fibrous sound-absorbing materials are common in acoustic panels that are used for road and rail noise absorption applications. Some fibrous absorbers require weatherproofing with a lining of a thin polyvinyl fluoride (or similar material) film to prevent rainwater intrusion or dispersion of the fiber material. Such fibrous absorbers have presented weather resistance and disposal problems and have caused health-related problems stemming from the dispersion of fiber particles due to time-related degradation or damage to the liner.

To address these problems, we have developed Eco Kyuon™ note 1), a sound absorbing panel comprising a thin microperforated aluminum plate and multiple internal air spaces separated by microperforated aluminum foils. We have also developed a transparent sound absorbing panel by substituting the thin microperforated aluminum plate and foil with suitable transparent materials that achieve both transparency and sound absorption performance. We also resolved the panel vibration problem. Our solution to the challenge of reducing panel vibration achieved improved sound absorbing performance and enabled us to develop Eco Kyuon Clear™ note 2), 1), 2), a transparent sound absorbing panel.

1. Performance of thin microperforated aluminum plates

1.1 Principles of sound absorption by microperforated plates

This section presents the principles of sound absorption by microperforated plates. As illustrated in **Fig. 1**, the sound absorbing panel is a multilayered structure of perforated plates and air spaces. **Fig. 2**

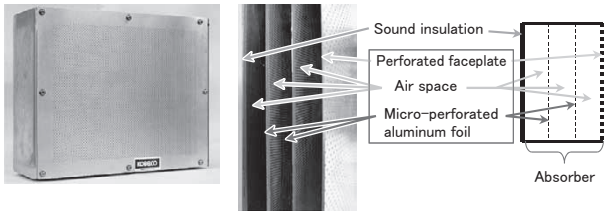

Fig. 1 Example sound absorbing panel structure

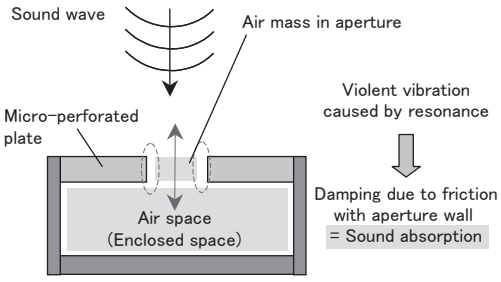

Fig. 2 Principles of sound absorption

note 1) Eco Kyuon is the translation of a registered Japanese trademark "エコキューオン" (No.5129527) of SHINKO KENZAI LTD.

note 2) Eco Kyuon Clear is the translation of a registered Japanese trademark "エコキューオンクリア" (No. 5481495) of SHINKO KENZAI LTD.

diagrams the principle of sound absorption with an enlarged view of an aperture in a perforated plate and an air space. The basic principle is that of a Helmholtz resonator, in which the air in the aperture of the perforated plate and the air in the space act as an acoustic mass-spring resonance system. The friction generated from the viscous damping that occurs between the air in the aperture and the aperture periphery during acoustic resonance leads to sound absorption. In essence, noise is absorbed when acoustic energy is converted via friction into heat energy. Although conventional sound-absorbing mechanisms comprising acoustically resonant perforated plates have been available for some time, we have achieved increased frictional damping in the apertures, improved sound absorption coefficient, and wideband sound absorption characteristics by shrinking the apertures to diameters of 1 mm or less.

1.2 Predicting the sound absorption coefficient

The sound absorption coefficient can be predicted for and designed into a soundabsorbing structure employing a microperforated plate[3]. Assuming a one-dimensional plane wave propagation, the Transfer Matrix Method can be used to estimate the coefficient. The relationship between the sound pressures (p1, p2) and particle velocities (u1, u2) upstream and downstream of the perforated plate depicted in **Fig. 3** is expressed by Eq. (1):

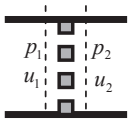

Fig. 3 Microperforations

$$\begin{Bmatrix} p_1 \\ u_1 \end{Bmatrix} = \begin{bmatrix} 1 & \frac{\Gamma_1}{\alpha} \\ 0 & 1 \end{bmatrix} \begin{Bmatrix} p_2 \\ u_2 \end{Bmatrix} \quad \cdots\cdots (1)$$

$$\Gamma_1 = j\omega M_A + R_A$$

$$M_A = \rho_0 \cdot (l_A + 1.6a(1 - 1.47 \cdot \alpha^{0.5} + 0.47 \cdot \alpha^{1.5}))$$

$$R_A = \frac{2R_V(l_A + l_R)}{a},\ l_R \cong 2a$$

where ω is the angular frequency, l_A is the plate thickness, α is the aperture ratio, $2a$ is the aperture diameter, R_V is the viscous resistance coefficient for the wall surface, and ρ_0 is the density of air.

Note that M_A is the open end corrected acoustic inertance of the aperture and R_A is the acoustic resistance. The underlying principle for sound absorption by a perforated plate lies in the attenuation due to the acoustic resistance generated by the friction between the aperture wall and the vibrating air in the aperture.

By multiplying the transfer matrices of the perforated plate and the air space together, the normal incident sound absorption coefficient can then be calculated from the specific acoustic impedance of the surface of the absorber structure.

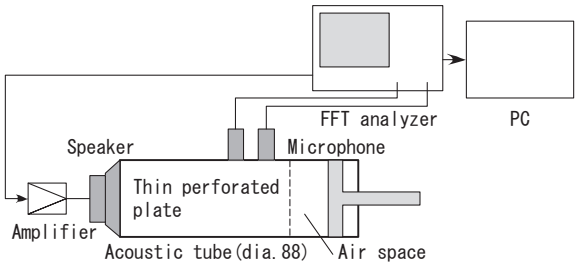

Fig. 4 Measurement device and thin perforated plate location

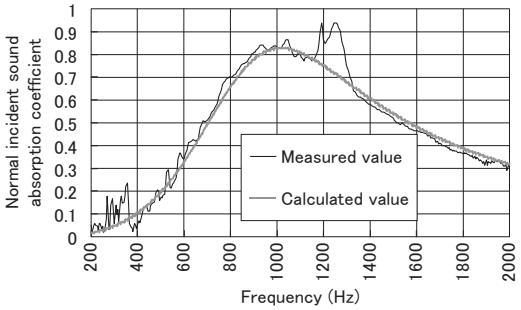

Fig. 5 Normal incident sound absorption coefficient for single microperforated plate

1.3 Normal incident sound absorption coefficient measurement

To measure the normal incident sound absorption coefficient of the microperforated aluminum absorber structure, we employed the two-microphone method [4], in which a thin microperforated aluminum plate is clamped between metallic rings and fastened to the inside of a tube.

Fig. 4 is a basic diagram of the device and the fastened thin microperforated aluminum plate. The thickness of the perforated plate was 0.3 mm, the aperture diameter was 0.5 mm, and the air space depth was 40 mm. **Fig. 5** shows the results of the absorption coefficient measurements and calculations. The calculated values and measured values matched well.

2. Development of sound absorbing panels with microperforated structures

2.1 Structure of sound absorbing panels

Sound absorbing panels with a microperforated aluminum absorber structure were used as a countermeasure against traffic noise. **Fig. 6** is a diagram of the sound absorbing panel dimensions and cross section and **Fig. 7** depicts the external

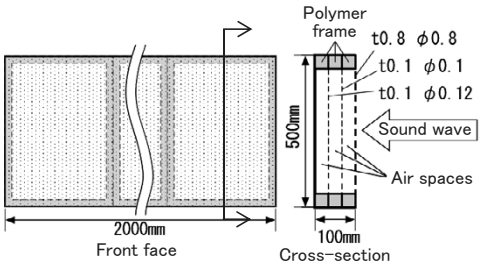

Fig. 6 Diagram of microperforated aluminum sound absorbing panel

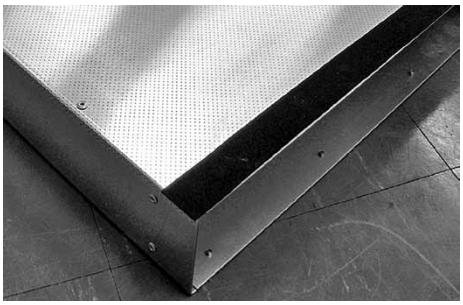

Fig. 7 Microperforated aluminum sound absorbing panel

appearance of the panel face. The main panel body is constructed from steel sheeting, with a thin, 0.8 mm-thick microperforated aluminum plate installed on the face of the panel. Two leaves of microperforated aluminum foil were also fastened internally with polymer frames. The polymer frames form and maintain the air spaces. The polymer frames also double as lengthwise partitions for the air spaces.

2.2 Sound absorption performance

The acoustic panel presented in this report was developed mainly for railroad applications and optimized for noise generated by passing railroad cars. The major component of noise from passing railroad cars is rolling noise with a frequency range between 400 Hz to 4 kHz and a high relative noise level. We therefore applied the method described in Section 1 to optimize the frequency characteristics for maximum absorption of rolling noise and finalized the specifications for the thin perforated aluminum plate, perforated foils, and air spaces. The fabricated sound absorbing panel structure was assembled inside the acoustic tube described in Fig. 4 to measure its normal incident sound absorption coefficient. The measurements were compared with the calculated values. The results are shown in **Fig. 8**. The calculated values and measured values matched very well.

2.3 Example of noise reduction effect

The designed sound absorbing panels were experimentally installed onto a non-absorbing noise barrier along a regular rail line that runs on a concrete slab track. The noise levels of passing trains before and after installation of the sound absorbing panels were compared to quantify the noise reduction effect. **Fig. 9** is a photograph of the installed sound absorbing panels. **Fig.10** shows the frequency analysis results and the relative sound pressure levels of passing trains before and after the installation of the sound absorbing panels at the measurement location. The measurement location was 14.3 m from the track noise barrier and at a height of 0.6 m from the top of the rail. A comparison of the pre- and post-installation speeds

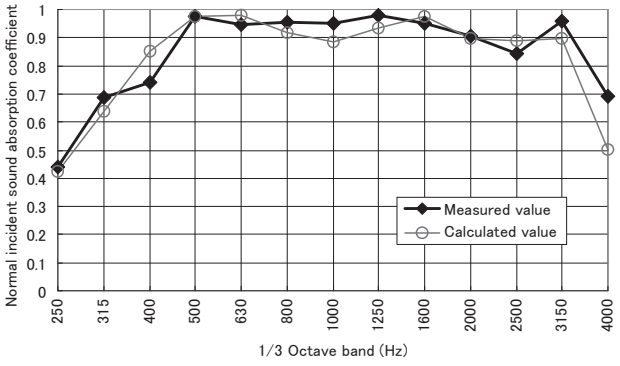

Fig. 8 Normal incident sound absorption coefficient

Fig. 9 Installation of microperforated aluminum sound absorbing panels

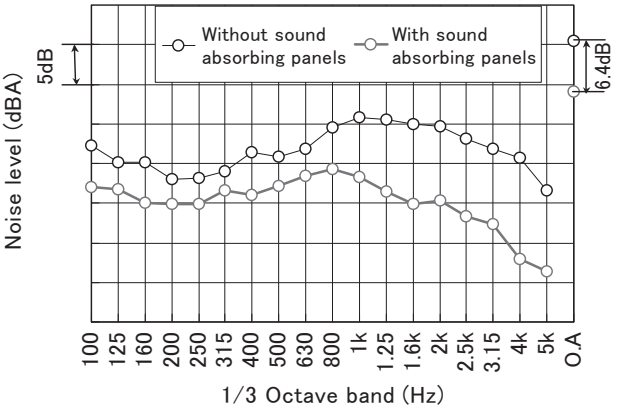

Fig.10 Frequency analysis results

of the passing trains indicated that the speed of the train after the sound absorbing panel installation was 3% faster.

We can see from Fig.10 that the installation of the sound absorbing panels achieved a 6.4 dB reduction in noise, with even greater noise reductions in the frequency range above 800 Hz.

3. Development of transparent sound absorbing panels

3.1 Application of transparent materials

Polymers are the material of choice for transparent applications of the microperforated soundabsorbing technology discussed in Section 1. However, the concern was the drop in the sound absorption coefficient of polymer films of the same thicknesses as the metal foils. Since polymers have less mass and stiffness, they are susceptible to panel vibration in comparison to microperforated metal sound-absorbing plates. Panel vibration causes the relative velocity of the vibrating air in the aperture to drop and compromise the sound absorption efficiency, which is dependent on friction.

To address this issue, we measured the normal incident sound absorption coefficient of microperforated polymer materials backed by an air space. The thin microperforated polymer plates had thicknesses between 0.075 mm and 0.3 mm. We employed the two microphone method described in Section 1.3 to compare the calculated values with the measurements. The microperforated sheet was fastened inside the tube so as to leave room for a 40 mm deep air space. The results are shown in **Figures 11-13**.

As can be seen from Figures 11-13, the greater

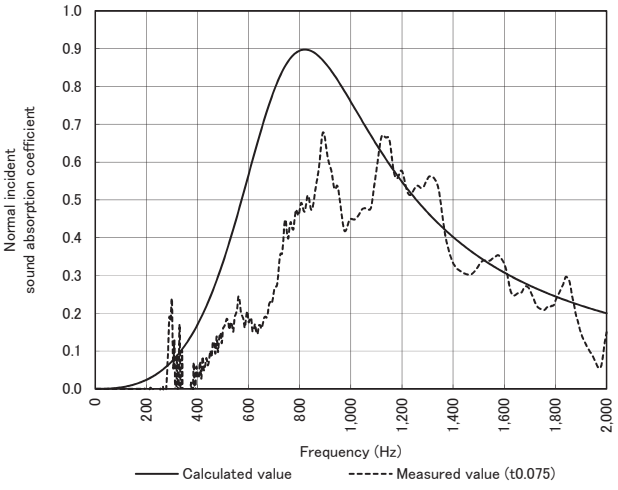

Fig.11 Comparison of normal incident sound absorption coefficient (Thickness=0.075 mm)

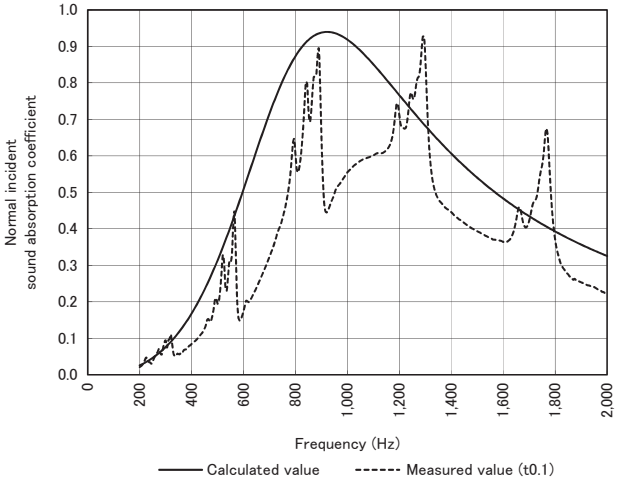

Fig.12 Comparison of normal incident sound absorption coefficient (Thickness=0.1 mm)

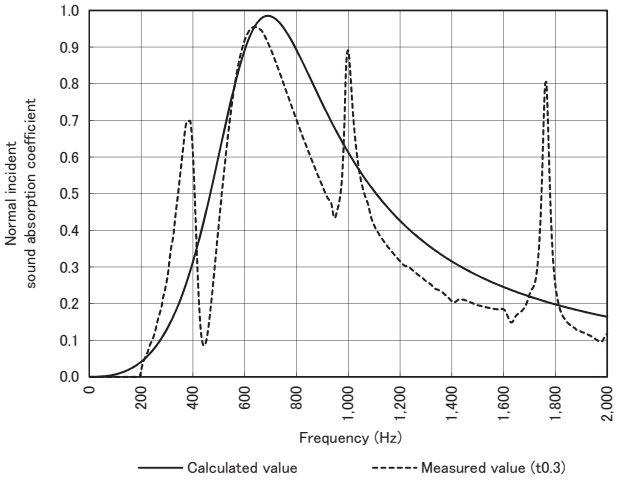

Fig.13 Comparison of normal incident sound absorption coefficient (Thickness=0.3 mm)

the plate thickness, the better the match between the measured values and calculated values. In other words, increased plate thickness reduces the effect of panel vibration and achieves efficient sound absorption performance. Based on the above results, we selected transparent sound-absorbing sheet materials with a thickness of 0.3 mm or greater.

3.2 Study of sound absorber configuration

This section discusses the study of a sound absorbing panel made from a transparent polymer with a microperforated soundabsorbing structure configured for vehicle road noise. The sound absorbing panel was configured with a thickness of 95 mm for the highway application. The method from Section 1 was employed to study configurations to satisfy the criteria established by each NEXCO company and Japan's Ministry

Table 1 Configuration of the sound absorber structure

	Constitution
Design element	Dimension
Surface plate thickness	2 mm
Surface plate aperture ratio	9.0%
Surface plate aperture diameter	1.9 mm
Air space depth	25 mm
First film thickness	0.5 mm
First film aperture ratio	0.9%
First film aperture diameter	0.4 mm
Air space depth	25 mm
Second film thickness	0.5 mm
Second film aperture ratio	0.3%
Second film aperture diameter	0.4 mm
Air space depth	27 mm
Back plate thickness	8 mm

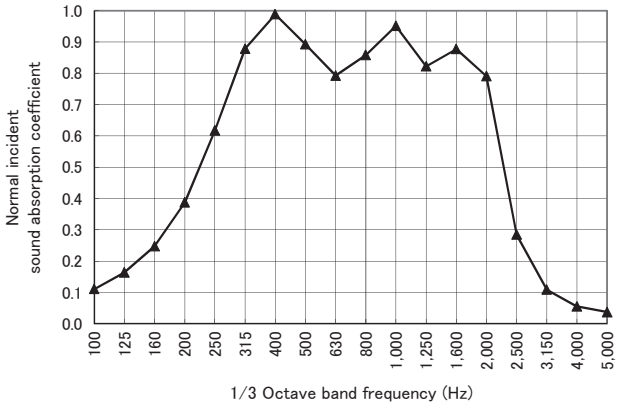

Fig.14 Normal incident sound absorption coefficient

of Land, Infrastructure, Transport and Tourism for road noise sound absorbing panels (Sound absorption coefficient of 0.7 or greater for 400 Hz and 0.8 or greater for 1 kHz, using the reverberation room method). **Table 1** describes the configurations for the panels. **Fig.14** shows the calculated results for the normal incident sound absorption coefficient.

3.3 Development of commercial transparent sound-absorbing panel

Based on the study above, a prototype transparent sound absorbing panel was fabricated to product-level specifications. The sound absorption coefficient of the prototype was measured with the reverberation room method. **Fig.15** is a schematic drawing of the prototype panel and **Fig.16** depicts the external appearance of the prototype.

Fig.17 presents the sound absorption coefficient measurement results from the reverberation

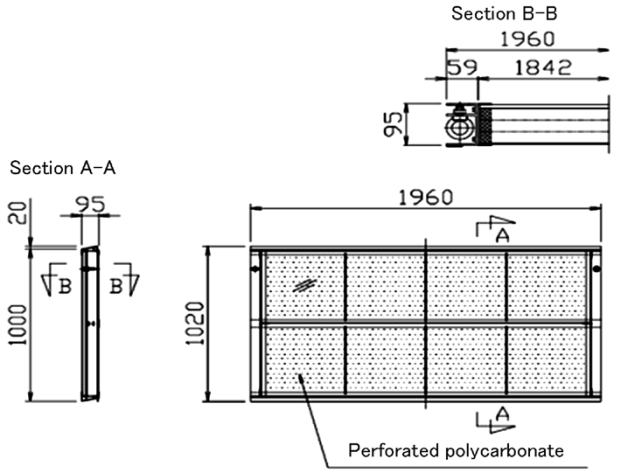

Fig.15 Schematic drawing of prototype panel

Fig.16 External appearance of transparent sound absorbing panel

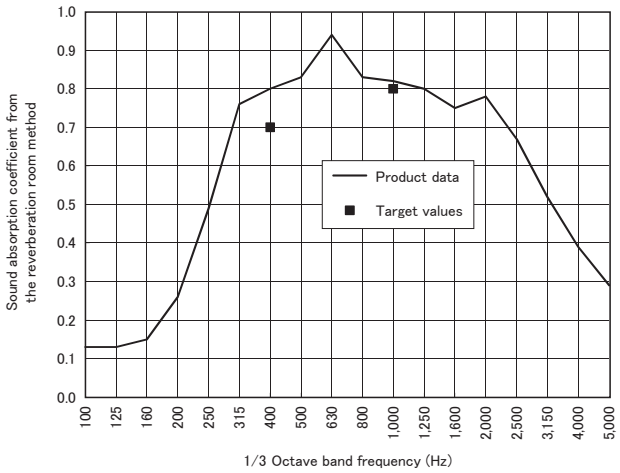

Fig.17 Sound absorption coefficient from reverberation room method

room method. The results confirm that the sound-absorbing performance satisfies the above-mentioned criteria as designed. We also verified that one can adequately see through the panel (as can be seen in Fig.16). This study therefore verifies that the

Fig.18 Installation example

sound absorbing panel is both sound absorbing and transparent.

Since its development, this product has been officially selected by Shizuoka Prefecture for use on its prefectural roads and by the Nagoya Expressway Public Corporation. **Fig.18** is an example of an installation for the Nagoya Expressway.

Conclusions

Since sound absorbing panels constructed with thin microperforated plates and foils and air spaces can be designed with optimized frequency characteristics, sound absorbers that match the noise characteristics of the target noise can be manufactured. The development of microperforated sound absorbing panels for rail and road noise applications using this technology contributes to the reduction of traffic noise. Additionally, commercial sound absorbing panel products that are both sound absorbing and transparent basically do not exist for the noise barrier market at this time. Much growth is anticipated for such sound absorbing panels where visibility and translucency are requirements.

Therefore, microperforated sound absorbing panels have potential for a broad array of applications and hold much promise going forward.

References

1) M. Horio et al. *Kobe Steel Engineering Reports*. 2014, Vol.65, No.1, p.84-88.
2) I. Yamagiwa et al. *Proceedings of the Autumn Meeting of the Institute of Noise Control Engineering Japan*. 2013, p.289-292.
3) T. Yamada et al. *Proceedings of the 17th Environmental Engineering Symposium*. 2007-7-19/20, p.39-41.
4) H.Utsuno et al. *The Journal of the Acoustical Society of America*. 1989, Vol.86, No.2, p.637-643.

Low Loss Reactor Comprising Dust Core and Copperbelt Coil

Hiroshi HASHIMOTO*1, Kyoji ZAITSU*1, Shumpei HAYASHI*1, Hiroyuki MITANI*2, Dr. Kenichi INOUE*3

*1 Electronics Research Laboratory, Technical Development Group
*2 Research & Development Planning Dept., Technical Development Group
*3 Technology Unit, Kobelco Research Institute, Inc.

To achieve the downsizing and weight reduction of voltage boosters for hybrid and electric cars, a voltage boosting reactive coil made by winding a flat, thin copperbelt of about 0.1 to 0.3 mm in thickness was contemplated. The coil was enclosed in a pot-shaped magnetic core made of pure iron powder. Numerical analysis and a model experiment indicated the possibility of making a reactor with a coil having a high-frequency loss that has been reduced to one-third to one-tenth that of conventional reactors and has excellent heat dissipating properties. This technology has enabled the downsizing of the reactor.

Introduction

With the recent global rise in environmental awareness, hybrid electric vehicles (hereinafter, HEVs) and electric vehicles (hereinafter, EVs) are spreading rapidly, thanks to their low CO_2 emissions. An HEV/EV system comprises more than one electric motor for driving and for generating power and requires the downsizing of the motors and batteries to improve the energy efficiency. To this end, each system mainly employs a power unit with a boost circuit (**Fig. 1**) that increases the battery voltage of 200-300 V to the motor-driving voltage of 400-800 V[1)-3)].

The reactor in a booster circuit is a core component that serves to boost the input voltage from the inverter with the action of, switching devices that turn on and off to alternately charge and discharge magnetic energy, and to smooth the ripple in the electric current generated during the voltage conversion. Such a reactor is required to keep its inductance at, or higher than, a predetermined value (in general, an L-value of 200-300 μH) even under a high current of several hundred amperes. Hence, it is designed to have large gap spacing so as to avoid the saturation of its magnetic core. Large gap spacing, however, increases the leakage flux from the gap and the amount of interlinkage flux into the coil conductor, increasing eddy current. As a result, the gap must often be separated into several sectors so as to minimize the amount of gap spacing per sector. Otherwise, the distance between the gap and coil must often be increased. These efforts inevitably cause an increase in the number of components and/or the upsizing of the coil.

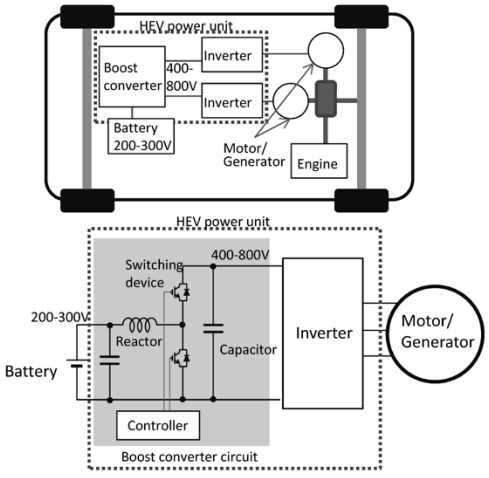

Fig.1 HEV system with boost converter circuit

Downsizing and weight reduction are imperative for any automotive components. To this end, studies are being conducted to decrease the required inductance by increasing the operation frequency (≧20 kHz) of boost converters[4)]. Increasing the frequency, however, leads to an increased loss in the reactor, posing a problem.

These problems have been solved by combining a pot-type reactor having a magnetic core made of iron powder (hereinafter, dust core) with a flatwise coil made of a copperbelt. Numerical analysis and a model experiment have demonstrated that the combination can decrease the coil loss while improving heat dissipation and thus enable the downsizing and weight reduction of the reactor. The following presents the outline.

1. Design concept and numerical analysis

1.1 Downsizing of reactor and improvement of heat dissipation performance

The basic structure of a conventional reactor is shown in **Fig. 2**. The inductance L, a major characteristic, is expressed by Equation (1):

$$L=\frac{\mu_0 \cdot S \cdot N^2}{\frac{\ell_c}{\mu_c}+\ell_g} \quad \cdots\cdots (1)$$

wherein S is the cross-sectional area of the flux path; ℓ_c, flux path length; ℓ_g, gap length; μ_0, vacuum permeability; μ_c:, relative permeability of magnetic core; and N, the number of turns in the coil.

Fig. 3 shows a known pot-type reactor, in which a coil is wrapped in a dust core. Such reactors have

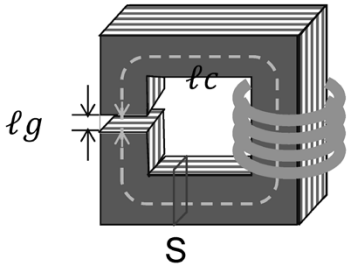

Fig. 2 Basic structure of reactor

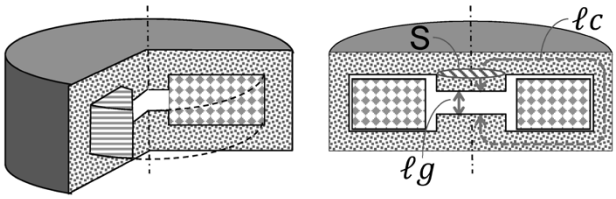

Fig. 3 Structure of pot-type reactor

been applied to noise filters with small capacities. Compared with a conventional reactor as shown in Fig. 2, a pot-type reactor has the advantage of allowing a shorter flux-path length ℓ_c and a greater flux-path cross-sectional area S. Hence, despite its smaller volume, a pot-type reactor can achieve inductance comparable with that achieved by a conventional reactor.

A pot-type reactor, however, has a coil wrapped by a magnetic core, which allows the coil to be cooled only through the magnetic core. Thus, when it comes to cooling, the pot-type reactor is at a disadvantage compared with the conventional structures. The reactors for HEVs and EVs are subject to high current. Thus it is most important for the coil to have high performance in heat dissipation. This has restricted the use of pot-type reactors.

Reactor coils are conventionally made of sheathed round wires, which have excellent workability and are inexpensive. On the other hand, from the aspect of coil cooling, the reactors for HEVs/EVs employ edgewise coils made of rectangular copper wires with large cross-sectional areas and low resistances. **Fig. 4** illustrates the heat-transfer structure of a pot-type reactor to which an edgewise coil has been adapted. This structure has an increased thermal conductivity in the radial directions; however, it suffers from inevitably poor thermal conductivity in the axial directions due to the increased number of heat transfer interfaces. Therefore, a pot-type reactor adapting an edgewise coil inevitably has the shape of an extended cylinder, which is a shape that is disadvantageous for inductance, and must be cooled from its outer circumferential surface or from the side of its central axis.

Against this backdrop, a structure was contemplated having a copperbelt wound flatwise as shown in **Fig. 5**. A heat transfer structure with a coil end in contact with the magnetic core results in low thermal conductivity in the radial direction of the reactor, but increases thermal conductivity in the axial direction, enabling cooling from the top and bottom surfaces of the reactor. This enables the reactor to have a flat shape, which is advantageous in securing inductance. In the cases of HEVs and EVs, downsizing as a whole can more easily be achieved by placing heat-generating components, such as reactors and switching elements, in contact with planar-shaped water-cooled heatsinks. Hence, the cooling structure adapting a flatwise coil is more suitable.

1.2 Reduction of coil loss during high-frequency operation

Reactor losses are classified into hysteresis loss/eddy-current loss occurring in magnetic cores and Joule loss/eddy-current loss occurring in coil conductors. As has been described, a reactor for an HEV/EV has large gap spacing, which is indispensable for avoiding the magnetic saturation of the core. This makes significant the loss due to the eddy-current generated in the conductor by the leakage flux from the gap. It is thus important to reduce the eddy-current loss in the coil to achieve, *inter alia*, downsizing and high-frequency.

Eddy current is generated in a coil when external magnetic flux intersects with the copper wires of the coil. The eddy current can be minimized if the copper wire is made sufficiently smaller in diameter than the skin depth of the eddy current; however, there is a trade-off in that the smaller the cross-sectional area of a lead the greater the direct current

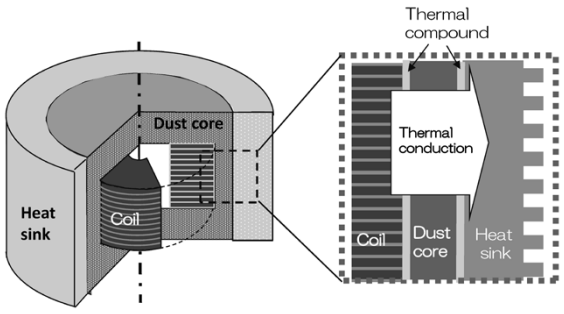

Fig. 4 Heat transfer structure of edgewise coil

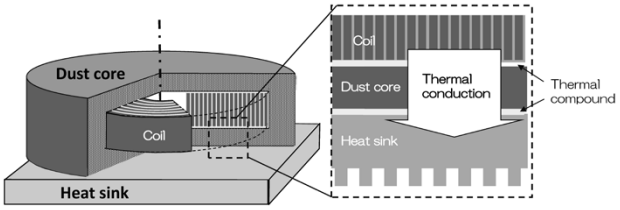

Fig. 5 Heat transfer structure of flatwise coil

(DC) resistance, which increases copper loss (i.e., Joule loss).

The skin depth δ of eddy current flowing in a conductor is given by Equation (2):

$$\delta = \sqrt{\frac{2}{\omega\mu\sigma}} \quad \cdots\cdots (2)$$

wherein ω is angular frequency, μ is the magnetic permeability of the conductor, and σ is the electrical conductivity of the conductor. That is, the higher the frequency the shallower the skin depth δ. **Fig. 6** shows the relationship between skin depth in copper coil and frequency f ($=\omega/(2\pi)$).

Now let us compare the eddy currents in the conventional and in the newly proposed structures used for pot-type reactors with large gap spacing. A copperbelt having a thickness of 0.3 mm and a width of 20 mm was made into a edgewise coil (DC resistance, 16 mΩ), which was adapted for a pot-type magnetic core with a gap spacing of 10 mm. As shown in **Fig. 7** (a), the flux crosses the wide surface of the coil, generating eddy current in the coil.

The magnetic field created by the eddy current in the coil is applied in the direction that cancels the magnetic flux of the reactor, which, as a result, decreases the inductance of the reactor. For this setting, the relationships of the operating frequency, inductance and alternating current (AC) resistance

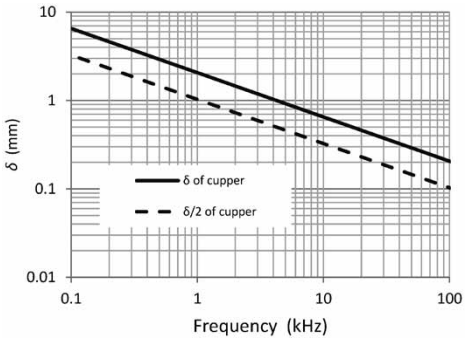

Fig. 6 Relationship between skin depth in copper coil and frequency

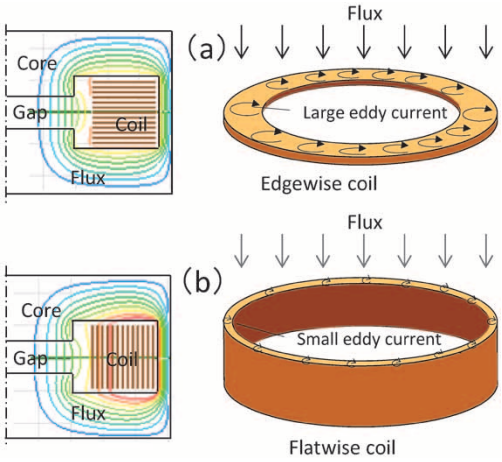

Fig. 7 (a) Eddy current in edgewise coil
(b) Eddy current in flatwise coil

were analyzed using electromagnetic-field-analysis software (ANSYS Maxwell). The results are shown in **Fig. 8** and **Fig. 9** (blue line).

In the case of the edgewise coil, the inductance decreases with increasing frequency. As shown, the inductance at the operating frequency of 10 kHz is almost 15% smaller than that at low frequency (100 Hz). The AC resistance at the operating frequency of 10 kHz becomes as high as 0.2 Ω, which is a factor of 12 greater than the direct current resistance of 16 mΩ.

Next, we studied eddy-current loss *Pe* occurring in the coil. As expressed by Equation (3), the value of *Pe* is calculated from the second power of the alternating current flowing through the reactor, and the AC resistance:

$$P_e = R_{ac} \cdot I_{ac}^2 \quad \cdots\cdots (3)$$

wherein R_{ac} is the AC resistance, and I_{ac} is the effective value of the alternating component of the current flowing through the reactor.

The effective value, I_{ac}, of the alternating component of the current flowing through the reactor is approximated by Equation (4):

$$I_{ac} \cong \frac{V_i\left(1-\frac{V_i}{V_o}\right)}{4Lf} \quad \cdots\cdots (4)$$

wherein V_i is the voltage before booster; V_o, voltage after booster; L, inductance; and f, operating frequency.

For the voltage before booster of 200 V, voltage after booster of 600 V, reactor inductance of 300 μH

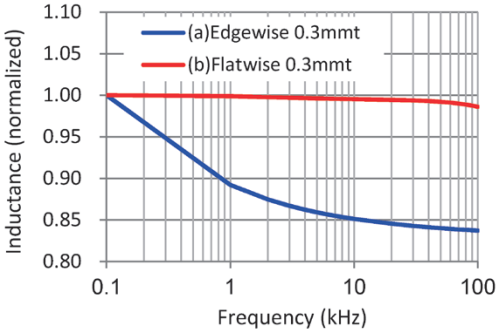

Fig. 8 Inductance frequency response (analysis)

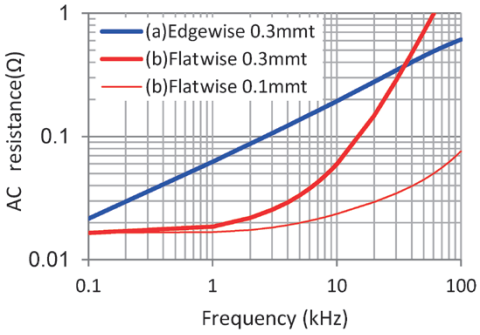

Fig. 9 AC resistance frequency response (analysis)

and operating frequency of 10 kHz, Equation (4) yields the alternating current I_{ac} of 11 A. Given the AC resistance of 0.2 Ω, Equation (3) yields the coil eddy-current loss of 24 W.

In contrast, when a flatwise coil as shown in Fig. 5 is adapted for a pot-type reactor, the flux generated in the coil space of the reactor penetrates through the copperbelt in the transverse direction of the copperbelt, as shown in Fig. 7 (b). Here, the thickness, t, of the copperbelt is set to be equal or smaller than half the skin depth, which makes the eddy current in the copperbelt small enough to prevent the decrease in inductance and the increase in AC resistance, the aforementioned problems encountered when using an edgewise coil. The upper limit, $\delta/2$, for the copperbelt thickness is depicted by the broken line in Fig. 6. For example, in the case of a typical reactor for current HEV/EV, operating at a frequency of approximately 10 kHz, a copperbelt thickness of 0.35 mm or smaller should suppress the eddy current effectively. For the operating frequency of 40 kHz, envisaged in the further downsizing of reactors, a copperbelt thickness of 0.15 mm or smaller would serve the purpose.

As an example, a magnetic field analysis was conducted on the case where a copperbelt of 0.3 mm thick and 20 mm wide is fabricated into a flatwise coil (direct current resistance, 16 mΩ) and is adapted to a magnetic core with a gap spacing of 10 mm. The resulting inductance and AC resistance are shown in Fig. 8 and Fig. 9 (red line). Unlike the edgewise coil, the flatwise coil has an inductance that remains almost unchanged in the range from low frequency to 10 kHz. Its AC resistance at 10 kHz is about 60 mΩ, which makes the eddy-current loss of the coil in the aforementioned booster operating condition to be 7 W, the value suppressed to 1/3 or less of the loss for the edgewise coil. It should be noted, however, that the higher frequency decreases the skin depth; and, in the high frequency region where $\delta/2$ becomes smaller than 0.3 mm, the AC resistance increases rapidly.

Hence, operation in the higher-frequency region requires a copperbelt having a thickness of half the skin depth ($\delta/2$), or thinner, at that operating frequency. Fig. 9 (red thin line) depicts the AC resistance for a copperbelt thickness of 0.1 mm, in which case, the AC resistance is suppressed up to 100 kHz, the frequency corresponding to $\delta/2$.

As has been described, winding a copperbelt with a thickness suitable for the operating frequency, in a flatwise manner makes possible a reactor with small eddy-current loss and excellent inductance characteristics at high frequencies.

2. Model experiment

Two models having pot-type dust cores with wide gap spacing, as described previously, were prepared, one including an edgewise coil (Coil a) and the other including a flatwise coil (Coil b). Their inductance, AC resistance and the heat transfer performance of their coils were measured. **Fig.10** shows the construction of the dust cores used in this model experiment. The specifications of the coils are shown in **Table 1**, and the design parameters of the reactors are shown in **Table 2**. Each dust core was made of insulated magnetic powder having an average grain size of approximately 100 μm or smaller so as to sufficiently minimize the eddy current loss that occurs in the magnetic core.

The analysis assumed a conductor model comprising an edgewise coil 0.3 mm thick and 20 mm wide; however, such a coil turned out to be difficult to wind. Hence, the measurement model adopted a thickness of 0.8 mm and a width of 10 mm.

2.1 Measurement results for electrical characteristics

The inductance-frequency responses of the coils were measured as their electrical characteristics when inserted in dust cores. The results are plotted in **Fig.11**. Also shown in the figure are the curves obtained by numerical analyses conducted under the same conditions as the experimental models.

The edgewise coil (Coil a, blue line) exhibits inductance decreasing as the frequency increases,

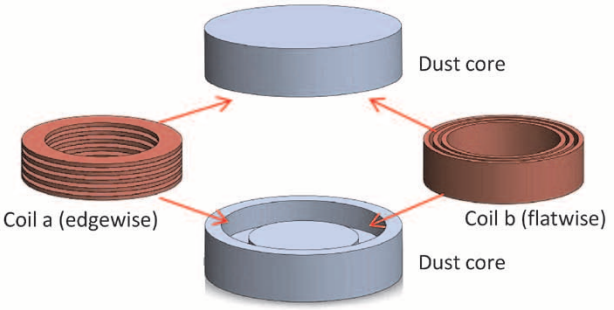

Fig.10 Construction of experimental models

Table 1 Coil specifications

	Inside diameter (mm)	Outside diameter (mm)	Wire diameter (mm)	Wire turns	weight (g)	DC resistance (mΩ)
Coil a (Edgewise)	60	80	0.8t×10	23	320	12.7
Coil b (Flatwise)	65	80	0.3t×20	23	260	16.5

Table 2 Design parameter of reactor

	S (mm^2)	ℓc (mm)	ℓg (mm)	μ_c	Wire turns
Design parameter of reactor	1,900	140	10	90 - 110	23

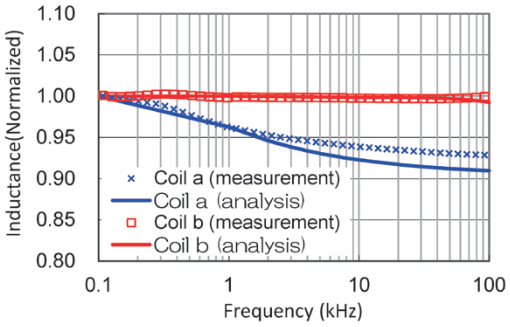

Fig.11 Inductance frequency response

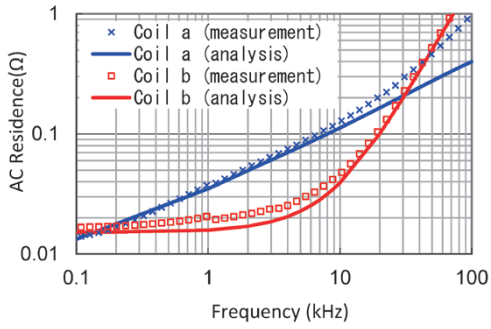

Fig.12 AC resistance frequency response

and the inductance at 10 kHz is approximately 6% smaller than that at a low frequency of 100 Hz. The flatwise coil (Coil b, red line), on the other hand, exhibits an almost constant inductance up to a frequency of 100 kHz. In the case of the flatwise coil, the experimental results agree well with what was predicted by the numerical analysis. In the case of the edgewise coil, the analysis and experiment agree in the frequency range lower than several kHz or so; however, the analysis cannot fully reproduce the behavior of the coil eddy current in the high-frequency range, causing an error of approximately 2%.

Fig.12 shows the AC resistance-frequency responses of the coils, including the analysis values and measured values. The flatwise coil made of 0.3 mm thick copperbelt exhibits lower AC resistances, which are suppressed lower than those of the edgewise coil, in the frequency range lower than about 10 kHz. Thus, appropriately selecting the copperbelt thickness for a flatwise coil in accordance with the operating frequency enables a significant reduction of eddy-current loss occurring in the coil. It should be noted, however, that although the results of experiment and numerical analysis agree with a high accuracy for the flatwise coil, the edgewise coil exhibits a significant discrepancy between the analyzed and measured values as the frequency increases to over 10 kHz. There remains an issue of analysis accuracy in the high-frequency range.

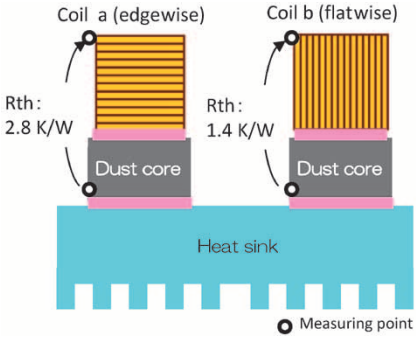

Fig.13 Thermal resistance of coils

2.2 Heat dissipation characteristics

The thermal conductance/resistance was measured for edgewise and flatwise coils and the results are shown in **Fig.13**.

In this experiment, a resin with a thermal conductivity of 1.1 W/mK was coated on the interface between the copperbelt in each coil and each dust core. Direct current of approximately 50 A was applied so as to induce a loss of 30 W in the coil. The resulting thermal resistance, *Rth*, between the top of the edgewise coil and the dust core was 2.8 K/W, and that between the top of the flatwise coil and the dust core was 1.4 K/W. The thermal resistance of the flatwise coil had decreased to half of that of the edgewise coil, confirming the excellent heat transfer characteristics of the flatwise coil.

3. Discussions

Table 3 summarizes, for comparison, the characteristics measured for both models. Compared with the currently predominantly-used edgewise model, the newly proposed flatwise model is superior in exhibiting smaller AC resistance at approximately 10 kHz, the frequency in the operating frequency range for current HEVs/EVs, and in heat transfer to heatsinks. As described in Section 1, selecting a copperbelt thickness of less than half the skin depth that corresponds to the operating frequency can further significantly reduce the AC resistance, i.e., the eddy-current loss of the coil, during high-frequency operation. Hence, adapting the newly proposed structure to reactors for the power units for HEVs/EVs, the units required to

Table 3 Summary of experimental results

	Inductance reduction rate(%)	AC resistance (mΩ)	Thermal resistance (K/W)
Condition	10Hz to 10kHz	@10kHz	From coil to core
Coil a (Edgewise)	−6	130	2.8
Coil b (Flatwise)	0	50	1.4

accommodate high current, which are to be downsized, will enable the gaps to be widened to suppress the magnetic saturation at high current and allow the operating frequency to be increased for downsizing.

Edgewise coils require special plastic working in the coil winding process, which makes thin copperbelts difficult to fabricate for use at high frequencies. By contrast, flatwise coils can be made by a simple tape-winding process and are more advantageous in terms of process cost.

The low-loss reactors herein proposed, comprising dust cores and copperbelt coils, are applicable not only to HEVs/EVs, but also to other booster reactors and AC filters for power conditioners used in renewable energy applications that are subject to power variation.

Conclusions

It has been demonstrated that combining a pot-type dust-core reactor with flatwise coil made of a copperbelt [5),6)] can realize a reactor that operates at high current with high-heat-dissipation and is suitable for HEV/EV applications. Also demonstrated was the fact that selecting a copperbelt thickness for the operating frequency can significantly reduce eddy-current loss occurring in the coil. The reactors for HEVs/EVs are expected to be downsized thanks to the proposed structure exploiting the features of dust cores.

References

1) H. Yaguchi et al. *TOYOTA Technical Review*. 2010, Vol.57, No.1, pp.12-19.
2) J. Kuroki et al. *Honda R&D Technical Review*. 2013, Vol.25, No.2, pp.41-47.
3) S. Yamamoto et al. *SEI Technical Review*. 2014, No.185, pp.29-33.
4) H. Kawahara et al. *Proceedings of the Annual Meeting of the Institute of Electrical Engineers of Japan*, 2015, Vol.4, p.153.
5) *JP Patent No.4654317*; also WO2011/007879.
6) *JP Patent No.5149976*; also WO2012/137494.

New Roll-to-Roll Sputtering System for Wide Film and Application Examples

Toshiki SEGAWA*1, Yoshimitsu IKARI*1, Naoki OOBA*1, Dr. Nobuyuki KAWAKAMI*2, Dr. Norihiro JIKO*2, Hiroaki TAO*2

*1 Advanced Products & Technology Dept., Industrial Machinery Div., Machinery Business
*2 Electronics Research Laboratory, Technical Development Group

A new roll-to-roll sputtering system for wide film substrate is now under development; it is characterized by the connection of unit chambers in the horizontal direction. The new model is an improvement over previous models and is easily disassembled for shipping and assembled for installation; and it has kept the "open chamber concept" of previous models in the way in which the process chamber with sputtering source dynamically moves to the back of the equipment, which allows easy access to the coating zone. It also has sufficient degassing capability, thanks to a specialized degassing chamber unit. This system makes a suitable coating process for touch-panel displays or heat reflective film, etc., where the substrate film is wider. The other R2R coating system models are also introduced.

Introduction

Products having resin films with various functions imparted by vacuum coating are widely used in our daily lives. For example, a package material for snack food or retort food includes a substrate film of polypropylene (PP) or polyethylene terephthalate (PET), with a coating of aluminum (Al) and/or silica (SiOx) deposited on the substrate film so as to suppress the transmission of atmospheric water vapor and oxygen and to prevent deterioration of food quality and extend the expiration date. Conventionally, many food-package materials have had aluminum coating deposited on their surfaces. Lately, package materials with a transparent film deposit of silica and imparted with a function of visibility are also found.

Smartphones and tablet terminals with touch panels have been spreading rapidly in recent years. These touch panels also include resin films with vacuum coating. More recently, in particular, projected capacitive touch panels are being widely used; these panels allow multiple pointing input and gesture functions, for example, moving the fingers to enlarge and shrink pictures. A transparent electrode component disposed on the operation surface of such a touch panel comprises a hard-coated PET substrate having an optical adjustment layer, index matching (IM) layer and indium-tin-oxide (ITO) film layer deposited on it. The layers are patterned for multi-wiring by etching. A patterned monolayer of ITO film, however, can be slightly visible. Hence an optical adjustment layer is formed on the ITO film layer so as to make the pattern less visible.

Coating on flexible substrate often involves the use of a system called "roll-to-roll" (hereinafter "R2R"), which has high productivity. In a R2R, a substrate film rolled in the shape of a hollow cylinder is mounted as-is in the system. The unwound film is guided by cylindrical rollers to be continuously processed at each step and is finally wound up again into a hollow cylindrical roll as a film-deposited product.

With the recent trend of large touch panels, the substrate width has been increasing from 400 mm to 500 mm. Large R2R sputtering systems that were designed to accommodate a substrate width of 1,300 mm (for three 400 mm wide pieces) are now being required to accommodate a substrate width of 1,600 mm (for three 500 mm pieces). Large-area applications, such as films affixed to window glass to block the sunlight, require a product width of 1,600 mm or greater, so the systems are required to accommodate a substrate width of 1,600 mm for that application, too.

Kobe Steel developed and launched the sales of a unique R2R sputtering system, type W35-S, for functional films having a substrate width of 350-700 mm.[1)] This R2R sputtering system has a vacuum chamber with a unique structure, making the system compact while facilitating easy access to its coating zone. moreover, a large R2R sputtering system, type W50-S, has been added to the lineup to accommodate substrates 1,300 mm wide. This system has a coating zone that is openable (open chamber concept), which facilitates access to the coating zone.

A new large R2R sputtering system model, type W60-S, is being developed in anticipation of the future demand for increasing the substrate width to 1,600 mm. Type W60-S exploits the open chamber concept, which is original to Kobe Steel and facilitates easy access to the coating zone, while resolving problems associated with type W50-S, such as requiring a tall housing and large amounts of time for disassembling and installation. This paper gives an outline of the new model, type W60-S, and its applications, as well as Kobe Steel's lineup of R2R systems.

1. R2R sputtering system, type W50-S

Type W50-S is a large R2R sputtering system for wide films that is based on Kobe Steel's conventional model. This system has a process chamber that mounts sputtering sources and a box-shaped base chamber that mounts a coating drum, in which the process chamber is fully openable to the base chamber (open-chamber concept.) This construction allows easy access to the coating zone and achieves excellent workability for cleaning and changing masks, as well as sputtering targets, while the process chamber is open. **Fig. 1** illustrates the construction of a R2R sputtering system, W50-S type, and **Fig. 2** shows the base chamber of the model W50-1300S system for 1,300 mm wide substrates.

The process chamber is equipped with several turbo molecular pumps (TMPs) so as to realize stable film coating in coating zones that are evenly evacuated. The system includes four coating zones, and the spaces in between the coating zones are also evacuated by TMPs to ensure favorable gas-separation characteristics. An upper chamber is stacked above the base chamber and mounts substrate rolls with large diameters, a degassing zone where the films are degassed by a span-heating method employing plate heaters set between idler rollers, and a monitor for checking film qualities such as film resistance and transmittance before the substrate is wound up.

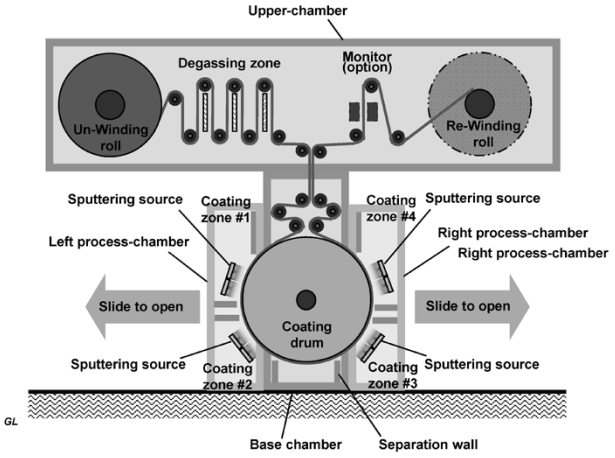

Fig. 1 Schematic of sputtering R2R model W50-S system

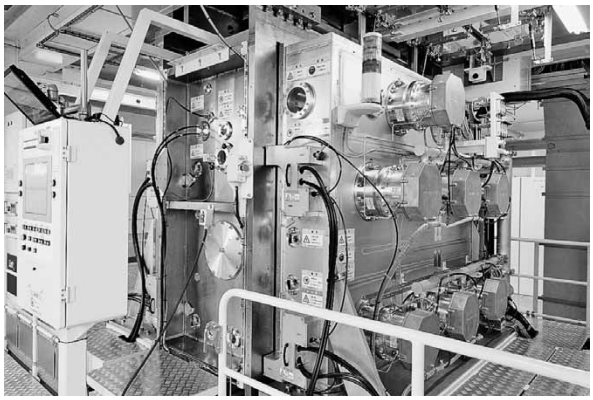

Fig. 2 Base chamber of sputtering R2R model W50-1300S

In the type designation, "W50" represents a R2R apparatus that has chambers, including an openable process chamber stacked, "1300" represents the compatible substrate having a nominal width of 1,300 mm, and "S" represents sputtering.

Thanks to the stacked structure of chambers, the system has the advantages of requiring a small installation footprint and possibly has only the upper chamber being inside a clean room. The other side of the coin is that the system is tall and requires tall housing. Moreover, the upper chamber, being a heavy load, must be disassembled before transportation and be assembled again at the installation site, which poses the problem of taking large amounts of time for disassembling, assembling and installing.

2. Features of new R2R sputtering system, W60-S type

The W60-S is a new type of R2R sputtering system based on the "open-chamber concept" while resolving the above described issues of the W50-S type. The advantages of the W60-S type R2R sputtering system are as follows:

(1) The process chamber is constructed so as to be openable, allowing easy access to the coating zone;
(2) the continuous degassing function, based on the span-degassing method, is unitized and integrated; and
(3) the unit chambers are connected horizontally, facilitating disassembly, transportation, restoration and expansion of the system.

Fig. 3 illustrates the basic configuration of the W60-S type R2R sputtering system. This sputtering system comprises chamber units, each designed to be within a dimensional limit imposed due to transportation, being connected in the horizontal direction. Substrate rolls are loaded and unloaded in a unitized un-winding (UW) chamber and a unitized re-winding (RW) chamber. The degassing mechanism is incorporated in a unitized degassing chamber, which is horizontally coupled with the UW chamber. The coating zones in the base chamber have openings, one on the left side and the other on the right side. The left and right process chambers, having a dovetail on their opening faces, open left and right for approximately 40 cm to avoid interference with the coating drum and

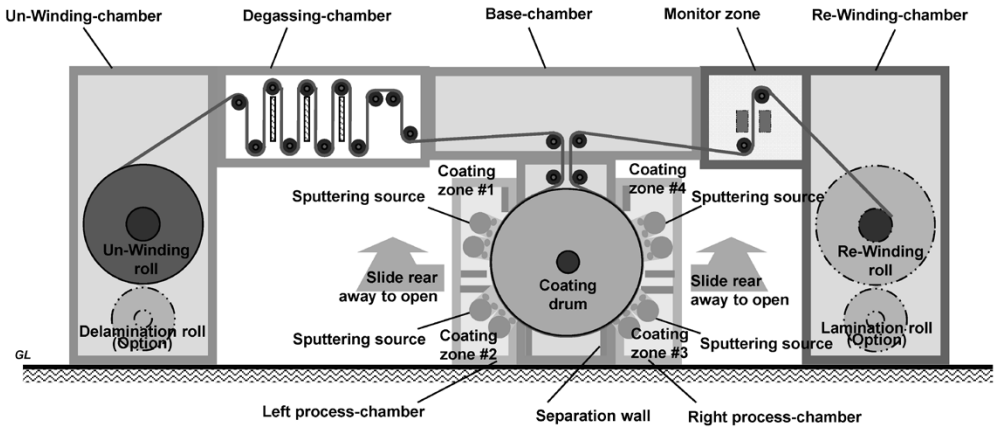

Fig. 3 Schematic of sputtering R2R model W60-S system

Table 1 Main specifications of W60-1600S model

Item	Specifications
Type of chamber structure	Unit chamber horizontal connection
Method to open coating zone	Sliding away of process chamber
Substrate	Plastic film (PET/PEN/PI etc.)
Film thickness	23-200 μ m
Film width	Max. 1,620 mm
Effective width	Max. 1,530 mm
Max. roll diameter	800 mm
Film tension	70-600 N
Film transfer speed	0.5-25 m/min
Diameter of coating drum	1,300 mm
Temperature of coating drum	-15 to 75℃
Number of coating compartments	4 sets
Number of sputtering sources	Max. 2 sets for each compartment
Type of sputtering source	Rotary magnetron or planner magnetron
Power supply	DC/DC pulse/MF-AC
Gas separation	Over 1/100
Type of degassing	Span heating between idler rollers
Degassing length	4 m
Minimum space for installation	15 (width)×19(depth)×5.5m(height)

move largely toward the back so as to expose the coating zones. This structure facilitates the changing of masks and cleaning of the coating zones. The sputtering targets, remaining in the retreated process chamber, can easily be changed. With this chamber structure, the W60-S type R2R sputtering system allows the chambers to be connected horizontally while securing accessibility to the coating zones, and facilitates installation. Thus the system can be introduced more easily than conventional models.

In addition to the conventional planar sputtering sources, the W60-S type accommodates rotary magnetron (RM) sputtering sources. The RM sputtering sources can achieve high target yields and are being adopted widely. A RM sputtering target unit for a nominal 1,600 mm-wide substrate may have a length exceeding 2,000 mm and weigh as much as 100 kg. Hence the W60-1600S model is adapted to support both ends of the target units and equipped with a dedicated hoisting accessory so as to ease the handling of the long target. Another feature is an increased expandability. The unitized UW chamber and RW chamber, for example, can optionally accommodate special rollers for unwinding and rewinding laminated films. The coating drum temperature is controlled by circulating medium, enabling film deposition at low to mid temperatures (-15 to 75 ℃).

Table 1 outlines the specifications of the W60-1600S model accommodating the substrate width of 1,600 mm.

The design development has been completed for the new W60-1600S model and for the W60-1300S model designed for 1,300 mm wide substrates. The base chamber, having a new design (for, e.g., the chamber structure, chamber open/close mechanism, door open/close mechanism, coating drum, pressure bulkhead and RM sputtering sources), has an

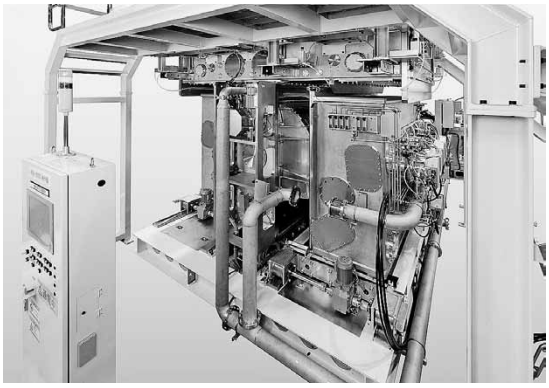

Fig. 4 Base chamber of sputtering R2R model W60-1600S

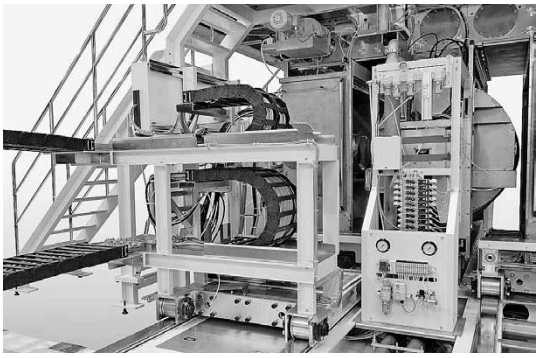

Fig. 5 Base chamber of sputtering R2R model W60-1600S

important effect on system performance. Hence a prototype W60-1600S base chamber has been built and evaluated for its basic performance, including pressure-separation performance, temperature-control function and the uniformity of the deposited films. **Fig. 4** and **Fig. 5** show the base chamber being tested and modified at the Takasago Works of Kobe Steel.

3. Fully equipped degassing function

The features of Kobe Steel's large R2R sputtering systems include a fully equipped degassing function. The degassing process involves a span-heating method, in which films are radiation-heated by plate heaters set between free rollers. The degassing length of 4,000 mm ensures sufficient degassing.

Kobe Steel constructed a dedicated degassing apparatus to propose, through some tests, the optimum process conditions for the span-heating degassing method using plate heaters. **Fig. 6** shows a degassing system (type W35-550D) with open/close doors on four sides. This system is to be connected with a box-shaped chamber designed for nominal 550 mm wide substrates. Thanks to the openable doors, this chamber structure facilitates the cleaning of rollers, plate heaters and the like. The maximum diameter of mountable substrates is ϕ400 mm. The chamber is evacuated by a dry pump.

An indium tin oxide (ITO) film used for a touch panel requires an index matching (IM) film, an optical adjustment layer that compensates for the difference in optical characteristics so as to prevent so-called "skeleton emergence," the problem of ITO wiring patterns showing up after the patterning. Here, comparisons were made between ITO films deposited with and without degassing. The substrate material was LightNavi® CW1300L/NP-50, a 50 μm-thick PET substrate with an IM layer, available from NOF Corporation. Un-balanced magnetron sputtering (UBMS), having a high plasma-assist effect,[2] was performed to deposit ITO films having a thickness of 23 nm. Sheet resistance and total light transmittance were measured before and after annealing at 150 ℃ for 1 hour to evaluate the effect of degassing. The results are shown in **Table 2**. It was revealed that the degassing eliminates residual

Fig. 6 Degassing R2R model W35-550D

Table 2 Comparison of typical ITO-film characteristics with and without degassing treatment

Condition		Sheet resistance (Ω/sq)	Total light transmittance (%)
With degassing treatment	As deposited	464	86.5
	After annealed	151	89.0
Without degassing treatment	As deposited	567	87.7
	After annealed	683	88.6

moisture and oligomers in the substrate, which are factors that inhibit the crystallization of the ITO film during annealing treatment, and enables favorably low sheet resistance with a high transmittance.

Resin substrates incidentally contain moisture. This makes degassing treatment important for other applications. For example, when depositing an oxide film, SiOx, a large amount of released moisture disables the control of oxygen taken into the film and destabilizes the quality of the film. Hence, the degassing treatment prior to the vacuum coating is extremely important in order to maintain constant conditions of film deposition.

4. Application examples of large R2R sputtering system

A large R2R sputtering system has been described using the example of ITO film deposition on wide substrate. There are other cases where similar systems are used. The following introduces the application examples of metal film deposition (thin films for metal mesh, metal wiring films) used in touch panel and optical film deposition.

4.1 Metal film for touch panels

(1) Thin film for metal mesh

Large touch panels used for tablet terminal and digital displays must maintain transparency while keeping their sheet resistance as low as several tens Ω/sq or less. For large-screen applications of 15" or greater, however, the reduction of ITO film resistance is approaching the physical limit. Electronic information devices such as displays and tablet terminals are also required to be flexible. Thus ITO films, which are prone to crack during bending and folding, are required to be replaced by other transparent conductive films with flexibility.

To resolve the issues associated with ITO films, metal mesh films,[3] in which metal films with a thickness of several hundred nanometers are patterned into fine mesh, have been implemented as new transparent conductive films in the last several years. The methods of depositing these metal films include vacuum processes such as vapor deposition and sputtering, as well as printing processes such as gravure offset and ink jet. These processes have pros and cons in terms of the need for photolithography, workability of the mesh, selectivity of wiring materials and production cost.

Fig. 7 shows a multi-layer film used for typical metal mesh sputter-deposited on a PET film. An intermediate adhesion layer is provided between the PET film substrate and metal conductive layer so as to improve their adhesion and has a minimum required thickness of 10 nm or less. The material selected for the intermediate adhesion layer is commonly an oxidation-resistant alloy in the same alloy system as the metal conductive layer so as to prevent the diffusion of the metal conductive material into the PET film and to inhibit oxidation. The topmost black layer suppresses the optical reflection from the conductive layer surface to obscure the meshed wiring and to mute the color intrinsic to the metal conductive layer. Metal oxide and/or nitride is/are mainly used as the material. As in the case of the intermediate adhesion layer, the black layer is required to have adhesion to the conductive layer, mesh-patternability (etchability) as well as continuous patternability with the conductive layer. These factors are taken into account in selecting the material for the black layer.

Fig. 8 is a micrograph of a metal-mesh film. This metal-mesh film was made from a multi-layer film including a metal conductive layer, as shown in

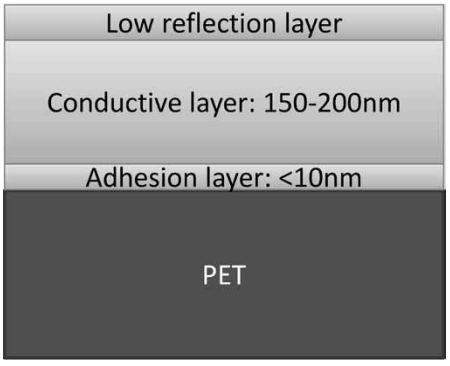

Fig. 7 Cross-sectional view of multi-layer thin film for metal mesh

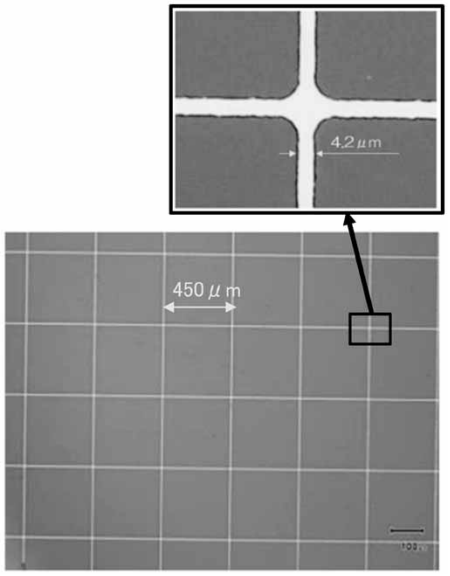

Fig. 8 Microscope photograph of Cu multi-layer after mesh patterning

Fig. 7, deposited on a PET substrate using the W35-350S system (the system details will be described later.) This multi-layer film was then patterned by photolithography. This sample includes a metal conductive layer of pure copper (tough pitch copper having a purity of 99.9% or higher), an intermediate adhesion layer of copper alloy and a black layer of copper alloy oxide. This photolithographic mesh pattern has a linewidth of 4.2 μm and line spacing of approximately 450 μm. The total light transmittance after the mesh patterning is 89.6%, satisfying the transparency required for touch panels.

(2) Metal film for wiring

Fig. 9 is a cross-sectional schematic drawing of a multi-layer film for wiring an electrostatic capacitance type touch panel. The multi-layer consists of, in sequence, a PET film substrate, an IM/ITO layer, an intermediate adhesion layer similar to the one used for the multi-layer film for metal mesh, and a metal conductive layer. The topmost protection layer serves to protect the metal conductive layer from oxidation, deterioration and fingerprints.

4.2 Optical film

Well-known examples of optical films include the films affixed to the glass windows of, for example, ordinary homes, office buildings and commercial facilities to improve interior air-conditioning efficiency and exterior appearance. Window films are heat reflective, transmitting visible light with a wavelength of 400 to 800 nm and reflecting light with wavelength of 800 nm or longer. These films are being widely used for the above purpose.

Fig.10 is a cross-sectional schematic drawing of a heat-reflecting film experimentally made by the W35-550S system (the system details will be described later) The W60 - 1600S, a large system with four coating zones, also has a to-and-fro deposition capability which enables the deposition

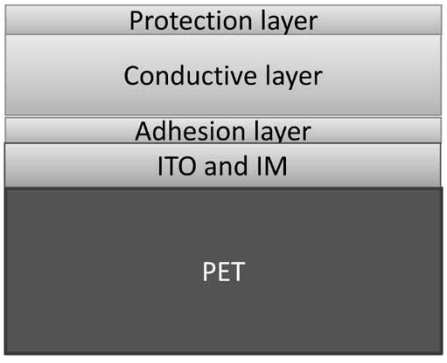

Fig. 9 Cross-sectional view of metal multi-layer on ITO for touch panel

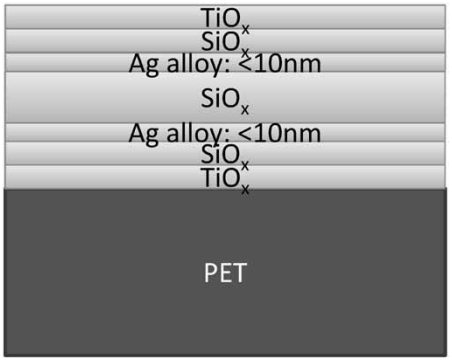

Fig.10 Cross-sectional view of heat reflective film

of this film structure. The multi-layer film comprises 7 layers of optically designed thin films deposited on a PET film substrate and includes a TiOx layer having a high refractivity, a SiOx layer having a low refractivity and a heat-reflecting layer of silver alloy. This arrangement is compatible with the total light transmittance for visible light of 67.8% and infrared light reflectivity of 68.2% (wavelength 1,100 nm.)

5. Lineup of R2R systems

5.1 Other large R2R systems

A degassing system, W30-1600D, dedicated to the R2R system, employs the span-heating method and accommodates the substrate width of 1,600 mm. This system is used for the pretreatment of sputter coating. Type W30 is designed conventionally, chambers being opened and closed, while the film transferring arrangement is fixed. This model is useful as an apparatus auxiliary to pre-existing systems whose productivity is bottlenecked by the degassing process and/or whose degassing function is relatively poor. The degassing zone has a length of approximately 4,000 mm. The apparatus accommodates substrate rolls of up to ϕ700 mm. **Fig.11** shows this degassing system.

A large chemical vapor deposition (CVD) system,[4] which is uniquely designed as a W60

Fig.11 Degassing R2R model W30-1600D

type by Kobe Steel, is also in the lineup. This is a coating system based on Kobe Steel's original method of coating SiOx. This system includes a pair of electrode rollers, which transfer resin substrates while depositing a dense film of SiOx by the mid-frequency (MF) magnetron discharge. The system has been applied to high-barrier films on resin substrates and low-refractive SiOx layers for the ITO films of touch panels. **Fig. 12** shows the W60-1300C.

5.2 Small R2R systems

A R2R sputtering system W35-S comprises a box-shaped chamber having a left door and a right door; a film transfer arrangement supported at its two ends by the front and rear walls of the box-shaped chamber; an anode layer source (ALS), a pretreatment source (optional) and a dual magnetron sputtering (DMS) source mounted on the left door; and a UBMS source mounted on the right door. The hinged door fully opens the chamber, making the system compact and allowing easy access to the coating zones. Here the type designation W35 indicates a R2R system having a box-shaped chamber with pivoting openable doors as described above.

Fig.13 shows the W35-350S system for a nominal 350 mm wide substrate with a door opened, while **Fig.14** shows the construction of the system. Opening the doors as shown in Fig.13 facilitates access to the sputtering source and to the coating masks, eases the loading of film substrates and collects all the work spaces in one spot. In conventional systems, the film transfer mechanisms are pulled out. The newly developed system eliminates the need for space to pull them out, which almost halves the installation footprint. Moreover, the film transfer rollers are supported at both ends, providing stability.

The W35 types can incorporate a CVD function in the lower part of the chamber. The CVD dedicated system is designated as W35-C, while the system combining CVD with sputtering is designated as W35-CS. The system can also incorporate various other functions. **Fig.15** shows an example in which an RM sputtering source (optional) is mounted

Fig.12 CVD R2R model W60-1300C

Fig.13 Sputtering R2R W35-350S model

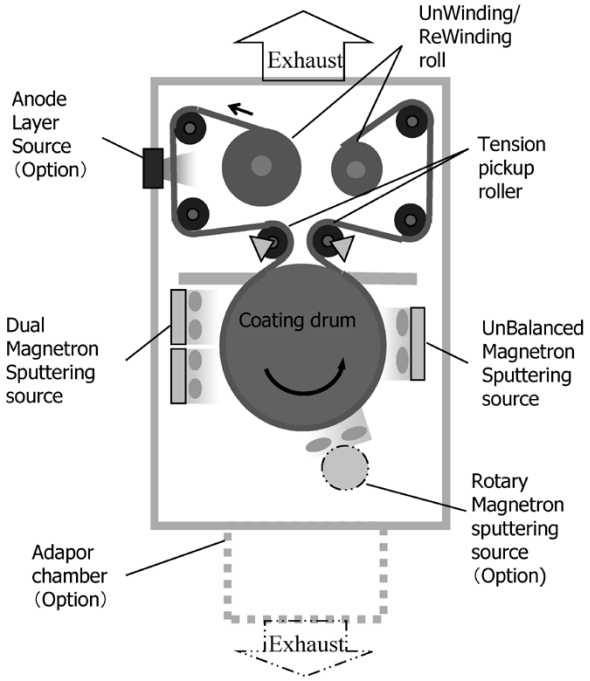

Fig.14 Schematic of sputtering R2R model W35-S system

Fig.15 Rotary magnetron sputter source in W35-550CS system

on the bottom of the chamber. The RM sputtering system employs a fixed magnet unit and a rotatable hollow cylindrical target. It has the advantage of a higher target utilization rate of about 80%, compared with 20 to 40% for the planar system. Kobe Steel adopted RM sputtering sources that are supported at both ends by the chamber interior walls.

This series has gained a fine reputation as small R2R systems and has been widely used, not only as experimental equipment, but also as production equipment for substrates that are 700 mm wide or narrower. The equipment lineup also includes the W40 types in which the coating zones of the W35 type are separated by a bulkhead structure and differential evacuation. Kobe Steel owns a system combining sputtering with CVD, W35-350CS and W35-550CS, which it exploits for various sorts of development and sample tests.

Conclusions

The R2R systems of Kobe Steel feature a unique structure to improve accessibility to various processing zones for facilitating cleaning and the changing over of shields/masks to stabilize product quality. The newly developed model of the large R2R sputtering system comprises unit chambers that can be connected horizontally so as to improve expandability, dismountability and mountability, enabling a quick response to the rapidly changing market. The system lineup is being expanded. Kobe Steel will strive to respond to customers' needs by integrating various technologies developed by the machinery business division and corporate research laboratories.

References

1) H. Tamagaki et al. *R&D Kobe Steel Engineering Reports*. 2008, Vol.58, No.2, pp.42-46.
2) Y. Kurokawa et al. *R&D Kobe Steel Engineering Reports*. 2002, Vol.52, No.2, pp.31-34.
3) Y. Ukai. *Electronic Journal*. March 2014, pp.56-57.
4) H. Tamagaki et al. "Transparent High Barrier Coating on Polymer Web by PE-CVD Roll Coater", *53th Annual Technical Conference Proceeding of the Society of Vacuum Coater*, 2010, pp.553-557.

Amorphous Oxide Semiconductor Adopting Back-channel-etch Type Thin-film Transistor

Shinya MORITA*1, Mototaka OCHI*1, Dr. Toshihiro KUGIMIYA*1
*1 Electronics Research Laboratory, Technical Development Group

Kobe Steel has developed a new amorphous oxide semiconducting material available for the back-channel-etch (BCE) type thin-film transistor (TFT) adapting mass production of flat panel displays. The material has high chemical resistivity for the conventional etchant of Mo/Al source and drain interconnection. It has been shown that good electrical characteristics and high reliability in BCE-TFT can be obtained by means of the additional annealing process to repair back-channel damage on the oxide semiconductor thin film.

Introduction

Lately, the performance of flat panel displays (FPDs), such as liquid-crystal displays (LCDs) and organic light-emitting displays (OLEDs), is being upgraded in terms of, for example, increased screen size, higher driving speed and elevated definition as seen in 4 k and 8 k displays. Hence thin-film transistors (TFTs), switching elements that drive picture elements, are required to be driven at higher speed under higher current. Accordingly, semiconductor thin film, the heart of a TFT, must be made of a semiconductor material with high electron mobility.

Amorphous oxide semiconductor materials,[1), 2)] as typified by indium gallium zinc oxide (In-Ga-Zn-O, IGZO),[3)] have electron mobility, an index showing how easily the electrons can move, more than ten times faster than those in conventional materials; and they can be deposited on substrates with large areas. Thus they are gathering attention as semiconductor material for next-generation displays. Oxide semiconductors, however, are sensitive to the external environment. This makes it important to have stable control of the TFT manufacturing process in mass production.

Against this background and to improve productivity, Kobe Steel has developed a new oxide semiconductor material, KOS-B02, which has an electrical performance equal to that of IGZO and superior chemical stability. This material was adapted for back-channel-etch TFT (BCE-TFT), which is more suitable for mass production. The production process was optimized, which resulted in favorable electrical characteristics and high reliability, as reported in this paper.

1. Issues with oxide semiconductor materials for FPD

Thin-film-transistor (TFT) elements are switching elements that switch the picture elements of LCDs and OLEDs. Each display may contain more than a million TFT elements. In the case of LCDs, each drain electrode is connected to its own picture-element electrode that supplies voltage to liquid-crystal molecules. The semiconductor thin film plays an important role in controlling the current between drains and sources.

Hydrogenated amorphous silicon (a-Si: H) has hitherto been used for the material for semiconductor thin film; however, performance improvement, such as increased screen size, higher driving speed and elevated definition, requires material with higher carrier mobility (hereinafter simply referred to as "mobility".) Hydrogenated amorphous silicon has mobility that is insufficient for next-generation 4 k/8 k displays and OLED applications. There is a need for semiconductor material with greater mobility.

Table 1 compares the features of various semiconductor materials used for displays. Low temperature polycrystalline silicon (LTPS) and amorphous oxide semiconductors, each having mobility higher than that of a-Si: H, are used for high-spec applications.[4)] Low temperature polycrystalline silicon exhibits the greatest mobility; however, there are problems in that its crystallization requires laser annealing, making it inapplicable to large areas, and its production cost is high. Oxide semiconductors, on the other hand, can easily be deposited on large areas by sputtering and are superior in productivity because the TFT production process, similar to the one based on conventional a-Si: H, can be used. Moreover, oxide semiconductors exhibit a little leak current, an advantageous feature for decreasing power

Table 1 Semiconductor materials used in flat panel display

	a-Si:H	LTPS	Oxide
material	Si	Si	IGZO, ZnO, ZTO, etc.
mobility(cm^2/Vs)	1<	50-100	1-30
TFT uniformity	Good	Poor	Good
TFT reliability	Poor	Good	Good
Process temperature	150-350°C	250-550°C	RT-400°C
Substrate	LCD	LCD OLED(small size)	LCD, OLED, E-paper

consumption, and are well suited for smartphone displays. As described, oxide semiconductors can achieve high performance, but their yield and productivity must be improved before they are used widely.

2. TFT structure and production process

To decrease the production cost, TFTs must have simplified structures so as to reduce the number of process steps. **Fig. 1** shows the structures of two typical types of TFT elements, each having a gate electrode on its substrate. The etch-stop (ES) type, shown in Fig. 1(a), has its semiconductor thin-film surface protected by an etch-stop layer (ESL) and achieves excellent reliability. The back-channel-etch (BCE) type, shown in Fig. 1(b), has no etch-stop layer, which requires fewer photo-patterning steps than the ES type; a feature more advantageous as regards the production cost.[5] In addition, it allows the use of the conventional process of a-Si: H-TFTs. Hence there are many manufacturers adopting the BCE type. In addition to the cost reduction, the BCE type can adopt a shorter channel length (L in the figure), which makes the downsizing of TFTs easier and has the advantage of permitting the parasitic capacitance, a cause of signal delay, to be made smaller.

The BCE type, on the other hand, is more susceptible to defects and contamination on the surface of the semiconductor thin film (back-channel) and requires highly sophisticated process control. Furthermore, during the patterning of the source and drain electrodes, the semiconductor thin film is exposed to the etchant, such as acid, which may reduce the thickness of the semiconductor thin film, thus posing a problem. Such etching damage may cause problems of deteriorated TFT characteristics and decreased reliability, often rendering the TFT elements impossible to make.[6), 7)]

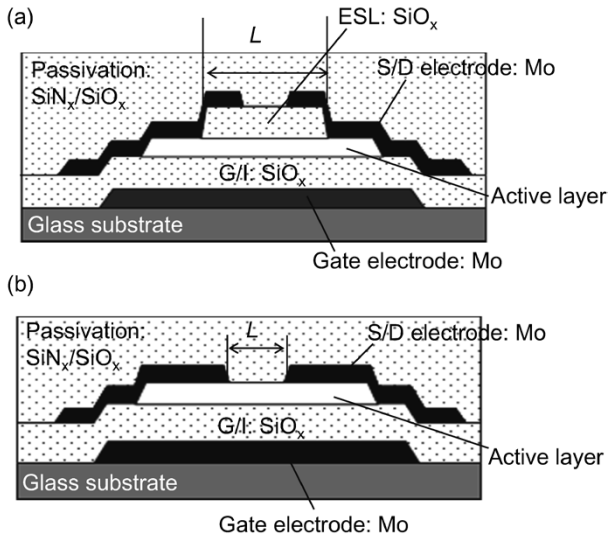

Fig. 1 Schematic of (a) ES-type, and (b) BCE-type TFTs

3. New oxide semiconductor material compatible with BCE type TFT

Oxide semiconductor thin films must have increased resistance against acid etchant to be compatible with the manufacturing process of BCE type TFTs, the process with a low production cost. Hence Kobe Steel revised the compositions of oxide semiconductors and has developed a material having both electrical characteristics comparable to those of IGZO and excellent acid resistance.

Among the constituents of IGZO, In is considered to improve conductivity, Ga decreases oxygen deficiency, and Zn stabilizes the amorphous structure.[8] In addition to these constituents, an addition of new elements was devised to achieve both the desired electrical characteristics and acid resistance.

In general, impurity elements in a semiconductor cause the carrier to be scattered, decreasing electron mobility. **Fig. 2** shows the results of a study on the field effect mobility of TFTs based on IGZO with addition of various elements. Most elements decrease the mobility to a greater or lesser extent. The results show that tin (Sn), even added in the amount of approximately 10 at%, exhibits no decrease in the mobility, implying no degradation in the electrical characteristics of IGZO thin film. This is attributable to the fact that, as is the case of In, Sn has a large ion radius and forms conductive oxide with less electron scattering. Moreover, SnO_2 is acid-insoluble with high chemical resistance and is effective in improving acid resistance.

With this in mind, Sn was selected as the fifth element to be included in IGZO. The composition of In, Ga, Zn and Sn was optimized to simultaneously achieve field effect mobility, reliability and acid

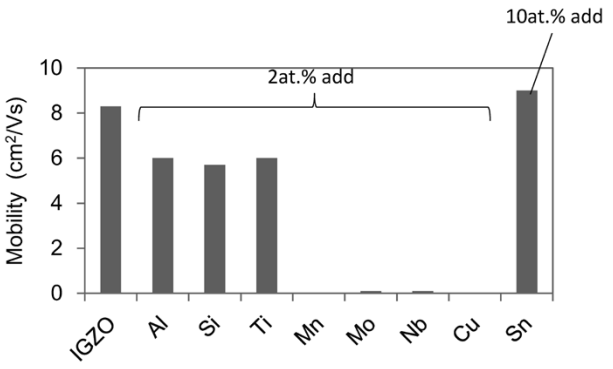

Fig. 2 Field effective mobility of IGZO-TFT with additional element

resistance. As a result, a new amorphous oxide semiconductor, KOS-B02, was developed, which is compatible with the production process of BCE type TFTs.[5), 6)] The manufacturability of a sputtering target with the proposed composition and sufficiently high density and quality was confirmed. A prototype sputtering target was prepared by Kobelco Research Institute, Inc., and the target was subjected to a trial production of TFTs and thin-film evaluation, as described in the following sections.

4. Characteristics of newly developed oxide semiconductor thin film

4.1 Comparison of basic characteristics

Table 2 compares the physical properties (carrier concentration, hole mobility, bandgap), sputtering rate and etching rate for the acid etchant of the newly developed KOS-B02 thin film with those of IGZO. The carrier concentration of $1.0 \times 10^{16}/cm^3$ is in the standard range of carrier concentration for oxide semiconductor, and both the hole mobility and bandgap have values similar to those of IGZO. The sputtering rate is higher than that of IGZO by almost 20%, indicating superior productivity.

The etching rate for acid etchant was measured using PAN etchant (a mixture of phosphoric acid, nitric acid and acetic acid) commonly used for the fabrication of source/drain electrodes. The etching rate of molybdenum (Mo) thin film, used for source/drain electrodes, is 83 Å/s and that of a-IGZO is about a quarter of that value. In general, the thickness of semiconductor thin film used for TFT is around 40 nm, which is much thinner than that of the source/drain electrodes (300-500 nm.) Thus there is a concern that the semiconductor thin film might be significantly removed during the fabrication of source/drain electrodes in the TFT manufacturing. It is noteworthy that KOS-B02 thin film is insoluble to PAN etchant, exhibiting no reduction in film thickness during immersion. Hence, this indicates that this semiconductor thin film will exhibit almost no thickness reduction during the TFT manufacturing process and is applicable to BCE type TFTs with a low production cost.

Table 2 Comparison of IGZO and KOS-B02 thin film

	IGZO	KOS-B02
Carrier concentration (1/cm^3)	4.0×10^{16}	1.0×10^{16}
Hall mobility (cm^2/Vs)	11.6	15.1
Photonic band gap (eV)	3.15	3.08
deposition rate ratio (IGZO : 1)	1	1.19
Etching rate for PAN (Å / sec)	20	0

4.2 Prototype evaluation of BCE type TFT

The characteristics of display TFTs are significantly affected not only by the semiconductor thin film alone, but also by the production process of the TFTs. In an attempt to confirm the performance in a real TFT, a prototype TFT based on KOS-B02 was prepared by the process commonly used for BCE type TFTs and was evaluated.

Fig. 3 illustrates the process used in the preparation of the prototype BCE type TFTs. The TFT comprises a gate electrode of Mo thin film deposited on a glass substrate and a gate insulation layer of SiOx deposited by plasma CVD (Fig. 3(a).) A semiconductor (IGZO or KOS-B02) thin film, 40 nm thick, was deposited and patterned on top by magnetron DC sputtering, and this laminate was then heat-treated in the atmosphere at 350℃ for 1 hour to improve the film quality (Fig. 3(b).) Subsequently, source/drain electrodes (Mo thin film) were deposited, and the resulting laminate was subjected to wet etching using PAN etchant to fabricate source/drain electrodes (Fig. 3(c, d).)

Then, passivation layers of SiOx and SiNx were deposited in sequence to protect the TFT element

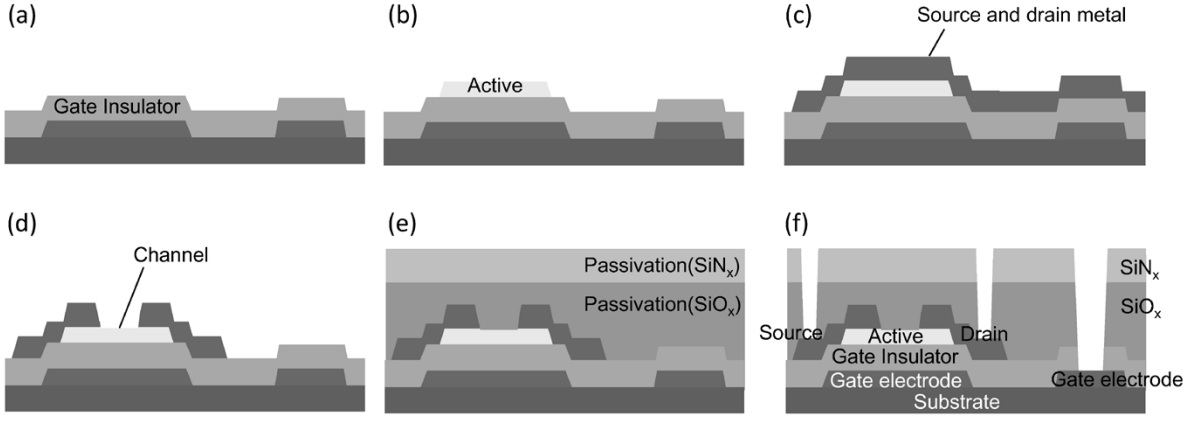

Fig. 3 Process flow of BCE-TFT

(Fig. 3(e)). Finally, annealing was applied for characteristics improvement before the completion (Fig. 3(f)).

4.3 Static characteristics of TFT

Fig. 4 includes cross-sectional photos taken at the edges of the drain electrodes of the TFT samples prepared. Fig. 4(a) shows IGZO with its thickness decreasing as the distance from the electrode increases. This thickness distribution of the semiconductor film causes distribution in the electric field, which can adversely affect the switching characteristics of TFTs. In the case of KOS-B02 (Fig. 4(b)), on the other hand, the oxide semiconductor thin film exhibits no reduction of thickness, indicating almost no removal of the semiconductor thin film by the etchant.

Fig. 5 depicts the switching characteristics (I_d-V_g characteristics) of the TFTs prepared. The drain current was measured at a drain voltage of 10 V while applying voltages of -30 to 30 V to each gate electrode. The drain current begins to increase at a voltage close to 0 V, showing switching from OFF to ON. The KOS-B02 shows favorable characteristics with a steep rise of its drain current, while IGZO exhibits a gradual rise as well as low drain current. The current-voltage characteristics (I_d-V_g characteristics) in the saturation region are given by the following:

$$I_d = \frac{\mu_{FE} W C_i}{2L} (V_g - V_{th})^2$$

W; channel width:
C_i; gate insulation film capacitance
L; channel length V_{th}; TFT threshold voltage

The field effect mobility, μ_{FE}, was calculated on the basis of the switching characteristics shown in Fig. 5, yielding 5.4 cm²/Vs and 7.9 cm²/Vs for IGZO and KOS-B02 respectively, with the latter showing higher mobility. Moreover, S values, representing the steepness of the rise in drain current (i.e., the minimum gate voltage required to increase the current by an order of magnitude) were 0.84 V/decade and 0.22 V/decade respectively, demonstrating the superiority of KOS-B02. The difference in the characteristics of the two materials is considered to be attributable to the etching, as described, of the semiconductor thin film during the fabrication of source/drain electrodes. Due to the reduced film thickness, the IGZO is considered to have deteriorated switching characteristics. The KOS-B02, on the other hand, exhibits excellent switching characteristics despite the damage caused by the etchant on the back-channel surface.

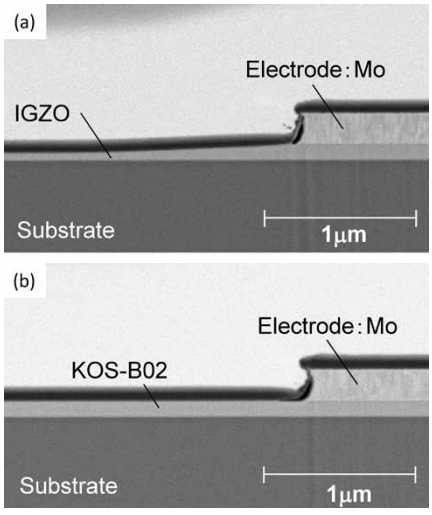

Fig. 4 Cross section SEM image of (a) Mo/IGZO and (b) Mo/KOS-B02 stacked film

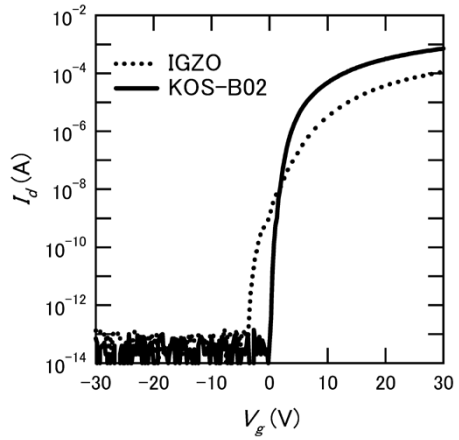

Fig. 5 I_d-V_g characteristics of BCE-TFT using IGZO and KOS-B02 thin film

4.4 Reliability of TFT

During operation, TFTs are subject to various external factors (stress). A large number of defects in semiconductor thin films and/or in interfaces cause changes in characteristics, such as a shift in TFT threshold voltages.[9] Such changes can cause uneven colors and lighting failure. Hence an accelerated test was conducted to confirm the variation in TFT characteristics.

Figs. 6(a) to 6(c) respectively show the measured characteristics of positive bias-temperature stress (PBTS), negative bias temperature instability (NBTS) and light negative bias-temperature stress (LNBTS). The measurement conditions are listed in **Table 3**. Each measurement was conducted after applying respective stress for a predetermined time period (0 s, 300 s, 1,000 s, 3,600 s, and 7,200 s.) Applying a bias to the gate electrode of a TFT causes electrons and holes to be trapped in the semiconductor thin film and interfaces, shifting the threshold voltage

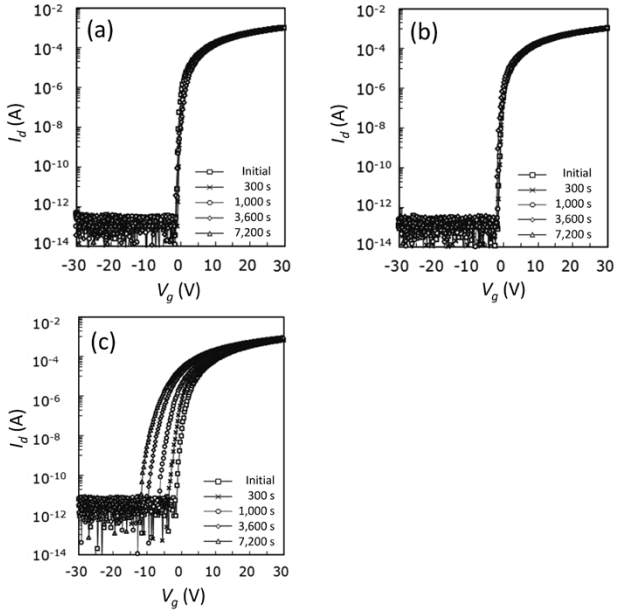

Fig. 6 Stress test results of BCE-TFT using KOS-B02 thin film (a) PBTS, (b) NBTS, (c) LNBTS

Table 3 Stress test conditions of TFT

	Vg (V)	Vs (V)	Vd (V)	T(℃)	Light	Time(s)
PBTS	20	0	0.1	60	-	0～7,200
NBTS	-20	0	10	60	-	0～7,200
LNBTS	-20	0	10	60	White LED 25,000 nit	0～7,200

in the positive or negative direction. As shown in Figs. 6(a) and 6(b), the switching characteristics remain almost unchanged for the PBTS and NBTS, indicating excellent stability against these stresses.

The LNBTS, however, caused the threshold voltage to shift toward negative as time elapsed: a shift of 9.8 V in 2 hours. The LNBTS is the most important stress test for liquid-crystal displays. As a rough indication, a shift of less than 2 to 3 V in 2 hours is regarded as acceptable. Hence the characteristics shown in Fig. 6(c) are considered to be inapplicable to LCD drivers.

The shift of threshold voltage under LNBTS is considered to be caused by electrons and holes that are newly created by photons and are trapped in the semiconductor thin film and interfaces. Multiple defect levels in a semiconductor thin film give rise to light-induced positive holes. When trapped, these positive holes create a fixed charge, facilitating the shift in threshold voltage.[10), 11)] When used for the ES type TFT, KOS-B02 exhibits no deterioration due to LNBTS. Hence the shift found in BCE-TFT is considered to be attributable to the deterioration of, or damage to, the back-channel.

5. Improvement in the BCE type TFT production process

5.1 Surface analysis of oxide semiconductor thin films

X-ray photoelectron spectroscopy (XPS) was performed to study how the etchant alters the surface of KOS-B02 thin film.

Fig. 7 shows the depth profiles of O1s spectrum in KOS-B02 thin film. The measurement in the depth direction was conducted while sputtering the thin film surface. Fig. 7(a) depicts the profiles measured on a sample without dipping in etchant, showing the O1s peak position remaining unchanged at 531.0 eV for the outermost and interior surfaces. Meanwhile, as shown in Fig. 7(b), the sample dipped in PAN etchant exhibits a peak position at 531.0 eV for the interior surface and a peak position at 531.8 eV for the outermost surface, a peak shift toward higher energy. The O1s peak energy depends on the bonding state of oxygen and takes a value of 530.5 eV for no oxygen deficiency and 532.5 eV for oxygen deficiencies.[12)] This implies that the dip in the etchant caused the oxygen deficiencies to increase. Oxygen deficiencies are considered to be the cause of

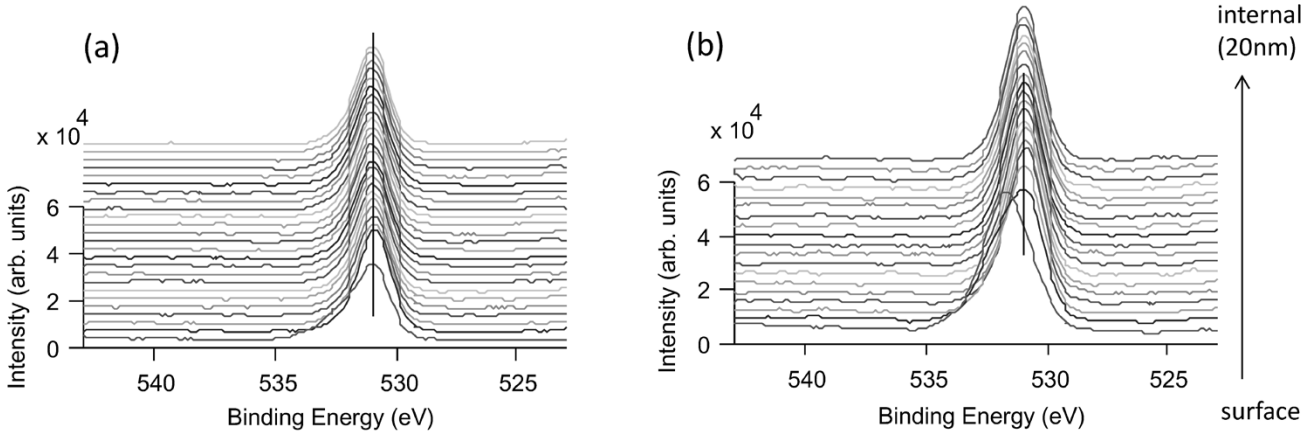

Fig. 7 Depth profile of O1s spectrum in KOS-B02 thin film; (a) without dip in etchant, (b) with dip in etchant

the deterioration due to optical-light stress.

5.2 Treatment to repair surface damage

To achieve favorable TFT characteristics, it is important to repair the surface damage caused by etchant. So, a study was conducted on an additional annealing in oxidation atmosphere (air) so as recover surface oxygen deficiency in the production process of BCE type TFTs. When TFTs are exposed to annealing atmosphere, the electrodes may be oxidized, causing the film to peel and/or the TFT characteristics to deteriorate. Therefore, the decision was made to apply annealing in addition to the process described above, after depositing the passivation layer of SiOx.

Fig. 8 shows the relationship between the annealing temperature and resistivity of KOS-B02 thin film. The specimen was a laminate having the same structure as the TFT, and the resistivity was measured by the van der Pauw method.[13] The resistivity intrinsic to KOS-B02 thin film was approximately 10 kΩcm. In contrast, dipping in PAN etchant decreased the resistivity to about 10 Ωcm. When the additional annealing was applied after the deposition of the SiOx passivation layer, the resistivity increased up to the annealing temperature of 400℃ and decreased at higher temperatures. The resistivity became closest to that intrinsic to KOS-B02 thin film at the annealing temperature of 300℃. The film quality is considered to become most stable at this temperature. Thus the annealing temperature was set at 300℃.

5.3 Verification on the effect of recovery annealing

A sample of BCE type TFT additionally heat-treated at 300℃ after depositing SiOx passivation thin film was evaluated for reliability under LNBTS. As shown in **Fig. 9**, almost no variation of threshold voltage was observed in the period of 0 - 7,200 s during which the stress was applied, indicating that the sample had a high reliability, unlike the TFT without additional annealing shown in Fig. 6(c). Reliability against LNBTS is known to strongly depend on the oxygen deficiency in oxide semiconductor thin films. The recovery of reliability is considered to be the result of the annealing having restored the surface, damaged as described, of the oxide semiconductor thin film.

5.4 Defect-restoration mechanism of recovery annealing

The condition of the oxide semiconductor thin film before and after annealing was studied. A sample element with the same structure and substrate as the TFT element was prepared and subjected to secondary ion mass spectroscopy (SIMS) to analyze the depth profile of O^- and OH^- ions (**Figs.10**(a), (b)). Both Figs. 10(a) and 10(b) exhibit high-intensity regions around the depth of 350 nm to 400 nm in the oxide semiconductor thin film. O^- ions were compared before and after annealing, and found to remain almost unchanged by the annealing, while OH^- ions exhibit a difference in the profile inside the semiconductor thin film. The annealing increased OH^- on the surface side, making OH^- ions more uniformly distributed. It is believed that OH^- ions terminate the generation of oxygen deficiencies around metal elements,[14] which implies that the semiconductor thin-film surface, having many defects, is oxidized by the annealing, while being protected by OH^- ions. The additional annealing thus serves to repair defects created in the backchannel during the making of BCE type TFTs,

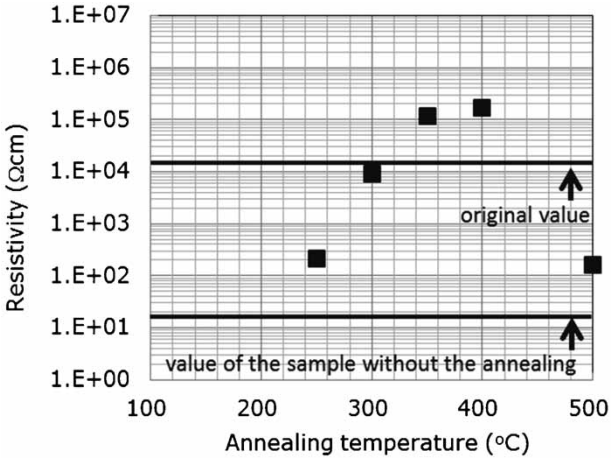

Fig. 8 Relationship between annealing temperature and electric resistivity of KOS-B02 thin film

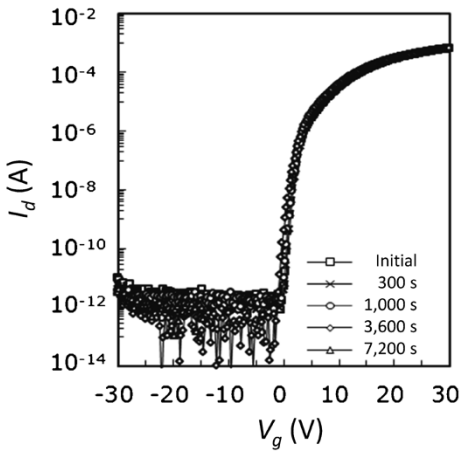

Fig. 9 Results of LNBTS for BCE-TFT using additional annealing

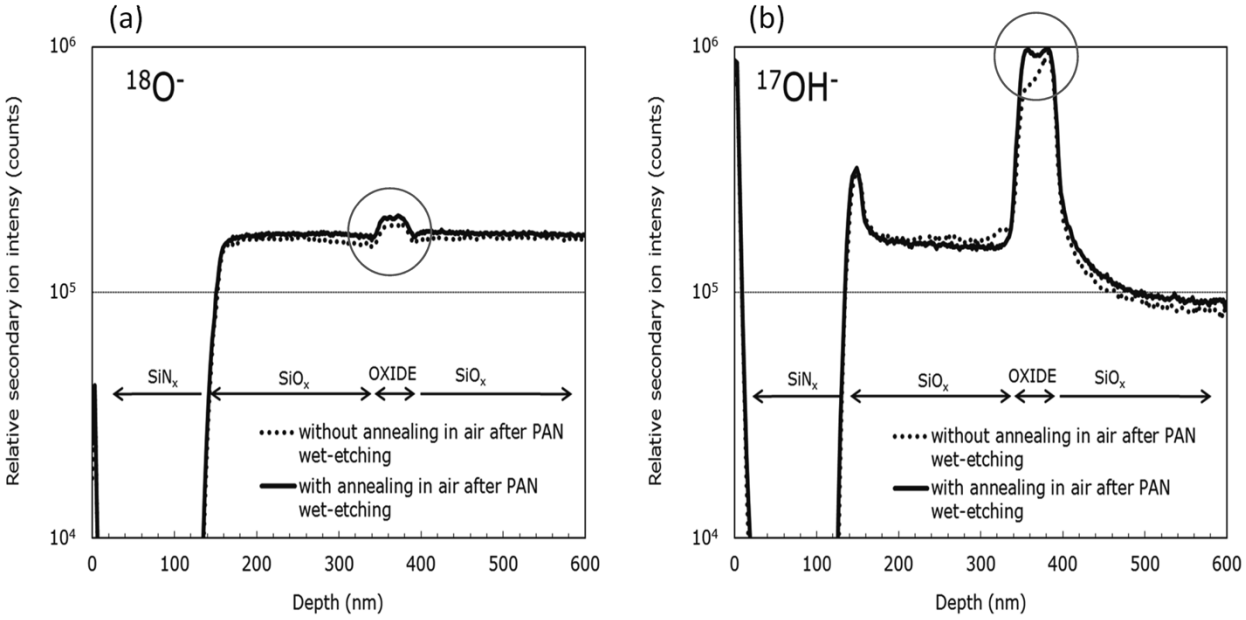

Fig.10 Ten-Depth profile of (a) O ion and (b) OH ion of BCE-TFT

by oxidation and OH termination, which realizes TFTs with high reliability. As described, KOS-B02 has been proved to be applicable to BCE type TFTs, whose production cost can more easily be reduced, and this enables the production of TFTs with excellent electrical characteristics and reliability.

Conclusions

An oxide semiconductor material, KOS-B02, which can realize both high productivity and mobility, has been developed for FPDs. The following characteristics have been confirmed:

1) The material composition of IGZO was revised in order to develop an oxide semiconductor material having high chemical stability, being almost insoluble to the PAN etchant commonly used in the fabrication of source/drain electrodes. The newly developed material is applicable to BCE type TFTs, which are low in manufacturing cost and more suited to volume production. This is expected to reduce the manufacturing cost of FPDs.
2) Regarding the use of the KOS-B02 in BCE type TFTs, adapting an annealing process that recovers back-channel damage allows the achievement of both excellent electrical characteristics and reliability.

References

1) J. I. Song et al. *Appl. Phys. Lett*. 2007, Vol.90, p022106.
2) P. Gorm et al. *Appl. Phys. Lett*. 2007, Vol.90, p063502.
3) K. Nomura et al. *Nature*. 2004, Vol.432, p.488.
4) J. K. Jeong. *2nd Oxide TFT Workshop*. 2007.
5) S. H. Ryu et al. *ECS Solid. State. Lett*. 2012, Vol.1, Q17.
6) S. Morita et al. *Proc. IDW'12*. 2012, p.883.
7) M. Ochi et al. *Proc. IDW'13*. 2013, p.371.
8) T. Kamiya et al. *OPTRONICS*. Vol.274, 2004, p.128.
9) J. Song et al. *SID 2013. DIGESTS*, p.93.
10) K. H. Ji et al. *Appl. Phys. Lett*. 2011, Vol.98, p.103509.
11) Y. Kim et al. *IEEE. Tra. Ele. Dev*. 2012, Vol.59, No.10.
12) G. H. Kim et al. *Phys. Status. Solid A*. 2007, Vol.207, p.1677.
13) K. Shono. *HANDOTAI GIJUTSU -JO*. University of Tokyo Press, 1980, pp.100-108.
14) Y. S. Lim et al. *Appl. Phys. Lett*. 2013, Vol.102, p.143503.

Site Flatness Measurement System with Accuracy of Sub-nanometer Order for Silicon Wafer

Kazuhiko TAHARA*1, Hideki MATSUOKA*1, Noritaka MORIOKA*1, Masato KANNAKA*2

*1 Technical Engineering Dept., LEO Business, Kobelco Research Institute, Inc.
*2 Production Systems Research Laboratory, Technical Development Group

A new system using a heterodyne interferometer has been developed to measure site flatness with an accuracy of sub-nanometer order for 300 and 450 mm wafers. This system is based on a spiral scan method, which enables the measurement of global flatness and site flatness. It is also possible to measure SFQR and ESFQR with 0.5 nm (σ) repeatability in an environment with as much as 5 Gal of floor vibration. This paper outlines the system and describes the experimental results for repeatability concerning global flatness and site flatness. Actual measurements turned out a GBIR of 0.68 nm (σ), SFQR of 0.33 nm (σ) and ESFQR of 0.39 nm (σ). Next, referring to the results of the measurement of actual wafers, it explains how this new system is effective in managing the process.

Introduction

The structures of silicon semiconductor devices are being miniaturized, allowing only small process margins for lithography. In lithography processes, focusing is conducted per each site within the surface of a chucked wafer, involving tilting to make each focal plane perpendicular to the optical axis. A wafer having a site thickness with variations greater than the focal depth of the optical system can cause failure attributable to defocusing. The local flatness of each site is referred to as "site flatness" and must have a dimension at the same level as the minimum working size of devices. The minimum working size has currently become 25 nm and has been refined at a pace of approximately 5 nm per year. There are trial manufacturing lines being planned for a line width of ten-odd nanometers, which has led to the need for an system that can measure site flatness with an accuracy in the order of sub-nanometers.[1)]

In general, shape measurement systems with sub-nanometer accuracies are subject to various disturbances, such as environmental vibrations, and can only be installed at limited locations. Flatness-inspection processes and facilities, on the other hand, require a system that enables measurement with high accuracy without preparing a special environment.

Regarding the size of wafers, φ300 mm wafers are mainly being used, and production processes for φ450 mm wafers are being studied.

Recognizing the rising interest in highly accurate site-flatness inspection, Kobelco Research Institute, Inc. and Kobe Steel have developed a system (hereinafter, "the present system") for measuring site flatness with an accuracy of sub-nanometer order (**Fig. 1**[2)]). The present system has improved vibration resistance and is designed for 300 mm and 450 mm silicon wafers after mirror surface polishing. This paper first summarizes the site flatness, then outlines the present system and finally describes actual measurement.

1. Indices of flatness

The indices of flatness include global flatness and site flatness (**Fig. 2**[3)]). Global flatness is typically represented by the global backside ideal range

Fig. 1 LSW-3010FE (Site flatness measurement system with an accuracy of sub-nanometer order for silicon wafer)[2)]

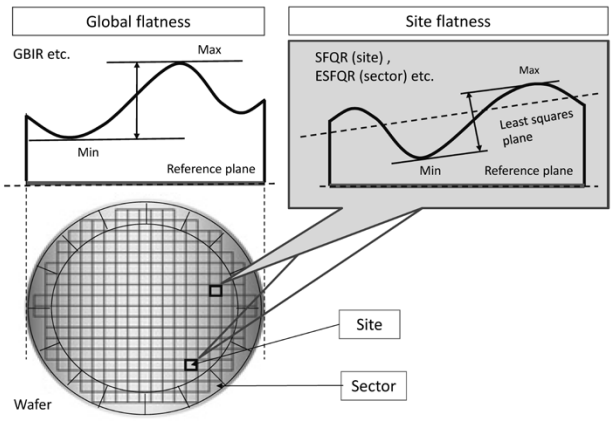

Fig. 2 Definition of GBIR, SFQR, ESFQR[3)]

(GBIR), which evaluates the thickness variation of an entire wafer. The GBIR is defined by the difference between the maximum and minimum values of thickness distribution. Site flatness, on the other hand, is typically represented by the site front least-squares range (SFQR) and edge site front least-squares range (ESFQR.) In SFQR, the entire surface of a wafer is separated into sites, each corresponding to an IC chip, and thickness variation is measured within each of these sites. The ESFQR evaluates the areas along the edge of a wafer where flatness tends to deteriorate compared with the inner wafer surface. The belt-like circumferential zone of a wafer is separated into equally-spaced sectors (as shown in Fig. 2) and the thickness variation in each sector is measured. The SFQR and ESFQR are each defined by the difference of maximum and minimum values that are determined from the distance from the reference plane that is obtained by the least-square method from the thickness distribution for the respective sector.

These indices are provided as indicators that affect the yield of the lithography process and are used also in the specifications for wafer trading. Hence, these indices, and their inspection accuracy as well, are regarded as important by wafer manufacturers and device manufacturers.

2. Measurement system

2.1 Measurement principle and advantage

Non-contact flatness measurement is usually conducted by means of electrostatic capacity, optical interference, triangulation, etc. The electrostatic capacity method, in particular, allows measurements of wafers with rough surfaces. Having an accuracy of several tens to a hundred nanometers depending on the objective distance and measurement range, it has been widely used in flatness inspection systems.[4] To achieve measurement with accuracy better than several ten nanometers, optical interferometry involving, for example, Fizeau interferometers and oblique-incidence interferometers, is generally used. Although these methods are applicable only to certain surface conditions of measured objects, they have the advantage of high accuracy. With the aim of achieving reproducibility in the order of sub-nanometers, the present system adapts the heterodyne interference method, in which shapes are measured by an optical probe. The following describes the measurement principle:

A wafer is rotated in the horizontal plane in the gap between a pair of sensor heads (optical probe), vertically disposed face to face with each other. The wafer is also moved in a linear direction such that the scanning is performed in a spiral motion. The wafer is edge-supported on a stage that can both rotate and move linearly, which governs the motion of the wafer (**Fig. 3**). During scanning, the apparatus measures the in-plane displacement change between the upper sensor head and the front surface of the wafer (ΔD_F; reference being made to the starting point of the measurement). Also measured is the displacement change between the lower sensor head and the back surface of the wafer (ΔD_B). Since the sensor heads are spaced at a constant distance, adding the changes of displacement measured by the two sensor heads enables the calculation of thickness variation (ΔT) in the plane.

The measuring principle of a displacement meter based on heterodyne interferometry (hereinafter, "heterodyne interferometer") is shown in **Fig. 4**. In the laser source, a laser beam is split into two laser beams, one modulated to a frequency of f and the other modulated to $f + \Delta f$, which are individually guided to the sensor heads. The two laser beams are incident on both the measurement surface of

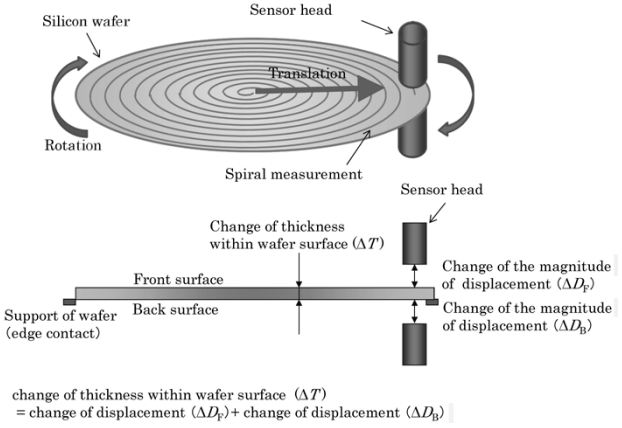

Fig. 3 Schematic of measurement part

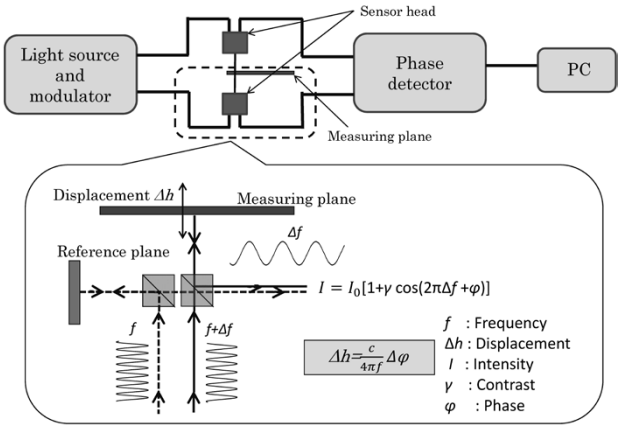

Fig. 4 Measuring method

the wafer and the reference surface contained in the sensor heads, and the reflected light is guided into the phase detector via optical fibers. The composite intensity of the two reflected light is brightness modulated by a modulated beat frequency of Δf to turn into interference signal I expressed by Equation (1):

$$I = I_0 \left[1 + \gamma \cos(2\pi \Delta f t + \varphi)\right] \quad \cdots\cdots (1)$$

wherein I_0, intensity sum of the two light; γ, contrast; φ, phase of combined light; and t, time. The phase of the interference signal is determined by the distance between the measurement surface and reference surface, and the relation between the amount of displacement variation on the measurement surface and the phase difference is given by Equation (2):

$$\Delta h = \frac{c}{4\pi f} \Delta \varphi \quad \cdots\cdots (2)$$

wherein: Δh, displacement variation; $\Delta \varphi$, phase difference: c: light speed. The amount of displacement variation at the measurement surface is given by detecting the phase difference $\Delta \varphi$, and calculating Equation (2). A heterodyne interferometer measures the phase change of interfering light and, hence, has the advantage of being immune to the change in light intensity in principle.[5)]

In addition, the heterodyne interferometer of the present system comprises one laser source for both the upper and lower sensor heads, as well as a common path, such that the drift caused by the change in ambient temperature is suppressed. Also, a polarization-maintaining optical fiber was adapted for the optical transfer between the units such that the interference signals are not affected by light phase and polarization disturbed by the pressure and/or vibration applied to the optical fiber itself. A simulation analysis was conducted on the structure of the sensor heads and their supports so as to minimize the measurement errors caused by the vibrations of the drive unit and floor. The results were reflected in the design. Furthermore, the effect of sound on the measured values was evaluated experimentally for the selection of the cover material and shape of the sensor heads. Various measures were thus taken to make the system immune to any conceivable disturbances, such as temperature change, vibration and sound.

2.2 Structure of flatness measurement unit

In a thickness measurement system having a pair of facing probes, the change in the spacing between the probes can become an error factor in the measured values. Hence, in addition to suppressing vibrations caused by the drive unit and other external factors, the system must have a structure with a minimum deformation due to the gravity-center shift of the stage. **Fig. 5** shows the construction of the present system. The rotary stage is driven by a hollow motor with air bearing, while the linear stage is driven by a linear motor with air sliders, to minimize the vibration of the stages during operation. The base and sensor holders included in the measurement unit are made of granite, which provides excellent vibration damping and has a small coefficient of thermal expansion, so as to suppress the infinitesimal deformation of the structure due to vibration and thermal expansion. In general, vibration absorbers based on air springs are often used for removing vibration from the floor. These absorbers, however, usually have a resonance region in the several Hz range, which may change the alignment of the system. Hence the present system comprises an active vibration isolator, which detects vibration and change in the alignment to perform feedback control, and successfully suppresses the low-frequency resonance and alignment change.

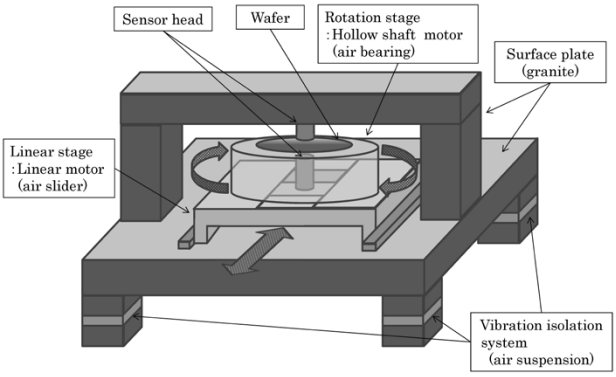

Fig. 5 Measurement system composition

The upper and lower sensors may be misaligned, due to the alignment error and temperature change, causing errors in the thickness values measured, as well as system differences and the long-term fluctuation of measured values. In order to adjust the sensor positions, a biaxial linear-moving horizontal stage, along with an algorism for the automatic control, has been developed. Periodic calibration using this stage can suppress the measurement errors.

3. System performance evaluation

3.1 Repeatability evaluation

Using the present system, a 300 mm wafer was measured for its GBIR, SFQR, and ESFQR, each 10 times, to evaluate the repeatability.

The results of the GBIR measurement are shown in **Fig. 6**. The standard deviation (σ) is 0.68 nm. Against the total thickness variation for the wafer of 649.2 nm (on average), the results demonstrate the repeatability of 1 nm or better. The measured values vary randomly without any distinguishing trend, such as monotonic increase, in the characteristic variation. **Fig. 7** depicts the standard deviation (σ) of the measured SFQR values plotted for the frequency distribution for the number of sites. The conditions for calculation are: size of site, 26 x 8 mm; site offset, (0,0); and the total number of sites, 336. The standard deviations (σ) for all the sites are 0.33 nm on average; 88.3% of the sites have standard deviations of 0.5 nm or smaller; and all the sites have standard deviations of 1 nm or smaller. Likewise, **Fig. 8** depicts the standard deviation (σ) of the measured ESFQR values plotted against the frequency distribution for the number of sites. The conditions for calculation are: sector length, 30 mm; sector angle, 5 degree; and the total number of sites, 72. The standard deviations (σ) for all the sites are 0.39 nm on average, 87.9% of sites have standard deviations of 0.5 nm or smaller, and all the sites have standard deviations of 1 nm or smaller.

Comparison of the distributions of standard deviation (σ) between SFQR and ESFQR indicates that SFQR has a greater number of sites having standard deviations (σ) of 0.25 nm or smaller. This is considered to be attributable to the area of each site that is 70% smaller than a sector making the measurement time for each site shorter, which suppresses the errors having long-term compositions. A similar explanation may hold for the repeatability of SFQR and ESFQR, which is better than that of GBIR.

The above results confirm that, in addition to global flatness, the site flatness of the inner and near-the-edge surface can be measured with an accuracy of sub-nanometer order, which was the object of this study.

3.2 Actual measurement

The present system was used for the measurement of two practical wafers (samples A and B.) **Fig. 9** depicts 2-dimensional maps of thickness, as well as the thickness distribution measured along each line (the arrows in the figure.) The GBIR for sample A was 0.609 μm, while that for

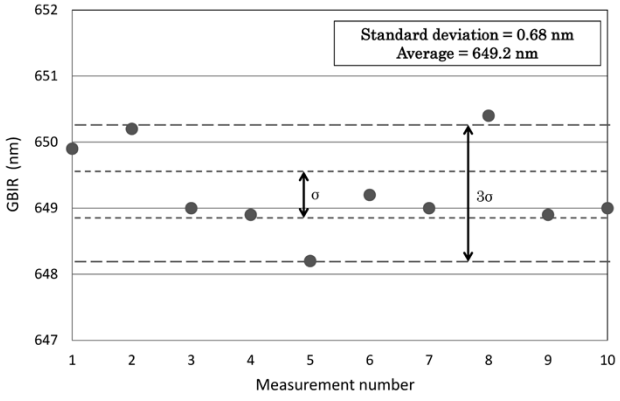

Fig. 6 Repeatability of GBIR

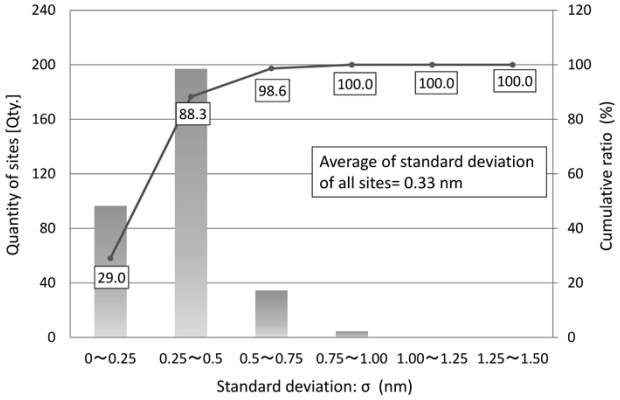

Fig. 7 Repeatability of SFQR

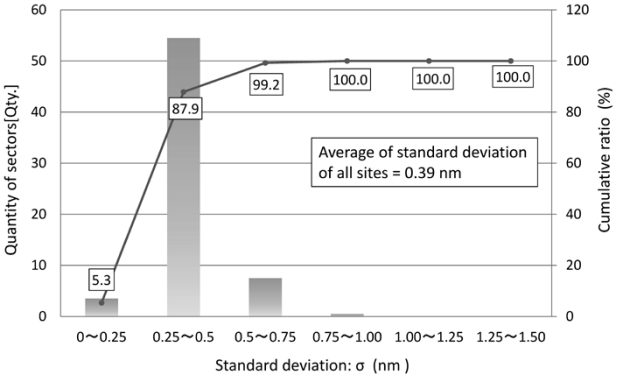

Fig. 8 Repeatability of ESFQR

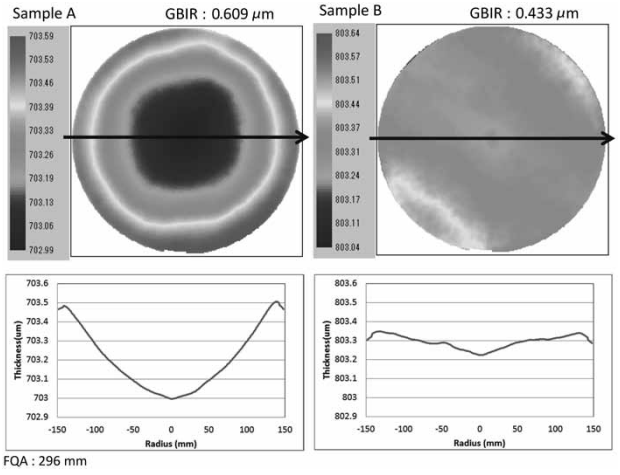

Fig. 9 2 D map of sample A, B

sample B was 0.433 μm. In general, the flatness of a wafer tends to deteriorate near the circumference rather than the central region.[6] The thickness distribution measured along one line shows a significant thickness change for each of the wafers, verifying the measurement of thickness distribution in submicron order.

Fig.10 provides SFQR site maps. Each map is a gray scale image of 20 nm pitch with darker gray representing greater values, and only the sites with values of 10 nm or smaller are represented by white. Focusing on the central region of each wafer, sample A is mostly occupied by sites with SFQRs of 20 nm or smaller, while sample B has a number of sites with SFQRs exceeding 20 nm. Hence the average value is smaller for sample A; 26.9 nm for sample A and 30.5 nm for sample B. Each sample has near-the-edge sites whose values are greater than those in the corresponding central region and are close to 100 nm. Comparing the SFQR Max, sample A has a value of 135.5 nm and sample B has a value of 107.9 nm, sample A having a value greater by approximately 30 nm. **Fig.11** shows the results of ESFQR measurement conducted on the same wafers to study the details near the respective edges. The vertical axis represents the ESFQR values measured, while the horizontal axis represents the angles of the sectors in the circumferential direction. The ESFQR average values are 335.4 nm for sample A and 466.2 nm for sample B, showing that sample A has smaller values as a whole. The above evaluation indicates that sample A has smaller thickness variation near the edge, while the thickness variations in the circumferential direction are similar for both the wafers.

As has been described thus far, the present system can clearly detect thickness variations of

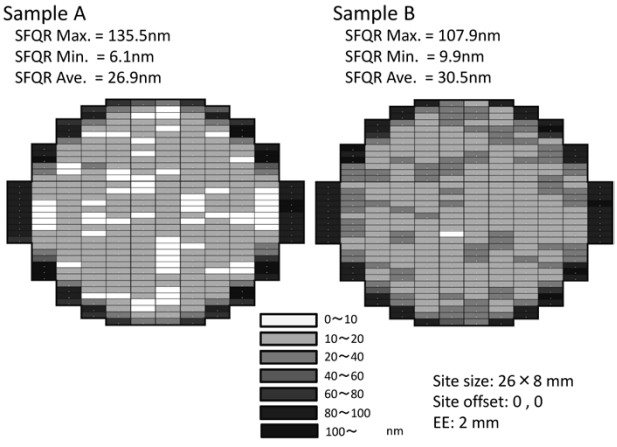

Fig.10 SFQR site map of sample A, B

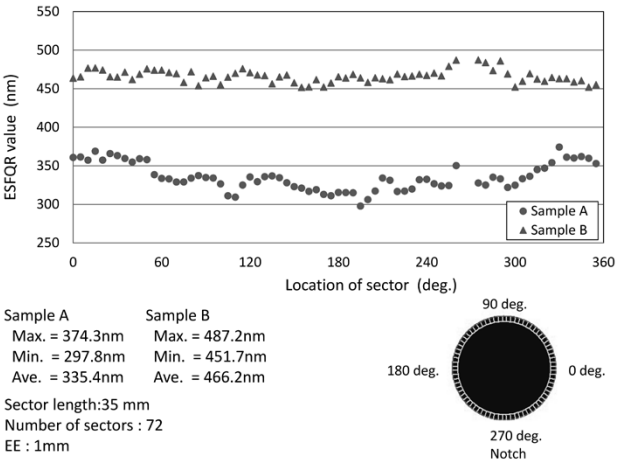

Fig.11 Relationship between ESFQR and sector angle of sample A and B

practical samples in micron to nanometer order. Their flatness features have been clarified by several evaluation techniques.

3.3 Discussions

Actual measurements have confirmed the repeatability of 0.68 nm (σ) for GBIR, 0.33 nm (σ) for SFQR and 0.39 nm (σ) for ESFQR (see 3.1.) These results demonstrate that the present system is capable of measuring wafer thickness with an accuracy of sub-nanometer order. The present system satisfies the measurement accuracy required for a site-flatness inspection system and can evaluate the wafers used for ten-odd nanometer design rule, which is expected to be launched in volume.

The present system may be used for the optimization of wafer polishing conditions. For example, the roll off of wafer-edges, occurring in the process of etching, grinding and polishing, may be improved by visual means based on 2 dimensional mappings and line profiles, as well as by quantitative evaluation by ESFQR measurements, as demonstrated for samples A and B (see 3.2.) Also, among other things, flatness deterioration due to malfunctioning wafer polisher may be detected, allowing the use of feedback in various manufacturing processes.

The specifications of the present system are listed in **Table 1**. It is less susceptible to external vibrations and has been confirmed to achieve repeatability that equals to the one reported herein under a floor vibration of 5 Gal. The spatial resolutions are 1 mm or smaller for SFQR, and 0.5 nm or smaller for ESFQR. The measurement time is 60 sec/wafer or less (for SFQR measurement) including the wafer transfer time by edge handling.

Table 1 Standard specification of developed measurement system

Wafer / Size	Silicon monocrystalline wafer (polish) / 300 mm
Wafer thickness	650～850 μm
Cassette / Transportation	FOSB, Open, FOUP etc. / Edge handling
Measurement method	Laser interferometer (flatness, bow/warp) Laser displacement meter (center thickness)
Scan mode	Spiral scan : R direction ; 0.5 , 1 , 2 mm pitch θ direction : ≦1 mm pitch
Measurement item	Global flatness : GBIR, GFLD, GF3D, GFLR, GF3R Site flatness : site ; SBIR, SFLR, SF3R, SFQR, SBID, SFLD, SF3D, SFQD sector ; ESFQR, ESFQD Shape : bow/warp Thickness : center thickness etc.
Repeatability(σ)	GBIR : ≦3 nm (typ. : 1 nm) SFQR : ≦1 nm (typ. : 0.5 nm) ESFQR : ≦1.3 nm (typ. : 0.5 nm) bow/warp : 1.2+ (warp/100) μm
Tact time	≦ 60 s/wafer
Size of device / Weight	1,970 × 2,990 × 2,200 mm (W,D,H) / 4,500 kg (approx.)
Temperature	23℃±1℃
Environment	Vibration of floor : ≦5 Gal, Clean room : Class1000 or More
Application	Edge rolloff, Resistance, PN judgment, ID reading, Diameter FFU, Load port, OHT, SECS/GEM etc.

Conclusions

A site flatness measurement system with sub-nanometer order accuracy has been developed for the post-polishing inspection of silicon wafers. The system comprises a heterodyne interferometer, a stage/base having excellent anti-vibration performance, and a highly functional vibration absorber. The repeatability (σ) of global flatness and site flatness was 0.68 nm for GBIR, 0.33 nm for SFQR and 0.39 nm for ESFQR, as per actual measurements. Flatness evaluation indices, such as SFQR and ESFQR, were compared for two wafer samples, which revealed their flatness features. The present system thus has been verified to be effective for various process controls.

The present system with enhanced vibration resistance is expected to be used for various wafer production processes and research applications so as to contribute to the manufacturing of high-quality wafers.

References

1) *ITRS International Technology Roadmap for Semiconductors 2013 Edition*.
2) K Tahara. *KOBERUNIKUSU*. 2014, No. 42, p. 18.
3) K Tahara. *KOBERUNIKUSU*. 2014, No. 42, p. 16.
4) H. Matsuoka et al. *R&D Kobe Steel Engineering Reports*. 2009, Vol.59, No.2, p.7.
5) JP Patent 5199141
6) T. Morimoto et al. *R&D Kobe Steel Engineering Reports*. 2005, Vol.55, No.1, p.45.

Experimental Production, Evaluation and Analysis Technologies for Li-ion Secondary Batteries

Takayuki TSUBOTA*1, Takashi ACHIHA*1, Yoshiki HAYASHI*1, Dr. Rinun SYU*1, Takashi IKEDA*1, Masato NISHIUCHI*2

*1 Electronics Technology Div., Technology Unit, Kobelco Research Institute, Inc
*2 Material Solutions Div., Technology Unit, Kobelco Research Institute, Inc

For Li-ion batteries used in vehicles and large-scale load-leveling systems, it is necessary to clarify negative electrode or positive electrode degrades to improve durability and predict battery life. In addition, it is important to clarify the relationship between the configuration factor for internal resistance and the fabrication elements of Li-ion batteries. We therefore investigated the internal resistance determined using electrochemical impedance spectroscopy (EIS), structural changes, chemical bonding states, and the relationship between the deterioration mechanism and the internal resistance in Li-ion batteries. This study demonstrated that a separation analysis of resistance involving the disassembly and re-assembly of a battery is effective for identifying the specific source of degradation. Thus, it is possible to clarify the main factors contributing to the characteristic fading of a battery via internal resistance and degradation analysis.

Introduction

Compared with conventional secondary batteries, such as Ni-MH batteries, lithium-ion secondary batteries are smaller and lighter, and have higher energy densities thanks to their high cell-voltages. Hence, they have been used for mobile devices such as smartphones and, in recent years, are being applied to hybrid cars, electric vehicles and stationary batteries. There are issues, however; their capacities and output must be increased, life be extended, safety be improved and cost be decreased. Hence development is being conducted on their electrode materials, electrolytes and separators. In particular, lithium-ion batteries for vehicles and stationary applications are expected to be used for a long period of time. When improving durability and/or predicting life, it is important to clarify which electrode, the positive or negative, dominates the deterioration. This clarification is key in developing batteries with longer life and improved input/output characteristics.

In response to such needs to clarify deterioration mechanisms, KOBELCO RESEARCH INSTITUTE, Inc. (KRI) has established comprehensive analysis technologies for secondary batteries, including technologies for prototype production, separation analysis of internal-resistance, physical analysis and simulation. As for the deterioration in the charge-discharge cycle in particular, KRI has studied the deterioration mechanism of positive-electrode active materials of batteries used for vehicles and other applications requiring high output.[1)-5)] In these studies, a combined analysis was conducted including physical analysis and separation analysis of the resistance of negative-electrode active materials, such as $Li(Ni_xMn_yCo_{1-x-y})O_2$-type active materials having lamellar rock-salt structure, $LiMn_2O_4$ having spinel structure, $LiFePO_4$ having olivine structure, graphite and Si.

As a continuation of the previous studies,[6)-8)] this paper describes the deterioration of a lithium-ion battery in a cycle test over a long period of time and introduces examples of combined analysis involving the physical analysis and separation analysis of internal resistance.

1. Trial production of batteries for evaluation and evaluation of battery characteristics

When analyzing deterioration, it is important to correlate the degradation of battery characteristics with the deterioration of materials (e.g., crystal structural change in active material, formation of films, and decomposition of electrolyte and generation of gas.) It is also indispensable to develop new evaluation/analysis methods for the purpose.

KRI is capable of experimentally producing evaluation batteries, including prototypes, which comprise various positive-electrode active materials, negative-electrode active materials, separators and electrolytes. **Fig. 1** shows a cylindrical cell (type 18650), laminate cell and prismatic cell that have been produced by KRI and have been used for

Fig. 1 Prototype cells for testing (cylindrical cell, laminate call and prismatic cell from the left)

acquiring data on cycle deterioration and high-temperature degradation. The company has also developed new evaluation/analysis techniques.[9)-12)] The following describes examples in which charge-discharge cycle deterioration was analyzed on a prototype laminate cell simulating a high input/output battery for hybrid applications.

1.1 Trial production of battery for evaluation

A positive electrode was prepared using an active material of Li $(Ni_{1/3}Mn_{1/3}Co_{1/3})O_2$ having an average grain size of 10 μm. Also included were a conductive paste of acetylene black, binder of polyvinylidene fluoride (PVDF) and solvent of N-methylpyrrolidone (NMP). The ingredients were put in a high-speed mixer (a thin-film spin system), in which they were mixed and kneaded for viscosity adjustment. The mixture was then applied on both sides of an aluminum foil collector by a continuous coater. The coated collector was dried and roll-pressed for density adjustment, which resulted in a positive electrode with a composite layer with a final thickness of 42 μm and a density of 2.8 g/cm^3. A negative electrode was prepared using an active material consisting of graphite, which was slurried in a mixer in the same manner as the positive electrode. The slurry was then applied on both sides of a copper foil collector to form a composite layer with a final thickness of 55 μm and a density of 1.3 g/cm^3. The positive and negative electrodes thus prepared were placed in an atmosphere of Ar gas having a dew point of -70℃ or lower, in which the electrodes were disposed face to face with a separator (polyethylene plastic film) sandwiched in between them. This electrode laminate was contained in a cladding and was immersed in an electrolyte (1 mol/L $LiPF_6$/ ethylene carbonate (EC): diethyl carbonate (DEC) = 1 : 1 vol.%) to produce a laminate cell with a designed capacity of 550 mAh. The cell was then subjected to initial charge-discharge at 0.2ItA (0.26mA/cm^2) x 3 cycles.

1.2 Evaluation of capacity degradation during charge-discharge cycle test

The laminate battery thus produced was subjected to a charge-discharge cycle test at the ambient temperature under conditions including a voltage of 2.7V to 4.2V, 2ItA (2.6mA/cm^2), and 6,100 cycles. The chemical reactions are as follows:

Positive-electrode reaction:

$$Li(Ni_{1/3}Co_{1/3}Mn_{1/3})_2 \Leftrightarrow Li_{1-x}(Ni_{1/3}Co_{1/3}Mn_{1/3})O_2 + Li_x^+ + xe^-$$

Negative-electrode reaction:

$$C + Li_x^+ + xe^- + \Leftrightarrow Li_xC$$

Total reaction:

$$Li(Ni_{1/3}Co_{1/3}Mn_{1/3})_2 + C \Leftrightarrow Li_{1-x}(Ni_{1/3}Co_{1/3}Mn_{1/3})O_2 + Li_xC.$$

Fig. 2 shows the charge-discharge curves at 2ItA. As the charge-discharge cycle proceeds, the charge curve shifts toward the high voltage side, while the discharge curve shifts toward the low voltage side. The increase in the over-voltage indicates the increased resistance. Also, degradation is observed in the charge-discharge capacity; the discharge capacity (for 2ItA) at 6,100 cycles decreases to 46% of the initial value.

To study the charge-discharge capacity, constant-current/constant-voltage charging (1 hour holding time for constant voltage) was conducted at 0.2ItA from 2.7V to 4.2V; while constant-current discharging was conducted at 0.2ItA. The resulting charge-discharge curves are shown in **Fig. 3**. The charge-discharge at a low rate is less affected by the over-voltage, enabling the evaluation of chargeable/dischargeable battery capacity. As the charge-discharge cycle proceeds, charge-discharge capacity is degraded; the discharge capacity at 6,100 cycles is decreased to 74% of the initial value. Thus, the charge-discharge cycle increases the internal resistance and degrades the capacity.

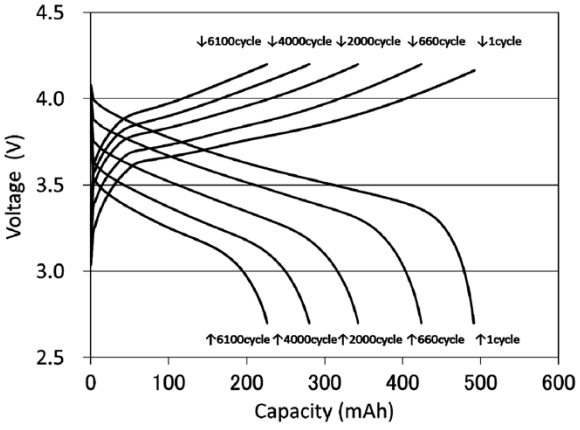

Fig. 2 Cycle dependence of charge-discharge profile (2 ItA)

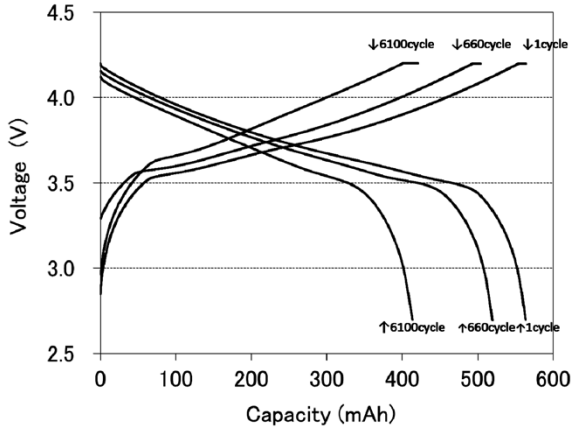

Fig. 3 Cycle dependence of charge-discharge profile (0.2 ItA)

2. Deterioration analysis

2.1 Separation analysis of internal resistance

Specifying the factors increasing internal resistance provides important R&D knowledge for improving charge-discharge cycle durability and input/output characteristics. The factors constituting internal resistance, however, are complex and include reactions involving lithium ions and electrons; namely, for example, charge-transfer resistance at the active-material/electrolyte interface: diffusion resistance acting on lithium ions in active material; electron resistance at, e.g., the active material/active material interface, active material/conductive-paste interface and active material/collector interface; and ion-transfer resistance in the electrolyte. For the analysis of internal resistance, an alternating current impedance method, which can separate reactions with different time constants, is useful.[13] However, time constants that are close to each other allow only the analysis of the alternating-current impedance waveform measured on a battery (full cell) as-is, disabling the separation of the resistance factors.

KRI has developed a separation analysis technology for resistance that separates the contributions of the positive electrode, negative electrode, separator and electrolyte to the internal resistance.[14] **Fig. 4** schematically illustrates the separation analysis of resistance for positive and negative electrodes. For each electrode, the positive and negative, a half cell including a counter electrode of lithium was prepared. Measuring the internal resistance of each half cell enables the separation of the contributions of the positive electrode and negative electrode to the increase in resistance.

A battery for analysis (full cell) was prepared using the positive electrode and negative electrode of a degraded battery and the analysis battery was fully charged before its internal resistance was measured. The results are shown in **Figs. 5** and **6**.

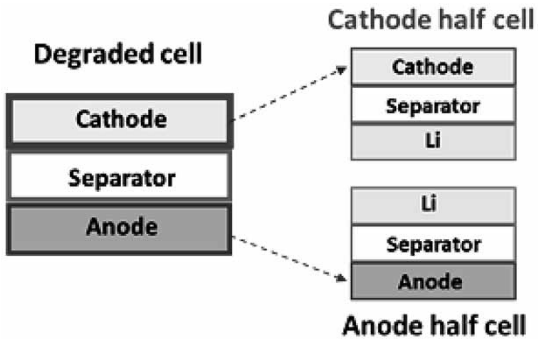

Fig. 4 Schematic image of resistance separation analysis

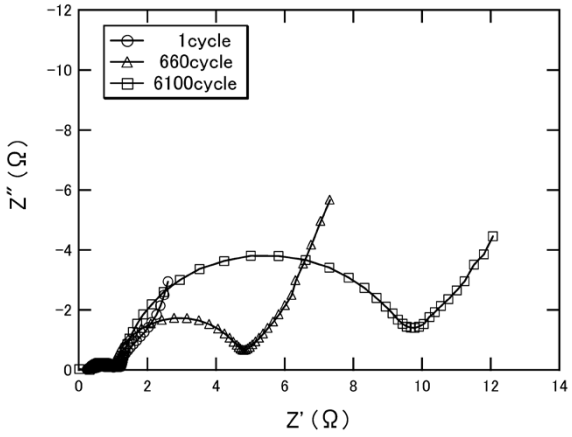

Fig. 5 Nyquist plots of degraded full cell

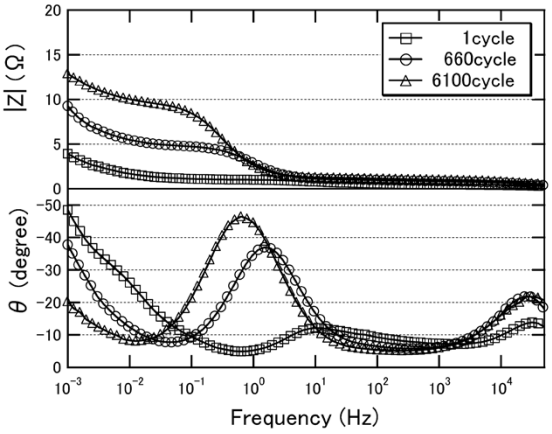

Fig. 6 Bode plots of degraded full cell

The internal resistance was measured by the AC impedance method. This method involves applying a frequency-modulated weak voltage (or, current) to the battery, and measuring the amplitude and phase difference of the response current (or, voltage), thereby separating elementary reaction processes with different time constants. An AC voltage of 1 MHz to 1 mHz with a superposed amplitude of 10mV was applied to the open circuit voltage (OCV), and the response current was measured to determine the internal resistance. The results show an arc corresponding to the reaction responding in the high-frequency region around 10 kHz, an arc associated with the reaction responding in the low-frequency region from 10 Hz to 0.1 Hz, and a linear portion rising diagonally up and to the right, the linear portion indicating the diffusion resistance (Warburg impedance) of lithium ion. The results show that the arc in the low frequency region increases significantly as the cycle proceeds.

Fig. 7 shows the internal resistance in a fully-charged state of the degraded positive-electrode half cell, and **Fig. 8** shows that of the degraded negative-electrode half cell. The positive electrode has been confirmed to have charge-transfer resistance in the

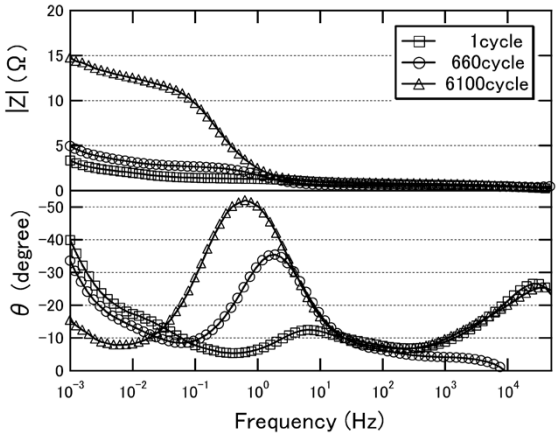

Fig. 7 Bode plots of degraded Cathode half cell

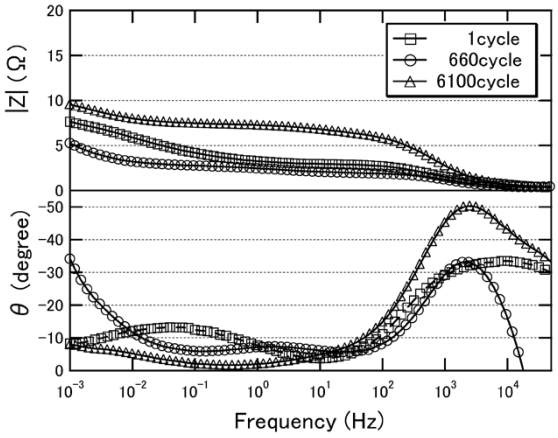

Fig. 8 Bode plots of degraded Anode half cell

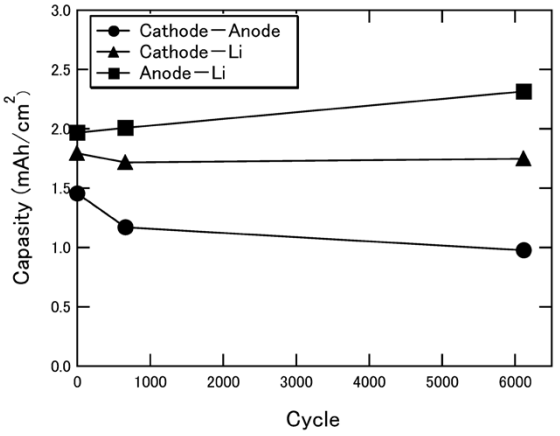

Fig. 9 Capacity fade analysis of cathode and anode

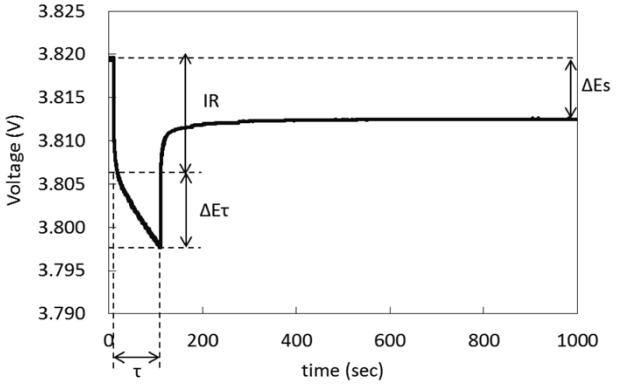

Fig.10 Scheme for single step of GITT profile of NMC cathode material

low-frequency region and to show an increase in resistance similar to that of the full cell. Meanwhile, the negative electrode has been confirmed to exhibit an increase in charge-transfer resistance mainly in the high-frequency region. In the charge-discharge cycle test conducted this time, the full cell exhibited a significant increase of reaction in the low-frequency region. The separation analysis of resistance has revealed that this reaction in the low-frequency region is attributable to the charge-transfer resistance of the positive electrode and the major factor increasing the internal resistance exists in the positive electrode.

2.2 Evaluation of single-electrode capacity

The prepared cells were used for the measurement of single-electrode capacity. The results are shown in **Fig. 9**. The full cell, prepared for the analysis, showed capacity degradation during the charge-discharge cycle test. The positive-electrode half cell and negative-electrode half cell, on the other hand, exhibited no significant capacity degradation like that seen in the full cell. Having a counter electrode of metallic lithium, each half cell contains a sufficient amount of the lithium ion necessary for charge and discharge. It is thus considered that, during the above charge-discharge cycle test, the active materials of the positive and negative electrodes retained the capability of inserting and removing lithium ion; however, the amount of lithium ion to be charged and discharged decreased, causing the capacity degradation. It should be noted that the capacity increase of the negative electrode implies a side reaction in which the electrolyte is decomposed to activate a film-forming reaction.

2.3 Evaluation of diffusion resistance against lithium ion in positive-electrode active material

The above positive-electrode half cell was used to evaluate the diffusion resistance against lithium ion by a galvanostatic intermittent titration technique, (GITT).[15), 16)] **Fig.10** shows an example of the GITT pulse waveform. The IR region in the figure includes the ion conduction resistance in the electrolyte, electron resistance, and charge-transfer resistance at the electrolyte/active-material interface. Meanwhile, the $\Delta E\tau$ region includes the diffusion of lithium ion. However, a combined analysis involving alternating-

current impedance, capable of evaluating reaction time constants, is required to correctly separate the diffusion resistance of lithium ion from the charge-transfer resistance at the electrolyte/active material interface, which has a slow reaction time constant.

The GITT waveform for a 50% charged state was analyzed, and the diffusion coefficient of lithium ion was calculated from Equation (1). Here, L is the thickness of the electrode composite layer, and ΔEs is the potential difference before and after the GITT measurement.

$$D_{Li^+} = \frac{4L^2}{\pi\tau}\left(\frac{\Delta Es}{\Delta E\tau}\right)^2 \quad (\tau << L^2/D_{Li^+}) \quad \cdots\cdots\cdots\cdots\cdots (1)$$

The diffusion coefficient of lithium ion in the positive-electrode active material in a discharged state is shown in **Fig.11**. It has been revealed that, as the charge-discharge cycle proceeds, the diffusion coefficient degrades.

2.4 Deterioration analysis of positive electrode

During charging, lithium ions are removed from the positive-electrode active material and are inserted into the negative-electrode active material. A reverse reaction occurs during discharging. Thus, during the charge-discharge cycle test, structural changes are repeated due to the insertion and removal of lithium ions to and from the active materials of positive and negative electrodes.

In an attempt to elucidate the degradation mechanism of the positive electrode, the change in the crystal structure of the positive electrode was studied using a Cs-STEM. Lithium easily reacts with moisture and changes its state. Hence, the degraded trial batteries were disassembled in the atmosphere of Ar having a dew point of -70℃ or lower to dismount the positive electrode, which was then mounted in a focused ion-beam (FIB) apparatus while maintaining the inert-gas atmosphere. Subsequently, using cross-sectional micro-sampling, samples for transmission electron microscopy (TEM) were extracted and thinned by the FIB.

Fig.12 is a cross-sectional TEM micrograph of a positive-electrode active material after 660 cycles. Li $(Ni_{1/3}Mn_{1/3}Co_{1/3})O_2$ (NMC) has a lamellar rock-salt structure in a hexagonal crystal system. The nano beam electron diffraction, with a simulation pattern for reference, identified a structural change in the surface layer, to a cubic rock-salt structure with lithium removed.

Fig.13 includes a cross-sectional Cs-STEM-HADDF image of the surface layer of the positive-electrode active material observed at an atomic resolution. Lithium ions are generally inserted into, or removed from, the space between layers having arrays of transition metal elements. The observation

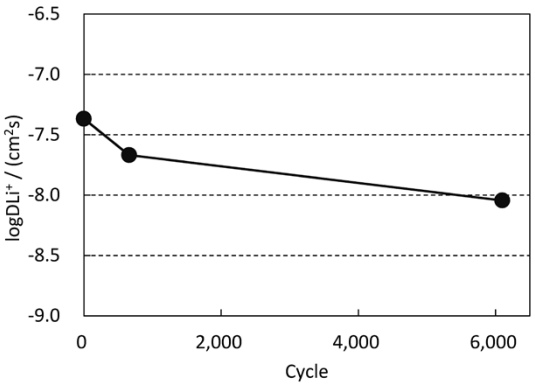

Fig.11 Chemical diffusion coefficient of Li^+ as a function of voltage calculated by GITT analysis

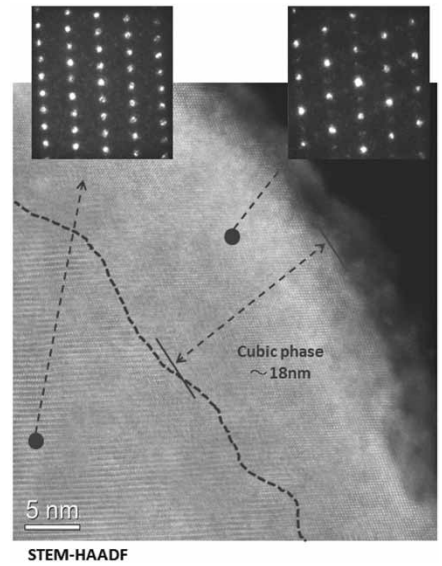

Fig.12 Cs-STEM-HADDF image shows cubic phase on the surface of NMC cathode material (660 cycle)

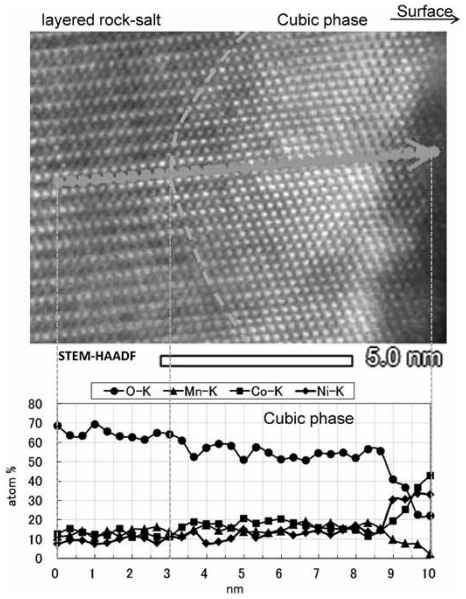

Fig.13 STEM-EDX line scan analysis of surface of NMC (660 cycle)

confirmed a cation mixing, in which transition metals, Ni, Co and Mn, have moved to the sites where lithium ions should exist. An STEM-EDX line analysis has confirmed oxygen defects in the cubic rock-salt structure and the Ni, Co concentrated region caused by Mn elution on the top surface layer.

As described, the surface layer of the positive-electrode active material after 6,100 cycles has undergone a structural change, becoming a cubic rock-salt structure. The thickness of the layer with the changed structure was 30 nm, showing no significant increase; however, the STEMEELS mapping of the chemical binding state, shown in **Fig.14**, has confirmed oxides of Mn/Co and a fluoride-based inorganic interface layer newly formed on the layer having a cubic rock-salt structure, which was created on the active material surface.

2.5 Deterioration analysis of negative electrode

An X-ray photoelectron spectroscope (XPS) was used to clarify the chemical binding state of the surface film of the negative electrode active material after 660 cycles. The narrowband spectra of major elements are shown in **Fig.15**. In addition to organic films and inorganic films including LiF and Li_2CO_3, the observation confirmed the existence of Mn, which is considered to have eluted from the positive-electrode active material and precipitated on the negative electrode. The film thickness was approximately 30 nm in terms of SiO_2.

Fig.16 shows the narrowband spectra of major

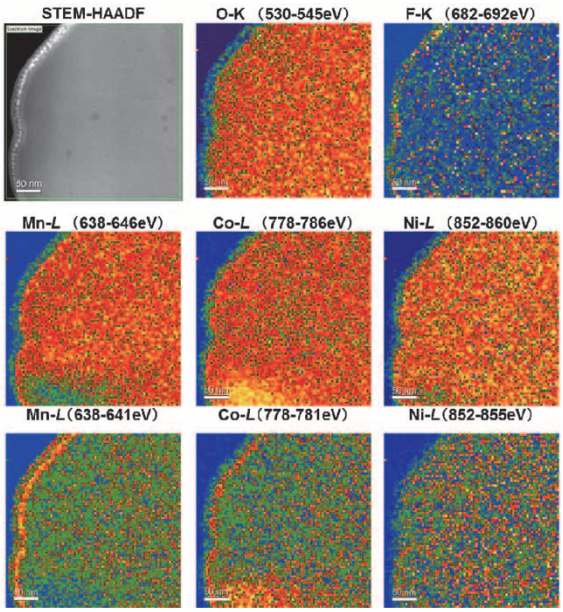

Fig.14 STEM-EELS chemical binding state mapping of surface of NMC (6,100 cycle)

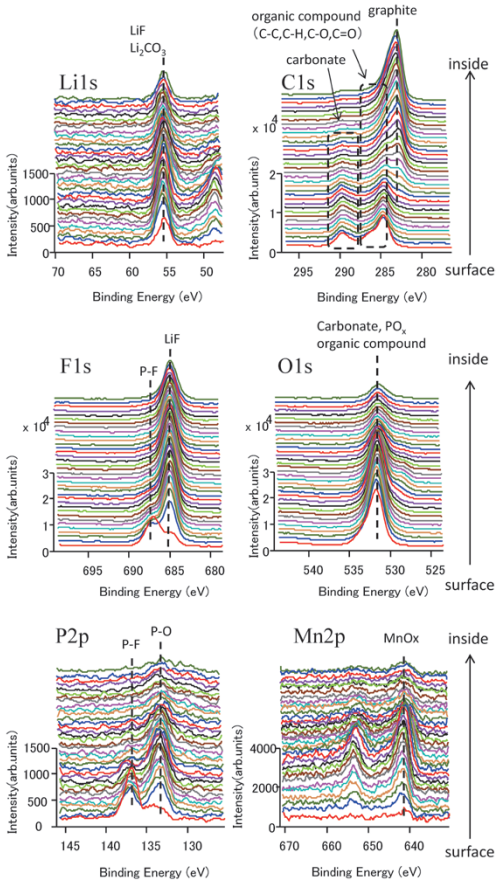

Fig.15 XPS depth profile of surface of graphite (660 cycle)

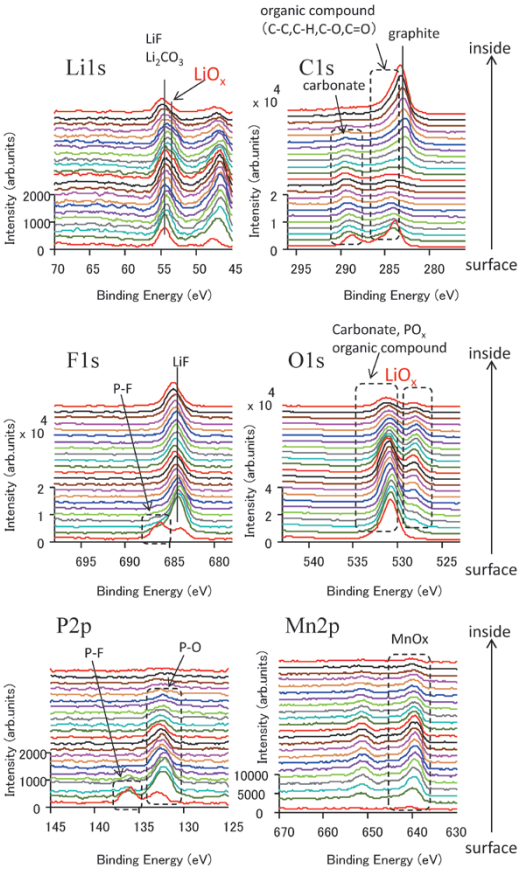

Fig.16 XPS depth profile of surface of graphite (6,100 cycle)

elements in the negative electrode active material after 6,100 cycles. In addition to the organic films and inorganic films including LiF and Li_2CO_3, as observed after 660 cycles, lithium oxides were newly observed. The film thickness was approximately 140 nm in terms of SiO_2, a four-fold or greater increase from the 660 cycles. In addition to LiF and Li_2CO_3, the formation of LiOx during extended cycles is considered to deactivate lithium ions, which otherwise are chargable-dischargable, causing the degradation of charge-discharge capacity.

3. Deterioration mechanism clarified by combined analysis of separation analysis on internal-resistance and physical analysis

The positive-electrode active material with increased internal resistance was found to have a surface layer whose structure had been changed to a cubic rock-salt structure due to the charge-discharge cycles. This change of crystal structure is considered to decrease the number of reaction sites and to increase the charge-transfer resistance at the electrolyte/active material interface. Further, the Mn/Co oxide layer and fluoride layer formed during extended cycles is also considered to decrease the number of reaction sites and to increase the charge-transfer resistance at the electrolyte/active material interface. Moreover, the cation mix, in which transition metals move to lithium-ion sites, is considered to inhibit the diffusion of lithium ion in the solid phase and increase the diffusion resistance.

It has also been found from the charge-discharge cycle test that both the positive and negative electrodes retain the capability of inserting and removing lithium ions; however, the number of lithium ions that can be inserted and removed has decreased. A Li containing film is formed on the graphite surface, which turns into thick LiOx films during extended cycles, which is considered to capture otherwise chargable-dischargable lithium ions and, as a result, degrade the charge-discharge capacity.

Conclusions

Lithium-ion batteries are being increasingly used for vehicles and stationary applications. Various measures will be taken to increase their capacities and output, extend their lifespan, and improve safety. Hence the combined analysis technology, applicable to real batteries, of separation analysis on internal-resistance and physical analysis will become increasingly important in elucidating the deterioration mechanism. There are research and development projects actively pursuing next-generation batteries, including lithium-ion batteries based on a positive electrode with high potential and high capacity,[17] all solid-state batteries employing solid electrolyte,[18), 19)] sodium-ion batteries and fuel cells. KRI is making progress in trial battery production, physical analysis, chemical analysis, safety testing and CAE combined analysis. KRI will strive to integrate these evaluation and analysis technologies and thus contribute to the development of next-generation secondary batteries and fuel cells.

References

1) T. Tsubota et al. *Proceedings of The 52th Battery Symposium (4H13)*. 2011, Tokyo.
2) T. Achiha et al. *51th Electronic Materials Conference, Fall Meeting (A4)*. 2011, Tokyo.
3) T. Tsubota et al. *Proceedings of The 53th Battery Symposium (1A20)*. 2012, Fukuoka.
4) T. Tsubota et al. *Proceedings of The 54th Battery Symposium (2B17)*. 2013, Osaka.
5) T. Tsubota et al. *Proceedings of The 55th Battery Symposium (3F15)*. 2014, Kyoto.
6) T. Tsubota. *KOBERUNIKUSU*. 2010, Vol.19, No.37, pp.4-6.
7) T. Tsubota et al. *47th Electronic Materials Conference, Fall Meeting (A9)*. 2010, Tokyo.
8) T. Tsubota et al. *KOBERUNIKUSU*. 2014, Vol.23, No.41, pp.1-3.
9) Y. Hayashi et al. *Proceedings of The 55th Battery Symposium (3F19)*. 2014, Kyoto.
10) T. Segi et al. *Proceedings of The 55th Battery Symposium (3F16)*. 2014, Kyoto.
11) T. Yamagami et al. *KOBERUNIKUSU*. 2014, Vol.23, No.41, pp.4-6.
12) Y. Takagishi et al. *Proceedings of The 55th Battery Symposium (3F18)*. 2014, Kyoto.
13) D. P. Abraham et al. *J. Electrochem. Soc*. 2006, 153 (8) A1610.
14) M. Nishiuchi et al. *Proceedings of The 53th Battery Symposium (1A19)*. 2012, Fukuoka.
15) Weidong Zheng et al. *Bull. Mater. Sci*. 2013, 36 (3).
16) M. Nishiuchi et al. *Proceedings of The 55th Battery Symposium (3F14)*. 2014, Kyoto.
17) T. Achiha. *Proceedings of The 55th Battery Symposium (3F17)*. 2014, Kyoto.
18) S. Okada et al. *J. Power Sources*. 2005, 146 (1-2) 565.
19) T. Achiha et al. *51th Electronic Materials Conference, Fall Meeting (A1)*, 2014, Tokyo.

Nb_3Sn Wire Technology for High-field Superconducting Magnet

Kazuyoshi SAITO*1, Kyoji ZAITSU*1
*1 Electronics Research Laboratory, Technical Development Group

Nb_3Sn superconducting wires are widely used for high-field superconducting magnets, and the NMR magnet is one of the most successful applications. In order to realize a large Jc (critical current density), which is essential to high-field superconducting magnets, several different types of production methods have been developed, such as the bronze-route method, the powder-in-tube method and the internal tin method. This article first reviews those wire production methods and the technique for Jc value enhancement. After that, current developments in the large Jc Nb_3Sn superconducting wire of Kobe Steel and Japan Superconductor Technology are described. The magnetic field dependence of Jc values in each manufacturing method is presented and the strong and weak points for the industrial usage of each manufacturing method are also described. An effective guideline for achieving the best superconducting magnet performance is discussed, optimizing the placement of Nb_3Sn wire manufactured by each method. The proposed design concept uses PIT method wire for winding the innermost layer and IT method wire for winding the outer layer. This idea could realize an NMR magnet with a high magnetic field and superior cost performance.

Introduction

Superconductivity is a phenomenon that allows electric current to flow with zero resistance under certain conditions. This enables a large electric current to flow in small wires. A general low-voltage wire, for example, has an allowable current density of 4 A/mm^2 due to the generation of Joule heat associated with electrical resistance. A superconducting wire, on the other hand, allows a current of as much as 100 to 200 A/mm^2.[1] Superconducting phenomena were originally discovered from the fact that mercury exhibits zero resistance when cooled to a temperature of approximately 4 K (-269 degrees Celsius.) Since then, much effort has been devoted to research and development aiming at industrial applications.

Although superconductivity requires cryogenic cooling, it can generate high magnetic fields that otherwise cannot be achieved. Hence, superconducting magnets are widely used for nuclear magnetic resonance (NMR), magnetic resonance imaging (MRI) and linear motor cars, a high-speed train system to be inaugurated in 2027 in Japan.

Japan Superconductor Technology, Inc. (JASTEC), a company in the Kobe Steel group, is the only manufacturer in Japan specializing in superconducting technologies, producing and selling both superconducting wires and superconducting magnets.

There are two types of superconducting wires manufactured and sold by JASTEC, namely, NbTi wires and Nb_3Sn wires. The wires of NbTi are mainly used for apparatuses generating magnetic fields up to 10 T (e.g., MRI and linear motor cars), while the wires of Nb_3Sn are used for applications requiring even higher magnetic fields, such as high-field NMRs.[2]

The first half of this paper describes typical manufacturing methods and features of value-added Nb_3Sn wires, which require highly sophisticated production technology, and the latter half describes the Nb_3Sn wires being developed by Kobe Steel and JASTEC.

1. Methods for producing Nb_3Sn wires and their features

Nb_3Sn is an intermetallic compound that is hard and brittle. The compound is difficult to deform plastically, which prevents the application of the production methods (e.g., wire drawing) developed for NbTi wires.[3] In order to resolve the issues of workability and to enable industrial manufacturing, proposals have been made for the use of composite processes, such as the bronze-routed process,[4] powder-in-tube process,[5] and internal tin process.[6] **Fig. 1** schematically illustrates the cross sections

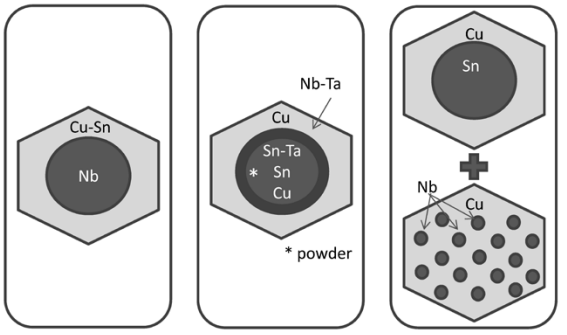

Fig. 1 Schematic cross section of Nb_3Sn single cores in different processes

of the materials made by different production processes, the details of which will be described later.

The characteristics required of superconducting wires depend on the apparatuses and applications, including among others factors, the critical electric current density (hereinafter, Jc), residual resistance ratio (hereinafter, RRR), mechanical strength and alternate current loss. This paper focuses on Jc, which is the most important characteristic of superconducting wires used for high-magnetic-field superconducting magnets, and provides improvement guidelines for each manufacturing process.

1.1 Bronze-routed process

The bronze-routed process (the "bronze" means a Cu-Sn alloy in this article) is a production method comprising the following: making a bundle of a multiplicity of hexagonal Cu-Sn alloy rods, each having a Nb filament core (Fig. 1(a)); inserting the bundle into a sheath of oxygen-free copper to create a composite; wire-drawing the composite; and heat-treating the wire-drawn composite at 650-750℃, thereby producing Nb_3Sn compound on the surface of the Nb filament by diffusion reaction.[4] This process involves no as-is use of Sn, which has a low melting point, and thus enables the extrusion of the billets at high temperatures, each billet having a large size and weight. Hence, the bronze-routed process has the advantage of mass productivity. Although, historically speaking, this is the earliest process to have become industrially feasible, issues remain with regards to the cost and Jc characteristic. The Cu-Sn alloy used as raw material is more expensive than pure metal Sn and Cu. Also, the alloy exhibits significant work hardening during the wire-drawing step, requiring frequent annealing to soften it. In addition, the supply of Sn to the diffusion reaction is limited by the solid solubility limit of Sn in the alloy (15.8%). This limits the amount of Nb_3Sn produced, making it difficult to improve the Jc characteristic.

1.2 Powder-in-tube process

The powder-in-tube process for making Nb_3Sn wires comprises the following: filling a tube of Nb alloy with powder containing Sn (e.g., Sn, Sn alloy, Sn compounds) and Cu; placing the tube in a sheath of copper, and bundling a hexagonal column (Fig. 1 (b); forming the Cu sheathed composite (no figure). Nb_3Sn is formed by Sn contained in the Nb alloy tube diffusing into Nb. This method results in the formation of Cu-Sn alloy during the Nb_3Sn-making step, which minimizes the adverse effect of the work hardening that occurs during the wire drawing. A direct reaction occurs between Nb and Sn without involving any Cu matrix, resulting in a high rate of Nb-Sn diffusion. Hence, the powder-in-tube process has the advantage that the volume fraction of Nb_3Sn can be increased and a high critical current density (Jc) can be obtained.

The use of Nb alloy tube, however, results in a Nb_3Sn core that is larger than that produced by the bronze-routed process, or by the internal tin process, which increases the hysteresis loss when used for AC applications.

1.3 Internal tin process

The internal tin process was devised based on the bronze-routed process to resolve the limitation of Sn concentration required for increasing Jc.[7] The resulting wire has a cross-section with multiple Nb cores and Sn alloy embedded in a Cu matrix. Various types of internal tin processes have hitherto been devised, and they all commonly use the three materials, Sn, Nb and Cu. One of the several wire making methods includes assembling modules, each integrating Cu, Nb core and Sn alloy, in advance. Another method involves assembling together a module combining a Cu and Nb core and another module combining Cu and Sn alloy (Fig. 1 (c)). As in the case of the bronze-routed process, heat treatment is applied such that Nb_3Sn is formed on the surfaces of Nb cores by diffusion reaction. The solid-solubility limit of Cu-Sn alloy places no limitation on the supply of Sn, which enables the amount of Nb_3Sn formation to be increased in order to achieve high Jc. Moreover, this production method processes the Cu, Nb core and Sn alloy independently without involving any material, such as Cu-Sn alloy, that would cause a rapid increase in work hardening and thus eliminates the need for frequent intermediate annealing, which is the factor increasing the cost of the bronze-routed process. It should be noted, however, that hot extrusion cannot be applied due to the low melting point of Sn; hence the process requires a newly devised technology for volume production.

2. Improvement of critical current density (Jc)

Various Nb_3Sn wires have been developed for apparatuses applying superconductivity, each having improved characteristics, such as Jc, mechanical properties and alternate-current loss, depending on the intended purpose. The critical

current density (Jc) is the most basic characteristic of high-magnetic-field superconductor magnets, since it determines the magnetic field generated by superconducting magnets.

There are three aspects involved in improving Jc: namely, i) the amount of the Nb_3Sn compound formed, ii) grain size (grain boundary) and iii) stoichiometric composition. Among them, increasing the amount (area ratio) of Nb_3Sn occupying the cross section of a wire is the most basic approach for improving Jc. In the case of the bronze-routed process, for example, the amount of Nb_3Sn generated can be increased by increasing the concentration of Sn in the Cu-Sn alloy and adjusting the area ratio of the Nb core. **Fig. 2** shows the relationship between the concentration of Sn in the bronze and Jc. It is revealed that increasing the Sn concentration increases Jc.

Next, the crystalline structure of the Nb_3Sn phase, which has a significant effect on Jc, is considered. Nb_3Sn is a type-II superconductor, which, upon the application of an external magnetic field, allows the magnetic field to penetrate into the superconductor. The penetrating magnetic field turns into a quantized state, called magnetic fluxes. When an electric current flows through the superconductor, the Lorentz force is applied to the magnetic fluxes. Any movement of magnetic fluxes in this state generates voltage in the energizing direction, causing energy loss. Hence, practical superconducting wires have mechanisms to suppress the movement of, or to fix, the magnetic flux to avoid the loss. The fixing of magnetic fluxes in a superconductor is called "magnetic flux pinning"; this function is carried out at "pinning centers."[10] The major pinning centers for Nb_3Sn are its grain boundaries, and fine and isotropic crystal grains provide a high Jc characteristic.[11] The grain size changes with the concentration ratio of Nb and Sn, heat treatment, and the like (**Fig. 3**).

Moreover, in the high magnetic-field range

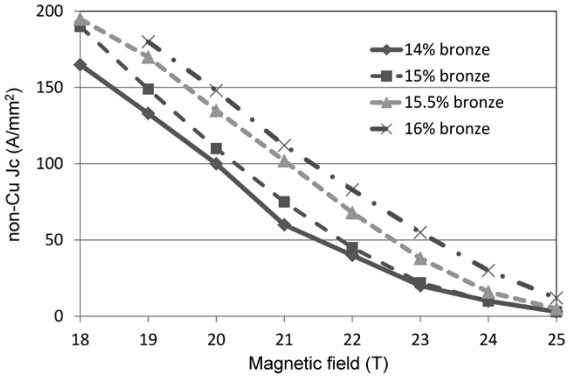

Fig. 2 Non-Cu Jc versus magnetic field curves of Nb_3Sn conductors with shown Sn amount in bronze alloy

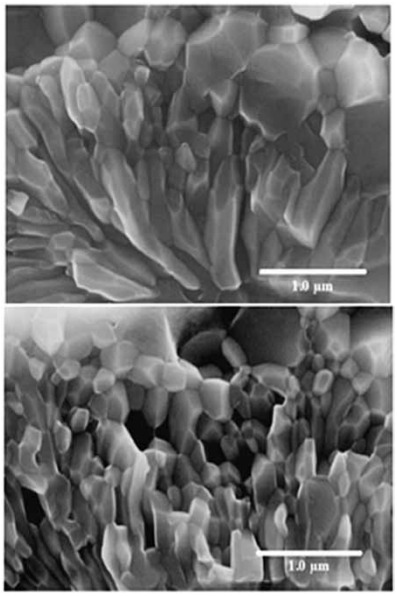

Fig. 3 SEM images of Nb_3Sn crystals using 13 wt% Sn bronze (top) and 15 wt% Sn bronze (bottom)

exceeding 18 T, the composition of the Nb_3Sn phase affects Jc significantly. To improve the Jc characteristic in the high magnetic-field range, several measures have been taken, including the addition of a third element into the Nb_3Sn phase and the high-temperature heat treatment for making the composition close to stoichiometry.[2]

The next section describes the development of Nb_3Sn wires by the Kobe Steel group.

3. Development of Nb_3Sn wires by Kobe Steel group

As a Kobe Steel group company, JASTEC manufactures, as one of its main products, the superconducting magnets of NMR apparatuses for chemical analysis and focuses also on the business of the Nb_3Sn superconducting wires used for this application. The detection sensitivity of NMR measurement increases proportionally to the 3/2 power of the magnetic field used. The resolution also increases in proportion with the magnetic field.

NMR has been used mainly in the field of chemistry, including the synthesis of organic compounds; however, with the recent development of biotechnology, the demand for it is increasing in the structural analysis of large biomolecules; like proteins. Proteins have complicated structures with large molecular weights; hence, analyzing their structures requires NMR apparatuses with high resolution. As a result, there is a strong demand for magnets with a high magnetic field.[12] Currently, the superconducting magnets most commonly used for NMR have a magnetic field of 9.4 T at median; while the NMR apparatuses for biomolecules use

superconducting magnets, each can generate a magnetic field of 14 T or higher. The demand for high-field NMR is strong, and a 1 GHz-class high-field NMR magnet (central magnetic field, 23.5 T) is being developed. The magnetic field to be generated is close to the upper critical magnetic field (Hc2) of Nb_3Sn.[13)]

Against this background and with application to superconducting magnets for high-field NMR as a goal, JASTEC has tested several superconducting wires made by the bronze-routed process, powder-in-tube process (TS-PIT) and internal tin process (DT). **Fig. 4** includes cross-sectional photographs of wires produced by the respective processes, and **Fig. 5** shows their Jc characteristics. Compared with the bronze-routed process, the powder-in-tube process (TS-PIT) resulted in Jc at higher magnetic fields in excess of 18 T, while the internal tin process resulted in higher Jc at magnetic fields up to the vicinity of 18 T. Superconducting magnets designed contemplating the Jc characteristics at these magnetic fields will have an excellent balance of cost and performance. The following describes the details of each process.

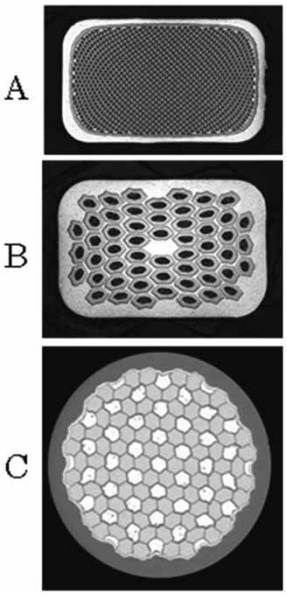

Fig. 4 SEM images of Nb_3Sn conductors developed by Kobe Steel A: bronze routed process, B: power in tube process, C: internal tin process (distributed tin process)

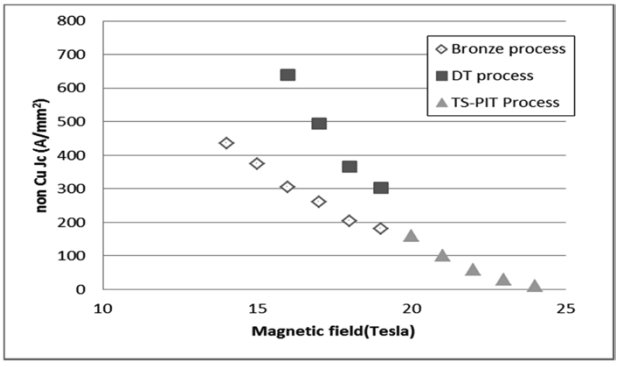

Fig. 5 Non-Cu Jc versus magnetic field curves of Nb_3Sn conductors with three types of manufacturing processes

3.1 Bronze-routed process; Development of Nb_3Sn wire based on high Sn bronze

The first industrial Nb_3Sn wire was produced by the bronze-routed process. Kobe Steel group adapted this process first and continued its development. As a means for increasing Jc, the company aimed at increasing the amount of Nb_3Sn generated in wires and conducted development based on Cu-Sn alloy (bronze) with a high Sn concentration. As described above, increasing the Sn concentration in the Cu-Sn alloy results in a large amount of intermetallic compound, rendering the processing difficult. To this end, the Kobe Steel group focused on the design of cross-sections that are less susceptible to working and on the optimization of the process steps, including the wire drawing and heat treatment. As a result, the company successfully developed a Nb_3Sn wire on the basis of a Cu-Sn alloy containing 16%Sn and achieved a Jc of 194 A/mm^2 at 18.5 T, 4.2 K. The superconducting magnet based on this wire succeeded in generating a high magnetic field of 22 T in 2000. This magnet was used for NMR measurement at 930 MHz, and the NMR apparatus achieved the highest central magnetic field at the time.[8)]

3.2 Powder-in-tube process; Nb_3Sn wire made by TS-PIT process.

In order to achieve a high magnetic field for an NMR apparatus, it is particularly important to improve Jc at high magnetic fields. JASTEC conducted development adapting a type of powder-in-tube process, called TS-PIT.[9)] In the TS-PIT process, powders of Ta and Sn are heat-treated for molten diffusion to produce a Ta-Sn compound, which is ground to powder. The powder is used to fill a sheath of Nb-Ta alloy to be wire-drawn. The idea behind this was that the addition of Ta would increase the diffusion rate of Sn in Nb, which would increase the amount of Nb_3Sn that would be formed. As seen above, the powder-in-tube process is characterized by the fact that elemental addition is relatively easy. Moreover, this process is not limited by the supply of Sn, as in the case of the bronze-routed process, which enables the Nb_3Sn phase to be

formed in a large amount, resulting in an excellent Jc characteristic at a magnetic field of 20 T or higher. It should be noted, however, that this process involves the handling of powder, which requires dedicated facilities. Also required are technologies that are different from the wire drawing of ordinary composite wires.

In order to demonstrate that the excellent magnetic field characteristics of Nb_3Sn wires made by the TS-PIT process can be realized on a practical scale, a prototype 50 kg wire was produced, which verified a significant improvement of Jc in the high-magnetic-field region.

The Jc characteristic has improved by 52% (Jc：295 A/mm^2 at 18.5 T and 4.2 K,) compared under the same condition with the wires produced by the bronze-routed process, used for the superconducting magnet for NMR at 930 MHz previously described. Another challenge for practical applications was the uniformity of the characteristics over the entire length of the wires, since this production method employs powder for raw material. For evaluating the uniformity of Jc characteristic, samples were taken at intervals of 50 m from a 500 m long prototype material, and the samples were subjected to Jc measurement. The results are shown in **Fig. 6**. The average value of Jc was 295 A/mm^2, while the standard deviation was 10 A/mm^2. This value is as good as the values for the bronze-routed process used in practical applications, verifying that a uniform Jc was obtained over the entire length. In addition, a Jc of 170 A/mm^2 was achieved in a high-magnetic-field region (21.5 T.) Although this value falls slightly short of 190 A/mm^2, which is required for an NMR superconducting magnet for 1,000 MHz, the results appear promising for the improvement of characteristics by the future optimization of the production process.

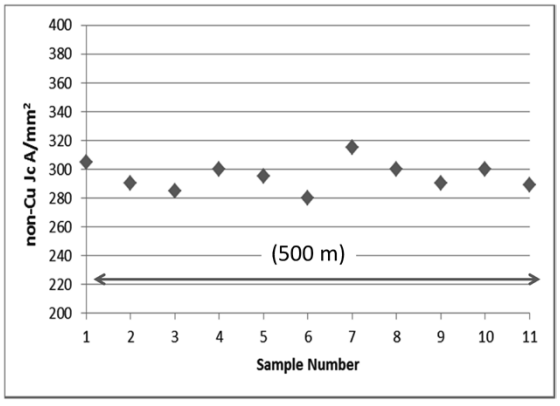

Fig. 6 Jc distribution by PIT process in 500 m long Nb_3Sn conductor

3.3 Internal tin process; Development of Nb_3Sn wire based on dispersed-tin process

In the case of superconducting magnets for super-high magnetic fields, the amount of wire used for an intermediate layer coil (located outside the innermost layer coil) is much greater than that of the innermost layer coil, affecting the cost more significantly. Using a wire based on the powder-in-tube process for these coils is not desirable from the aspect of market competitiveness. The intermediate layer coils require Nb_3Sn wires that cost less than those made by the TS-PIT process and have Jc values higher than that achieved by the bronze-routed process in the high-magnetic-field region of approximately 16-18 T. JASTEC has been conducting technology development based on the concept that the distributed-tin process, a type of internal-tin process, is suitable for this purpose and so far has completed prototype production on a volume production scale. The distributed-tin process is a method involving wire drawing, in which an Nb module (an array of Nb cores disposed in a Cu matrix) and Sn module (Sn alloy embedded in a Cu matrix) are combined. This process allows the amount of Cu matrix to be reduced below that of the conventional process incorporating Nb and Sn into the same module and enables the improvement of Jc. That is, the one module of Nb and Sn requires a Cu matrix that promotes the diffusion reaction of Nb_3Sn, while the distributed-tin process allows Nb and Sn to be distributed, which decreases the amount of Cu matrix, enabling a high Jc to be obtained.

Another prototype 50 kg wire was produced using the distributed-tin process to verify its performance. The resulting Jc was 373 A/mm^2 at 18.5 T and 4.2 K, indicating an improvement in the Jc characteristic of 70% or greater compared with the bronze-routed process.

3.4 Summary

Nb_3Sn wires based on three different processes have been developed for application to magnets with a high magnetic field. As shown in Fig. 6, the relationship between Jc and the magnetic field varies depending on the production processes. Each process has pros and cons, and an optimal one must be selected−with reference to specifications and economy, for example. **Table 1** summarizes the features of these processes. When designing a magnet with a high magnetic field, care is taken to selectively exploit the wire performance for the most economical generation of a high magnetic field.

Table 1 Featured aspects of Nb_3Sn conductors made by different processes and design consideration for NMR magnets

Process	Bronze	Poder in tube (PIT)	Internal tin
Critical current dessity	Low	High up to 24(T)	High below 18(T)
Typical value	180(A/mm^2) @18.5(T)	170(A/mm^2) @21.5(T)	270(A/mm^2) @18.5(T)
Material cost	Middle	High	Low
Lead time	Long	Long	Shrot
Heat teatment	Short	Short	Long
Single unit length	Long	Short	Short
Suitable magnetic field and amount usage in NMR magnet	>16(T) Large	18(T)< Small	>18 (T) Middle

Conclusions

In order to develop a superconducting magnet that generates a high magnetic field, it is imperative that the Nb_3Sn wires have a high Jc. The wires must also be made at low cost to increase market competitiveness. With consideration to these two aspects, we will strive to contribute to the superconductivity business of the Kobe Steel group through the development of Nb_3Sn wires.

References

1) Denkigakkai Tsushinkyoiku, *CHOUDENDOU KOUGAKU*, Ohmsha. 1988, p.233.
2) K. Tachikawa. *TEION KOUGAKU*. 2009, Vol.44, No.10, p.456.
3) K. Egawa et al. *TEION KOUGAKU*. 2004, Vol.39, No.9, p.391.
4) M. Sugimoto et al. *TEION KOUGAKU*. 2012, Vol.47, No.8, p.479.
5) A. Godeke et al. *Cryogenics*. 2008, Vol.48, p.308.
6) K. Tachikawa. *TEION KOGAKU*. 2010, Vol.45, No.3, p.88.
7) T. Takeuchi. National Institute for Materials Science (NIMS). http://www.nims.go.jp/smcMetal/kinzokuchoudenndoutainoayumi_5_S1_2.pdf, (reference date: 2015-03-10).
8) T. Miyazaki et al. *TEION KOUGAKU*. 2004, Vol.39, No.9, p.415.
9) K. Zaitsu et al. *R&D Kobe Steel Engineering Reports*. 2007, Vol.57, No.3, p.58.
10) T. Matsushita et al. *CHOUDENDOU KOUGAKU NO KISO*. Yoneda Shuppan, 2004, p.23.
11) M. Konuma et al. *CHOUDENDOU ZAIRYOU TO SENZAIKA GIJUTSU*. Kougakutosho. 1995. p.181.
12) H. Maeda et al. *TEION KOUGAKU*. 2002, Vol.37, No.1, p.2.
13) T. Kiyoshi . *TEION KOUGAKU*. 2002, Vol.37, No.1, p.10.